UNIVERSITÀ DEGLI STUDI DI PALERMO
Dottorato INFORMATION AND COMMUNICATION TECHNOLOGIES
Dipartimento Energia, Ingegneria dell'Informazione e Modelli Matematici
Settore Scientifico Disciplinare ING-IND/22

Luminescent composites for optical applications

IL DOTTORE
Francesco Armetta

IL TUTOR
Prof. Patrizia Livreri

IL COORDINATORE
Prof. Ilenia Tinnirello

CO TUTORS
Prof. Vincenzo La Carrubba
Dr. Maria Luisa Saladino

CICLO XXX
ANNO CONSEGUIMENTO TITOLO 2018.

Progetto: DELIAS – "Ricercatori ed Esperti Di Alta Tecnologia e Innovazione Tecnologica Applicata al Settore dei Beni Culturali" a valere sull'Avviso n. 713/Ric. del 29 ottobre 2010
TITOLO III
"CREAZIONE DI NUOVI DISTRETTI E/O NUOVE AGGREGAZIONI PUBBLICO – PRIVATE"

Codice identificativo progetto: PON03PE_00214_2/F9

UNIONE EUROPEA
Fondo Europeo di Sviluppo Regionale

Ministero dell'Istruzione, dell'Università e della Ricerca
Ministero dello Sviluppo Economico
Ministro per la Coesione Territoriale

Luminescent composites for optical applications

INDEX

- **Transmission Electron Microscopy**
- **Nuclear Magnetic Resonance Spectroscopy**
- **Thermogravimetry and Differential Thermal Analysis**
- **Porosimetry**
- **Infrared Spectroscopy**
- **Luminescence Spectroscopy**
- **Emission spectroscopy**
- **Viscosimetry**
- **Electrical conductivity**

A3. Graphs and tables

A4. Scientific activity of Francesco Armetta

List of Publications

List of Communications

Presentation

In the last years, the optical devices have been one of the promoted and developed important technologies. From the invention of the first lamp to the production of lasers, LED and optical sensors an evolution of the performances of the devices has been observed strictly connected to the properties of the materials used for their production. The researchers are nowadays working on the assessment of well-known materials and on the development of new materials having improved optical properties. In this context, the nanomaterials are at the same time a resource and a challenge, due to their improved and innovative optical properties and to the difficult of control the synthesis process and the nanoparticle properties. The scale up of nanoparticle synthesis have to face with economic issue due to the request of high performance materials with a low cost production. In fact these materials are in form of powder, that cannot directly to be used for the device fabrication, so they have to be combined with other substances both inorganic and organic easily processable with adequate mechanical and optical properties for the devices.

The combination of optical powders (phosphors) could generate composites, nanocomposites or supramolecular hierarchical structures depending on the size of phosphors and the nature of other substances. This new materials allowed to produce technological devices having any shape but maintaining or tuning the optical properties of the phosphor.

An appealing application for researchers and industry is about the white light production by Light Emitting Diodes (LED) devices. Until now several types of materials having optical properties have been developed. Among other materials, the phosphors, compounds doped with trivalent lanthanides ions which confer luminescent properties to crystalline structures, are particularly interesting.

Yttrium Aluminium Garnet (YAG, $Y_3Al_5O_{12}$) is one of the crystalline systems with good luminescent performance after the doping. It is possible to prepare single crystals or nanopowders, which are processable as ceramics and composites.

The **goal** of the thesis is the development of luminescent composites and nanocomposites based on doped YAG, having high performances useful for white LED, pointing to the tailoring of their optical properties by choosing proper methodology of preparation.

The composites and nanocomposites were prepared by using Ce:YAG phosphor or nanophosphor as filler. Different methodologies were used for their preparation by systematically varying some of the parameters that affect the final structural and optical properties. The more suitable composites and nanocomposites were tested for the realization of white LED.

In a first step, two series of composites were prepared by dispersing commercial Ce:YAG phosphors in PolyMethylMethacrylate (PMMA) and in PolyCarbonate (PC) by using the melt mixing procedure. The effect of the phosphor concentration has been investigated. This work has been carried out in collaboration with Prof. Adriaan S. Luyt of Department of Chemistry, University of the Free State (Qwaqwa Campus), South Africa.

In the second step, the development of non-common and innovative synthesis for the preparation of Ce:YAG nanophosphors has been carried out. The obtained products were characterized and the nanophosphors having the best structural and optical properties were used for the preparation of PMMA nanocomposites by using the solvent casting procedure and for the test in a wLED device. The glycothermal synthesis and the microemulsion assisted synthesis have been developed. The Urea Glass Route (UGR) method has been carried out in collaboration with Dr. Cristina Giordano at Institut für Chemie, Technische, Universität Berlin (Germany) and at School of Biological and Chemical Sciences, Queen Mary University of London (UK).

In the last step, non conventional Ce:YAG hierarchical nanostructures have been developed. Hierarchical structure could extoll the optical properties of nanophosphor and the mechanical properties of the template (e.g. foldable paper or unrolling glass wool) opening up the way to a myriad of possibility to preparation of systems that can be easily shaped for advanced lightening applications.

The optical properties of the obtained materials have been investigated in collaboration with Dr. Ing. Dariusz Hreniak of Institute of Low Temperature and Structure Research, Polish Academy of Sciences, Wrocław (Poland).

The thesis is organised in four chapters as below:

- Chapter I is a short overview of luminescent materials features and possible applications, with focus on the doped YAG phosphors and nanophosphors and their composites.
- Chapter II is a description of the preparation and characterization of Ce:YAG-PMMA and Ce:YAG-PC composites by using commercial powder. A deepened investigation on the structural and optical properties is presented. The application of the composites in a wLED device is also reported.
- Chapter III describes the development and the assessment of three non-common synthetic routes to obtain the Ce:YAG nanophosphors. The preparation and characterization of Ce:YAG-PMMA nanocomposites and their application in a white LED by using the best synthetized nanophosphors is also reported.
- Chapter IV reports the development of non-conventional hierarchical nanostructures based on glass wool for possible lighting applications.

CHAPTER I

Luminescent materials

§ 1.1. Luminescent composite features and applications

Luminescence is defined as the emission of light by bodies, which is in excess of that attributable to black body radiation, and persists considerably longer than the periods of electromagnetics radiations in the visible range after the excitation stops.

Luminescent materials are called phosphors. The first systematic study of luminescent crystals was made by Lenard and his school at the beginning of the twentieth century [1]. The practical interest in luminescent materials for use in efficient cathode ray screens, and eventually for luminescent lamps, which were developed in 1939's, stimulated the study of crystal luminescence in a very substantial way.

There are several types of luminescent materials both organic and inorganic [2,3].

The luminescent system generally consists of a host lattice and a luminescent center, often called as 'activator'. In general, the host needs to be transparent than the radiation source used for excitation process.

The host could affect the luminescence properties of the material so it is important to evaluate the proper host-activator couple in order to gain the desired luminescence. Luminescent ions mainly include lanthanides, transition metals, and main group of metal ions.

The activator absorbs the exciting radiation and is raised to an excited state. The excited state returns to the ground state by emission of radiation or by non-radiative decay. It is necessary to suppress this non-radiative process. In some materials the excitation radiation is not absorbed by the activator but the other ion may absorb the exciting radiation and subsequently transfer it to the activator. In this case, the

absorbing ion is called as a "sensitizer". In many cases the host lattice transfers its excitation energy to the activator, so that, the host lattice acts as the sensitizer. High-energy excitation always excites the host lattice. Direct excitation of activator is only possible with ultraviolet and visible radiation [4].

Depending on the decay time (τ) of photon emission, the photoluminescence can be classified as fluorescence or phosphorescence. Fluorescence possesses a short time lapse (τ<10 ms) after the excitation source is removed, whereas phosphorescence has a much longer decay time (τ > 0.1 s).

The common mechanisms involved in luminescence process are showed in Figure 1.1.

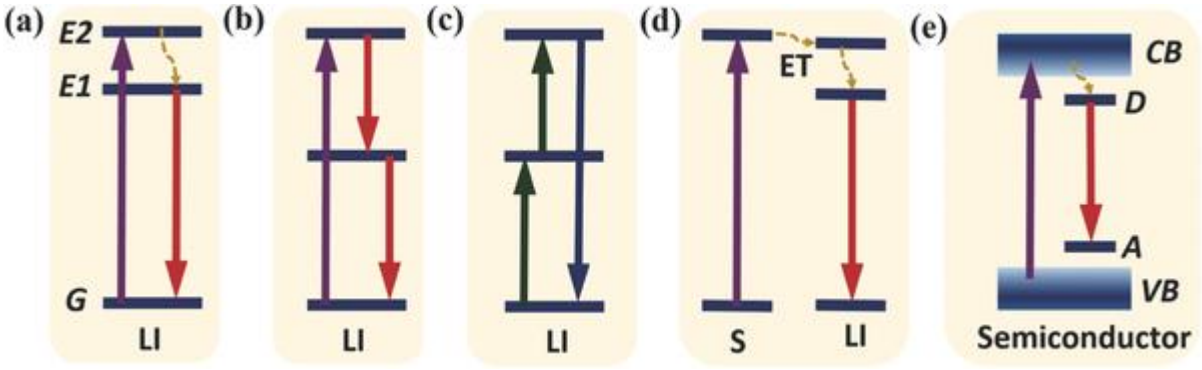

Figure 1.1 Luminescent mechanisms: (a) down-shifting, (b) down-conversion, (c) up-conversion, (d) Sensitized emission from an activator through energy transfer. (e). LI Luminescent Ions, E and G Excited and Ground states, S Sensitizer, ET Energy Transfer. CB and VB Conduction and Valence Bands, D and A Donor and Acceptor energy levels.

The luminescence of active ions can be basically classified into several types as function of the path followed by the electron.

- **down-shifting**: Stokes emissions with photon energy smaller than the excitation source as consequence of a non-radiative relaxation process.
- **down-conversion:** Stokes emissions caused by the presence of two emission process.
- **Up-conversion:** anti-Stokes emission which needs two or more excitation photons to produce a higher energy photon.

In case of an active ion without efficient absorption matching, the available pump energy, a sensitizer ion can be incorporated into the host material to transfer the excitation energy to the activator (Figure 1 (d)). As shown in Figure 1 (e), when luminescent ions are doped host, emission can occur under band-to-band excitation. The excitation energy transfers from the host to the doped luminescent ions. On the whole, luminescent ions can absorb the supplied energy and then give specific light due to the variation in the energy-level structure.

Luminescence has been playing a major scientific and technological role for humankind. Numerous kinds of metal-ion-doped phosphors have been synthesized in different forms, such as glasses, crystal bulks, ceramics, powders, nanoparticles (NPs) [5], and thin films [6], in which the luminescence properties primarily depend on the ion type and its energy transition. The use of a specific ion is strictly connected to the emission required for the material use. Furthermore, a codoping is also possible in order to fabricate tuned luminescent materials [7].

The possibility to combine luminescent ion doped phosphor with other materials represent the key for the preparation of novel systems with high and novel performances. The systems not only complement different functional properties in one material, but may possess superior mechanical, luminescent, or thermal properties also offering a possibility to manufacture high-performance and low-cost materials. Incorporating luminescent ions into several advanced functional materials while keeping the beneficial aspects of each component can form novel multifunctional materials [8].

The preparation of luminescent composite materials with coupling effects are promising for multifunctional applications, including novel display, multimodal bioimaging, phototherapy, drug delivery, biodetection, photocatalysis, thermometer, and optical sensing [9]. One example of this kind of composite materials are the organic and organic-inorganic metal-ion doped hybrid phosphors, like metal-organic frameworks [10].

An essential classification of the multifunctional materials is based on the dimension of their components. Composites are prepared by using micrometric or macrometric components, nanocomposites contain at least one nanometric component.

Literature is full of studies regarding the preparation of luminescent multifunction materials with different nature, structure and properties [11,12]. In this thesis the attention is focalized on phosphors dispersed in polymeric matrixes for the production of one of the component of white Light-Emitting Diode (LED) device and on hierarchical nanostructured phosphors.

LED is a solid state electroluminescent device, which is totally revolutionizing the world of enlightenment. Although studies on the first LEDs were not particularly promising, research has made progress by focusing most of its interest on high-bandgap III-V compounds. In 1993, Shuji Nakamura, a Nichia Corporation's engineer, developed the first high performance blue LED [13] using a dual Gallium nitride-based heteronuclear structure and its ternary alloys (InGaN / AlGaN). Three years later Nakamura coupled the blue LED with Ce:YAG obtaining white light. It was the invention of the white LED (wLED). In this technology the phosphorus absorbs part of the incident blue radiation on it and resumes it by showing a luminescence on the green, yellow and red portion of the visible spectrum as show in Figure 1.2.

Another method to produce the white light is to use three LEDs of blue, green, and red together. In this case the light is intense and a lot of color can be produced, allowing their application to large display and a LED screen production.

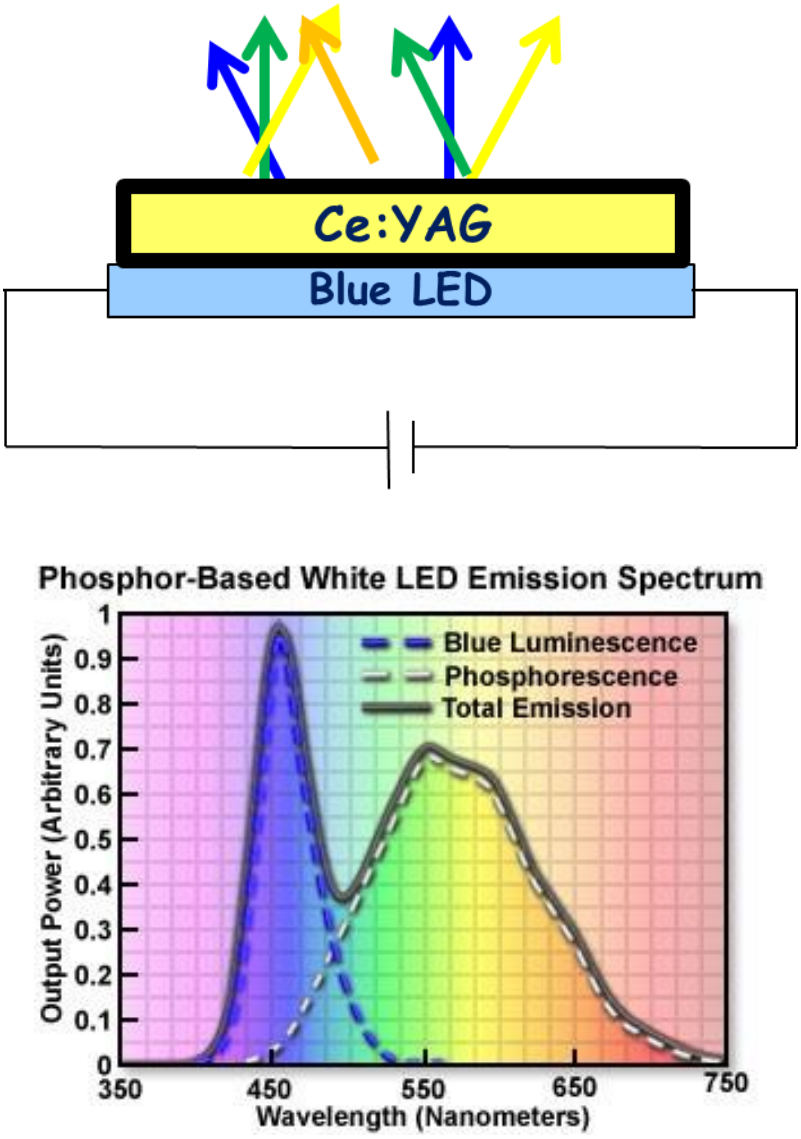

Figure 1.2. (up) Scheme of Nakamura's wLED; (down) Emission spectrum of white light generated by a wLED.

After nearly a century of rapid development, LEDs are considered by the scientific community as being ready to replace incandescent and fluorescent lighting. wLEDs as compared to the typical values of traditional incandescent and fluorescent lighting technologies, display competitive values of luminous efficacy, colour rendering index (CRI) and correlated colour temperature (CCT)[14]. These characteristics, corroborate

by low cost, energy efficient, mercury-free, long lifetimes, and compactness involved a large increase of the use of this illumination device [15].

The definition of the relevant factors that affect the quality of these new sources is a key aspect for the design and production of such electronic devices.

Ce^{3+} and Eu^{2+} (through the parity-allowed 5d–4f transitions) are the most used lanthanide ions, which satisfy the solid-state lighting requirements of small Stokes energy loss, strong absorption, and short ($<10^{-6}$ s) excited state lifetimes. Although, the few chemically stable and non-toxic Ce^{3+} and Eu^{2+} doped hosts available present some important disadvantages, such as expensive large scale synthesis, low moisture stability, thermal instability at present operating temperatures of the devices, color deficiency in the blue-green and red spectral regions, which limits the luminous efficacy, as well as the broadband red emissions.

In the past decade researcher worked to develop of new phosphors (both organic and inorganic), able to better fulfill the solid-state lighting requirements.

The main challenge in solid-state lighting is the development of novel materials that collect the blue light from long UV/blue LEDs and efficiently convert it into the other colors needed for white light emission. The materials should, therefore, display the following requests:

- Ability to be synthesized and recycled in easy large scale processes;
- High brightness;
- Emission quantum yield values larger than 0.50 to reduce the emitters concentration (~0.1–3.0% by weight), while retaining the integrity (transparency, mechanical and thermal stability) of the hybrid host after doping;
- Blue, yellow-green, green and red emission colors with high CRI and controlled CCT, purity and hue;
- Photostability under UV irradiation.

Concerning the processability of the lighting devices, the focus must be placed in large-scale thin film technology, namely in the hybrid/substrate and multi-layers adhesion, thickness values and homogeneity control, low surface roughness, and optical transparency [16].

Regarding the composite for wLED production, several types of medium, both organic and inorganic could be used. As inorganic the silica is the most used for the preparation of ceramics [17, 18]. Recently, the new generation is the class of phosphor-in-glass (PiG) where the mixture is sintered at an optimal temperature at which the glass components are melted, while the phosphor powders remained solid as much as possible [19].

As organic medium, epoxy resin or silicone [20,21] polymethylmethacrylate (PMMA) and polyurethane (PU) are some of the most used thanks to the process which entraps the phosphor particles and to properties such as good transmission over the visible spectral range, mechanical properties of plasticity, lightness, easiness of fabrication and low cost of massive production [22,23,24,25]. In some cases the polymeric matrixes could allow an organization of nanoparticles into supramolecular structures, which considerably increase the extraordinary properties of nanoparticles [26].

Researchers are demonstrating the possibility to use nanopowders which have a number of distinct advantages including favorable quantum confinement effects, increased optical lifetime, and improved environmental stability. However, one of the main challenges in the developing of the nanocomposites is the incompatibility of the nanomaterial with the polymer matrix, leading to problems such as particles aggregation and lower fluorescence quantum yield [27]. Recently, several studies demonstrate the importance to combine nanoparticles and well defined supports i.e. silver, titanium dioxide and zinc oxide on wool fibers [28,29,30] or gold nanoparticles on fiber-optic [31].

§ 1.2. Doped YAG materials

Yttrium Aluminum Garnet (YAG, with chemical formula $Y_3Al_5O_{12}$) has emerged as the most widely produced laser gain host and has enjoyed recent popularity as a substrate material for optical components. The YAG host is a stable compound, mechanically robust, physically hard, optically isotropic, and transparent from below 300 nm to beyond 4 microns.

The garnet structure was firstly reported by Menzer [32] according to Geller [33].

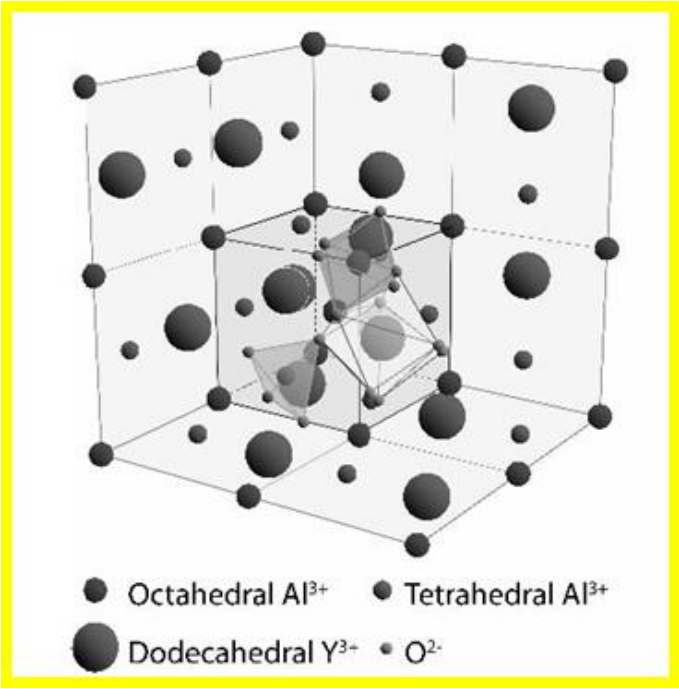

Figure 1.3. YAG crystal lattice. The Cerium ions substitute some yttrium ions in their positions.

Generally, the energy levels of the activator ions in phosphors can determine excitation and emission properties which are directly related to the 4f and 5d energy levels. For the specific case of Ce:YAG, the cerium ions can substitute the yttrium ions in theirs lattice position. The amount of cerium ions established the doping ratio. The energy of 4f–5d1 transitions is around 2.7 eV, i.e., in the visible range, which may be compared to the 4f–5d transitions for a free Ce^{3+} (6.12 eV), which is in the UV range [34].

As oxide, doped:YAG can be obtain as single crystal, powder and nanopowder.

The single crystal having good optical, chemical and mechanical characteristics is applied in laser applications. Crystals are usually grown by the conventional Czochralski (CZ) technique which can involve the production of lattice cavities or heterogeneous doping agent distribution [35]. These negative factors, corroborate to the high cost production and the difficulty to reach high crystal dimension, have encouraged the development of new approach for the preparation of massive

material maintaining their good optical performances. In order to get new opportunities researchers are projecting new materials such as ceramics and composites, starting from powders.

The solid-state reaction is the most common method of obtaining micrometric phosphors for optoelectronic application. The solid-state reaction involves physical mixing of the raw materials followed by a high temperature treatment (over 1500 °C) at long time reaction because of the refractory nature of the oxide precursors, for this reason the shape, size, and distribution of the particles are hardly controlled [36,37].

The particles dimension is often reduced by the ball milling procedure. Sometimes additive are also added to improve the disperdibility in a medium. There are several producers which sell doped YAG phosphors, but only a few amount of information about these products are given.

The use of YAG nanophosphor doped with lanthanides generated a lot of contrast opinions, but their use could have a great industrial impact. It is clear that, particle size and morphology of the garnet powder play an important role with respect to resin incorporation and optical behavior. Synthesis routes play a crucial role in the properties of the garnet nanophosphors. A variety of wet-chemical methods, sol–gel process, co-precipitation, microemulsion etc. have been developed for manufacturing nanostructured phosphors [38, 39]. These methods are many advantageous due to lower processing temperature respect to the solid –state reactions, and a better control over composition and homogeneity [40]. The control of particles size and shape is crucial and for this reason, in the last decade, researchers are hardly working on the assessment of traditional synthesis method and on the development of new ones, in order to have the possibility to tune these parameters.

Phosphors and nanophosphors cannot directly to be used for the fabrication of a device, so they have to be further processed. Recently, it was demonstrated that polymeric composites of PMMA containing Ce:YAG are an ideal yellow light emitter complementary to a blue light to the realization of a white LED on a large scale [41,42].

PMMA or Plexiglas is an amorphous, colorless thermoplastic with outstanding chemical-physical properties including optical clarity, chemical resistance (it is

resistant to many inorganic reagents, aliphatic hydrocarbons, non-polar solvents, diluted aqueous acids, and alkaline), protection against ultraviolet radiation, scratch resistance, odorless, tasteless, and nontoxic [43]. PMMA transmits light in the range 360–1000 nm almost without loss [44]. The main physical-chemical properties of PMMA are summarized in Ref. [45]. PMMA has also application in other fields, such as aircraft glazing, signs, lighting, dentures, food-handling equipment, contact lenses, substitute for inorganic glass, coating applications, and so on.

Generally, polymer nanocomposites are obtained by in situ synthesis or by dispersion (ex situ) of inorganic materials in organic matrix. In situ synthesis is based on chemical conversion of precursors in order to obtain well-organized structures. For in situ process, methods such as sol–gel, chemical vapor deposition (CVD), or spray pyrolysis can be used. Most cases of ex situ synthesis require the bulk material to be patterned or broken down into smaller pieces using physical methods. Different methods can be used for dispersing inorganic nanoparticles into polymer matrix: direct mixing of the nanopowders into a polymeric matrix (in solution or in melt), in situ polymerization in the presence of the nanoparticles previously obtained or in situ synthesis of inorganic nanoparticles in the presence of polymer, and in situ synthesis where both inorganic and organic components are formed together [46].

Ce:YAG -encapsulated PMMA composite particles were also produced by electro-hydrodynamic atomization. The Ce:YAG particles were added to a solution of PMMA in DMF [47].

§ 1.3. Thesis objective

wLEDs have advantage such as higher energy efficiency, higher reliability, longer life, faster response, and lower pollution compared to traditional lighting. It is suggested that they have a prosperous future in the lamp market. One of the weakness of this device is the conversion of blue light to the other component, in order to give a pure white light with high efficiencies.

In this step it is required an high and tuned photons conversion and a reduced scattering phenomenon. One limit is that the radiation diffusion on the particle

surfaces reduces the wLED efficiency. There are several materials produced for this purpose [17,21], but it is difficult to reach a good compromise between the requirements.

The development of luminescent nanomaterials, having high performances useful for white LED, is one of the opened challenge in the research field.

Ce:YAG composites are a good solution for the photons conversion due to the high quantum efficiency of the phosphor. Several authors [20] demonstrated the possibility to tuning the optical properties of the composites by changing the dispersing medium. Otherwise the particles dimension of the phosphor has a relevant effect on the scattering phenomena. It was suggested that nanophosphors be utilized to increase the transmission and to reduce the optical scattering loss [48,49]. The particle scattering scales as the square of the particle mass; therefore, the reduction of particle size to the nanoscale range should essentially eliminate the scattering. The obtained material is a so called nanophosphor.

The **goal** of the thesis is the development of luminescent composites and nanocomposites based on Ce:YAG, having high performances useful for white LED, pointing to the tailoring of their optical properties by choosing proper methodology of preparation.

Composites have been prepared preliminary in order to evaluate the effects of polymeric matrix, such as PMMA and PC (chosen for their mechanical and transparencies properties), and Ce:YAG quantity on the luminescent properties.

The goal has been reached developing nanophosphors synthesis methods able to control at the same time particles size and optical properties. The syntheses were developed by systematically varying several parameters in order to evaluate their effect on nanophosphors properties.

The best obtained nanophosphor has been used in the preparation of the nanocomposites to verify their application in a wLED device.

Furthermore, in the view of a possible scale up of the materials production, the preparations have been planned with respect the low cost, eco-sustainability and high yield of the process.

References

[1] F. Seitz, Luminescent Crystals, in "preparation and characteristics of Solid Luminescent Materials. Pub: John Wiley & Sons, inc, NY, p.1 (1948).

[2] C. Feldmann, T. Jüstel, C.R. Ronda, P.J. Schmidt Advanced Functional Materials, 13 (7) (2003) 511–516.

[3] Z. Zhao, J.W.Y. Lam, B.Z. Tang, Journal of Materials Chemistry, 22 (2012), 23726-23740.

[4] G. Blasse, B. C. Grabmaier, "Luminescent materials" Springer Verlag, Berlin, Heidelberg, (1994) 11.

[5] M.K. Tsang , G. Bai , J. Hao , Chem. Soc. Rev., 44 (2015), 1585.

[6] Y. Zhang , J. H. Hao , J. Mater. Chem. C, 1 (2013), 5607.

[7] X. He, X. Liu, R. Li, B. Yang, K. Yu, M. Zeng, R. Yu, Scientific Reports 6 (2016) 22238.

[8] G. Bai, M.K. Tsang, J. Hao, Adv. Funct. Mater., 26 (2016), 6330–6350.

[9] W. Feng , C. M. Han , F. Y. Li , Adv. Mater., 25 (2013), 5287.

[10] L. D. Carlos, R. A. S. Ferreira , V. d. Z. Bermudez , B. Julian-Lopez , P. Escribano , Chem. Soc. Rev., 40 (2011), 536.

[11] Y.S. Lin, S.H. Wu, Y. Hung, Y.H. Chou, C. Chang, M.L. Lin, C.P. Tsai, C.Y. Mou, Chem. Mater., 18 (22) (2006), 5170–5172.

[12] E. Chelebaeva, J. Larionova, Y. Guari, R. A. Sá Ferreira, L. D. Carlos, F. A. Almeida Paz, A. Trifonov, C. Guérin, Inorg. Chem., 47 (3) (2008), 775–777.

[13] S. Nakamura, T. Mukai, and M. Senoh. Applied Physics Letters, 64 (1994),1687–1689.

[14] Y.C. Lin, M. Karlsson, M. Bettinelli, Top Curr Chem (Z) 374 (2016), 21.

[15] R. Zhang, H. Lin, Y. Yu, D. Chen, J. Xu, and Y. Wang, Laser Photonics Rev. 8 (2014) 158.

[16] L.D. Carlos, R.A. S. Ferreira , V.d.Z. Bermudez , B. Julian-Lopez , P. Escribano , Chem. Soc. Rev., 40 (2011), 536.

[17] A. Maître, C. Sallé, R. Boulesteix, J.F. Baumard, Y. Rabinovitch, Ceramics, 91(2) (2008) 406–413.

[18] J. Liu, L. Lin, J. Li, J. Liu, Y. Yuan, M. Ivanov, M. Chen, B. Liu, L. Ge, T. Xie, H. Kou, Y. Shi, Y. Pan, J. kun Guo, Ceramics International, 40(7) (2014) 9841-9851.

[19] R. Zhang, H. Lin, Y. Yu, D. Chen, J. Xu, Y. Wang, Laser & photonics Review, 8(1) (2014), 158–164.

[20] S. Nakamura, G. Fasol, Springer, Berlin, (1997).

[21] S. Ye, F. Xiao, Y. X. Pan, Y. Y. Ma, and Q. Y. Zhang, Mater. Sci. Eng., 71 (2010), 1–34.

[22] H.J. Byun, W.S. Song, Y.S. Kim, H. Yang, , J. Phys. D. Appl. Phys., 43 (2010), 195401.

[23] J. Ryszkowska, E. Zawadzak, D. Hreniak, W. Strek, K.J. Kurzyd£owski, Polimery, 52 (2007), 340.

[24] A. Jusza, K. Anders, P. Polis, R. Stepien, L. Lipinska, R. Piramidowicz, Opt. Mater., 36 (2010), 1749-1753

[25] N. Francolon, A. Potdevin, D. Boyer, G. Chadeyron, R. Mahiou, Ceram. Int., 41 (2015), 11272-11278.
[26] F.V. Hajiyeva, M.A. Ramazanov, A.M. Maharramov, Nanomedic Nanotechnol (2015), S7.
[27] V. M. Diep, A.M. Armani, Nano Lett., 16 (12) (2016), 7389–7393.
[28] M. K. Fern, H. James ACS Appl. Mater. Interfaces, 3 (2011), 1083–1092.
[29] H. Zhang, K. R. Millington, X. Wang, Polymer Degradation and Stability, 94(2) (2009), 278-283.
[30] A. Becheri, M. Dürr, P. Lo Nostro, P. Baglioni Journal of Nanoparticle Research, 10(4) (2008), 679–689.
[31] B.Y. Hsieh, Y.F. Chang, M.Y. Ng, W.C Liu, C.H. Lin, H.T. Wu, C. Chou, Analytical Chemistry, 79 (9) (2007), 3487-3493.
[32] G. *Z.* Menzer, *Kristallogr.*, *69* (1928), 300.
[33] S. Geller, Z Kristallogr, 125 (1967), 1–47.
[34] P. Dorenbos, J Lumin, 34 (2013), 310–318.
[35] B. Cockayne, J. Am. Ceram. Soc., 49 (1966), 204–207; b) J. L. Caslavsky, J. D. Viechnicky, J. Mater. Sci., 15 (1980), 1709–1718 ; c) C. D. Brandle, L.R. Barns, J. Cryst. Growth, 26 (1974), 169–170.
[36] C.C. Lin, Y.S. Zheng, H.Y. Chen, C.H. Ruan, G.W. Xiao, R.S. Liu, J Electrochem Soc, 157(9) (2010), H900–H903.
[37] H. Shi, C. Zhu, J. Huang, J. Chen, D. Chen, W. Wang, F. Wang, Y. Cao, X. Yuan, Opt Mater Express, 4(4) (2014), 649–655.
[38] P.A. Tanner, L. Fu, L. Ning, B.M. Cheng, M.G. Brik, J Phys, 19 (2007), 216213–216227.
[39] X. Li, B. Zheng, T. Odoom-Wubah, J. Huang, Ceram Int, 39 (2013), 7983–7988.
[40] V. Tucureanu, A. Matei, I. Mihalache, M. Danila, M. Popescu, B. Bita, Journal of Materials Science, 50(4) (2015), 1883–1890.
[41] M. L. Saladino, D. F. Chillura Martino, M. A. Floriano, D. Hreniak, L. Marciniak, W. Stręk, E. Caponetti, J Phys. Chem C, 118 (2014), 9107.
[42] M. L. Saladino, A. Zanotto, D. F. Chillura Martino, A. Spinella, G. Nasillo, and E. Caponetti, Langmuir, 26 (2010), 13442.
[43] W. Brostow, M. Dutta, J. Ricardo de Souza, P. Rusek, A. Marcos de Medeiros, E.N. Ito, Express Polym Lett., 4(9) (2010), 570–575.
[44] S. Gross, D. Camozzo, V. Di Noto, L. Armelao, E. Tondello Eur Polym J, 43 (2007), 673–696.
[45] J.E. Mark (ed) Polymer data handbook. Oxford University Press, New York (1999).
[46] T.E. Motaung, A.S. Luyt, F. Bondioli, M. Messori, M.L. Saladino, A. Spinella, G. Nasillo, E. Caponetti, Polym Degrad Stabil 97 (2012), 1325–1333.
[47] C.J. Jr Hogan, K.M. Yuna, D.R. Chenb, I.W. Lenggoroc, P. Biswasb, K. Okuyama Coll Surf A, 311 (2007), 67.
[48] Y. X. Pan, W. Wang, G. K. Liu, S. Skanthakumar, R. A. Rosenberg, X. Z. Guo, K.K. Li, J. Alloys Compd., 488 (2009), 638-642.
[49] H. Yang, D. K. Lee, Y.S. Kim, Mater. Chem. Phys., 114 (2009), 665–668.

CHAPTER II

Ce:YAG polymeric composites

The first step of the research was the preparation of composites by using commercial Ce:YAG phosphor as filler and PolyMethylMethacrylate (PMMA) and (PolyCarbonate) PC as dispersing medium. The melt mixing method has been selected on the view of a scaling up of the process for the production of this material and processing on devices.

§ 2.1. Preparation by melt mixing

Several Ce:YAG-polymer composites were prepared with different amounts of Ce:YAG in the range 0.1-5 wt.%. The structure, morphology and optical properties were studied. The composites were combined with a blue LED in order to test their performance in a white LED device.

PMMA or PC pellets and Ce:YAG powder were dried in an oven at 80 °C for 12 hours before use. All composites were prepared by mixing the polymer and filler in a Brabender Plastograph 50 mL internal mixer at 200 °C and 50 rpm for 10 minutes. For the preparation of the composites, PMMA or PC was first melted for 2 minutes at 200 °C, and different amount (0.1, 0.3, 0.5, 1, 2 and 5 wt. %) of the Ce:YAG powders were added into the molten polymer and mixed for a further 8 minutes. The samples were then melt pressed into 3 mm thick sheets at 200 °C for 5 minutes at 50 bar.

The samples were then melt pressed into 3 mm thick sheets at 200 °C for 5 minutes at 50 bar. Pure PMMA and PC, as a control samples, were prepared following the same procedure.

Yellow solid products, composed of the PMMA or PC polymeric matrix containing Ce:YAG particles, were obtained (Figures 2.1 and 2.2). The composites remained transparent up to 2 wt.% of Ce:YAG in PMMA and up to 1 wt.% of Ce:YAG in PC .

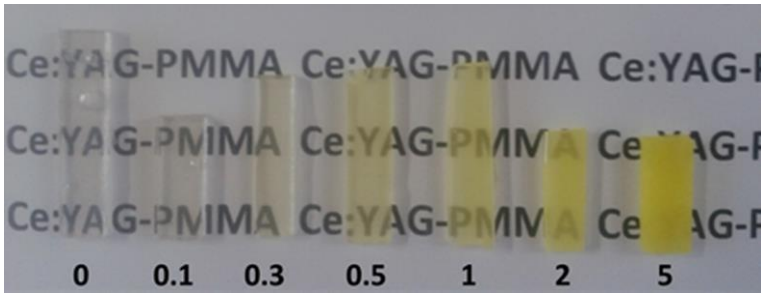

Figure 2.1. Photo of the obtained PMMA composites at different Ce:YAG amount (0-5 wt.%).

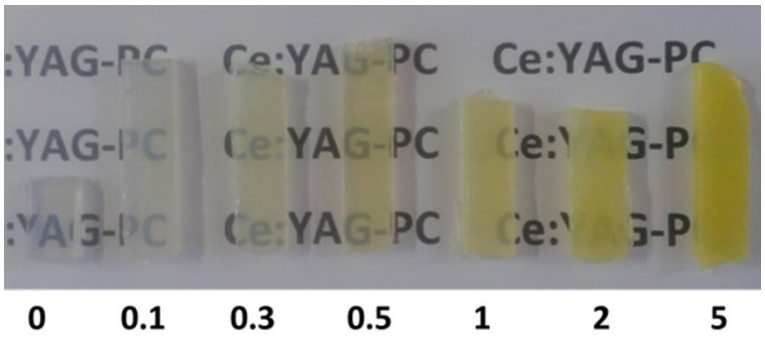

Figure 2.2. Photo of the obtained PC composites at different Ce:YAG amount (0-5 wt.%).

§ 2.2. Effect of the Ce:YAG amount in PolyMethylMethacrylate matrix

The WAXS patterns of the Ce:YAG, PMMA and the Ce:YAG-PMMA composites were obtained and reported in Figure 2.3.

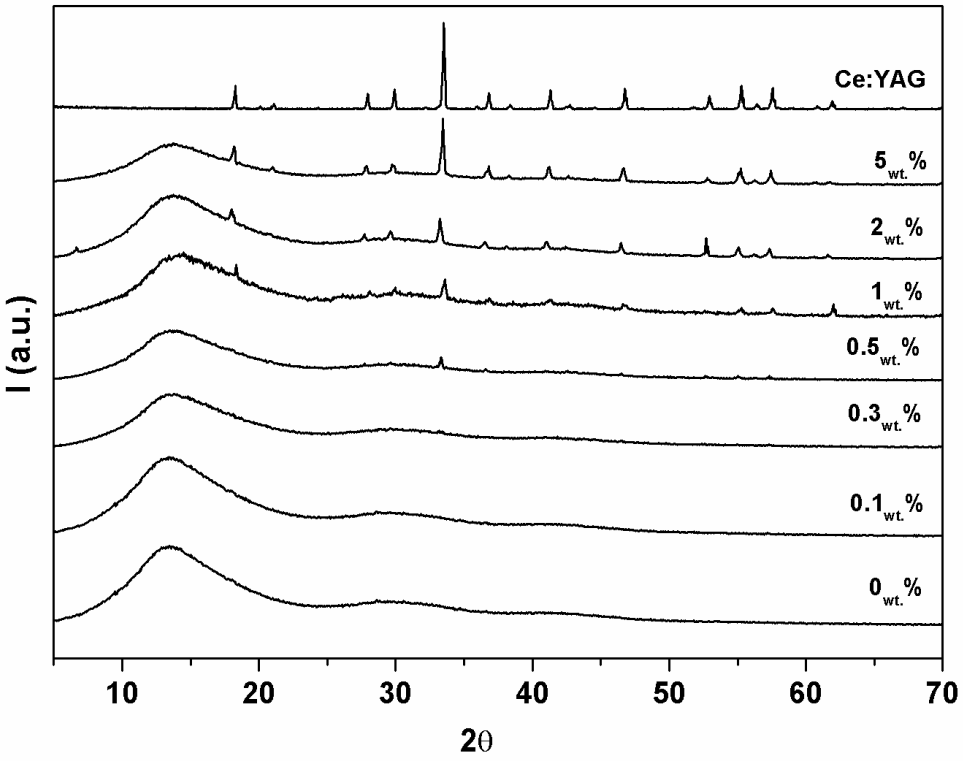

Figure 2.3. WAXS patterns of Ce:YAG, PMMA and Ce:YAG-PMMA composites.

The diffraction pattern of the Ce:YAG powder is typical for the garnet phase. The diffraction pattern of PMMA shows a broad diffraction peak band centred around 14°, typical of an amorphous material, together with two bands of lower intensities centred at 29.7° and 41.7°, in line with previously reported results [1, 2, 3, 4]. The first band reflects the ordered packing of polymer chains while the second and third one denote the ordering inside the main chains with their intensity systematically decreasing [5]. The diffraction pattern of the composites loaded with 0.1 and 0.3 wt.% are similar to that of the pure PMMA. A low intensity diffraction peak appears at 33° in the pattern of the composite loaded with 0.5 wt.% Ce:YAG. All the peaks of the garnet phase, with intensities increasing with increasing amount of Ce:YAG, are present in the WAXS patterns of the composites loaded with 1, 2 and 5 wt.% Ce:YAG. No shift in the position of the garnet phase peaks with respect to the powder was observed, thus confirming that no structural modification occurred in the filler when

it was embedded in the polymer. No change in the cell parameter of the garnet phase was observed.

The Ce:YAG-PMMA composites loaded with 0.5 and 5 wt.% Ce:YAG were analysed with TEM to investigate the distribution of the particles in the polymer. Some of the TEM micrographs, taken at different magnifications, of the Ce:YAG-PMMA composites loaded with 0.5 and 5 wt.% Ce:YAG are shown in Figure 2.4.

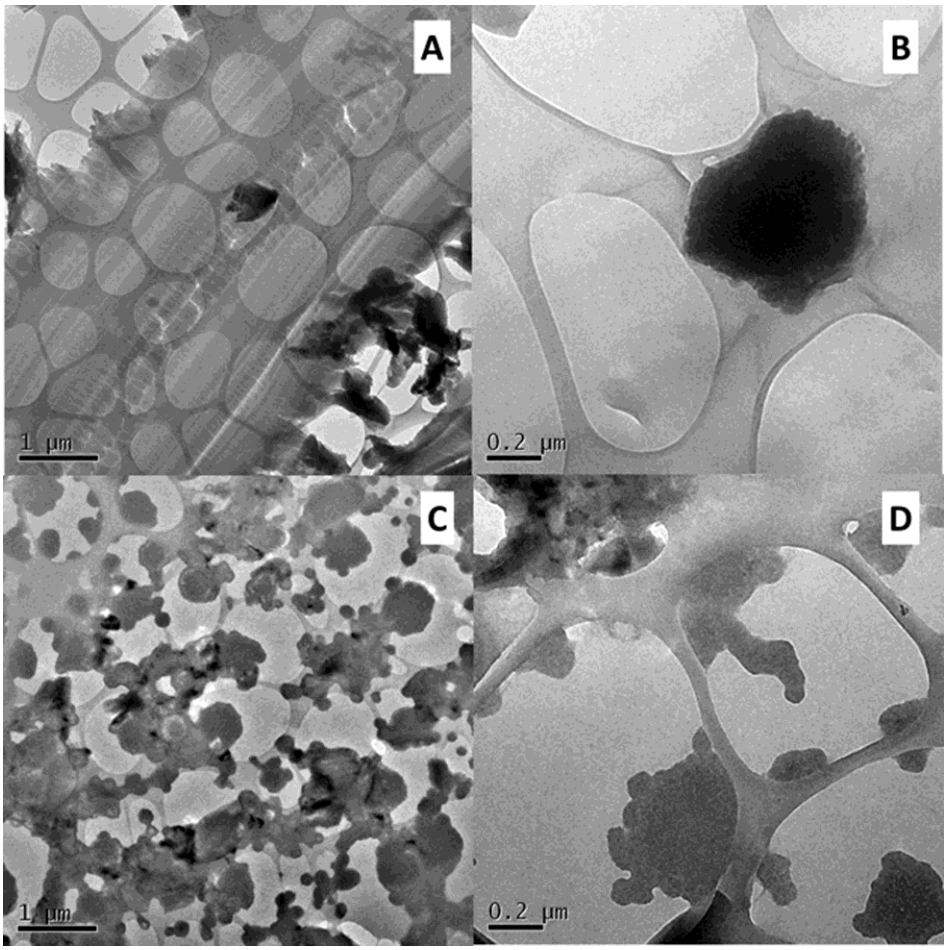

Figure 2.4. TEM micrographs of Ce:YAG-PMMA composites (A-B) 0.5 wt.% (C-D) 5 wt.% at two magnifications.

The Ce:YAG particles maintained the same mean size (~ 0.5 µm) in all the analysed samples. Being the filler commercially available, and knowing that the particles size

of the filler is of few μm (polydispersion in the range 0.1 -2 μm), it is possible to assert that the size of the filler is not influenced by the preparation method we used.

The particles formed clusters uniformly dispersed in the composite, but their distribution was significantly different. For the 0.5 wt.% composite, isolated clusters were present, while for the 5 wt.% composite a more homogeneous dispersion of clusters was observed.

^{13}C {^{1}H} CP-MAS NMR measurements were performed to understand the possible changes of the polymeric chains caused by the presence of Ce:YAG in the polymer and to investigate the interactions between the two components. The ^{13}C {^{1}H} CP-MAS NMR spectra of PMMA and the Ce:YAG-PMMA composites, and the assignment of the ^{13}C chemical shifts of the polymer are reported in Figure 2.5.

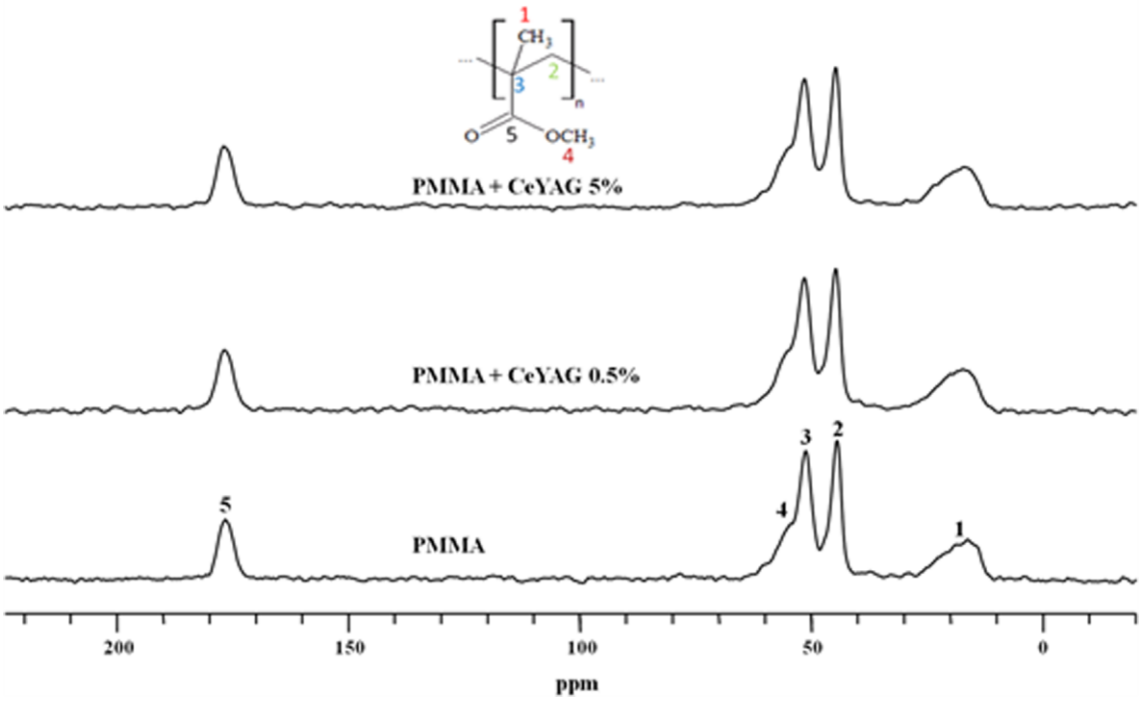

Figure 2.5. ^{13}C {^{1}H} CP-MAS NMR spectra of PMMA and of Ce:YAG-PMMA composites.

All the spectra show five resonance peaks at 177.9, 55.4, 52.3, 45.2 and 16.6 ppm due to respectively the carbonyl carbon, methoxyl group, the quaternary carbon of the polymer chain, and the methylene and methyl groups. No modification in the chemical shift and in the signal shape was observed in the presence of Ce:YAG. This

confirmed that there were no chemical interactions and that only physical interactions occurred between the polymer and the Ce:YAG particles.

In order to investigate possible molecular interactions between the components, and to detect dynamic changes in the polymer induced by the presence of Ce:YAG, the proton and carbon spin lattice relaxation times in the rotating frame, $T_{1\rho}(H)$ and $T_{1\rho}(C)$, were determined through solid-state NMR measurements. Both the $T_{1\rho}(H)$ and $T_{1\rho}(C)$ values give information about molecular motions in the kHz range [1,2,3]. These motions reflect the dynamic behaviour of a polymeric chain in a range of a few nanometers. However, for natural-abundance experiments the spin diffusion is less effective in the $T_{1\rho}(C)$ averaging, and this parameter is therefore a good probe for local mobility. The $T_{1\rho}(H)$ and $T_{1\rho}(C)$ values obtained from each peak in the ^{13}C spectra of all the samples are reported in Table 2.1.

Table 2.1. Relaxation time values for all the peaks in the ^{13}C spectra of PMMA and of Ce:YAG-PMMA composites loaded with 0.5 and 5 wt.% Ce:YAG.

Carbon	ppm	$T_{1\rho}H$ (ms)			$T_{1\rho}C$ (ms)		
		PMMA	Ce:YAG-PMMA (0.5 wt.%)	Ce:YAG-PMMA (5 wt.%)	PMMA	Ce:YAG-PMMA (0.5 wt.%)	Ce:YAG-PMMA (5 wt.%)
1	177.9	14.3 (2)	16.1 (2)	33.5 (2)	31 (3)	24.8 (2)	16.4 (3)
2	55.4	-	21.5 (2)	-	41.0 (2)	4.6 (4)	6.4 (3)
3	52.3	25 (1)	11.8 (1)	54.4 (3)	62.6 (4)	17 (2)	16 (2)
4	45.2	13.4 (1)	9.5 (3)	15.8 (2)	65.3 (2)	14.9 (2)	16.2 (1)
5	16.6	15.2 (2)	15.7 (4)	16 (3)	17.0 (1)	19.6 (2)	24.4 (2)

The calculated $T_{1\rho}(H)$ values for all the peaks in PMMA are of the same order of magnitude. The similar relaxation times for the proton bound to the corresponding carbon atoms indicate that no specific interactions occurred. As a consequence, the material can be considered homogeneous to the length scale of a few nanometers. The

loading of 0.5 wt.% Ce:YAG in PMMA does not cause any appreciable change to the above parameter, thus indicating that this concentration is unable to modify the dynamic behaviour of the polymer. Different behaviour was observed for the composite loaded with 5 wt.% Ce:YAG, where the $T_{1\rho}(H)$ values were strongly affected by the presence of the filler. There was an obvious increase in the $T_{1\rho}(H)$ values for signals 1 and 3, compared to the ones of the pure PMMA. These longer relaxation times can be ascribed to a local stiffness (within a few nanometer length) as a result of the presence of the filler.

The calculated $T_{1\rho}(C)$ values vary a lot between the different samples and relaxation peaks, and there is no trend. However, for both composites these values were strongly affected by the presence of the Ce:YAG particles. This indicates that a minor contribution to the $T_{1\rho}$ relaxation arises from each molecular group that modulates the $^{1}H-^{13}C$ dipolar coupling. A bigger decrease was observed for the 2, 3 and 4 carbons. These variations can account for specific interactions between the polymer and the surfaces of the Ce:YAG particles. In fact, in agreement with a previous finding [6,7], an electron donor-acceptor interaction between the carboxyl oxygen lone pair and the surface yttrium or cerium ions could take place. This specific interaction can account for the observed variations in the relaxation time due to the retrieval of electrons along the polymer chain.

The excitation and emission spectra of Ce:YAG powder, of PMMA and of Ce:YAG-PMMA composites, measured at room temperature, are reported in Figure 2.6.

The excitation spectrum of the Ce:YAG powder show a large band centred at 460 nm and assigned to the $2F_{5/2} \rightarrow 5d_2$ absorption transition, as expected. No band is observed in the pure PMMA. The excitation spectra of the Ce:YAG-PMMA composites show the same large band which intensity increase with an increase in the amount of Ce:YAG.

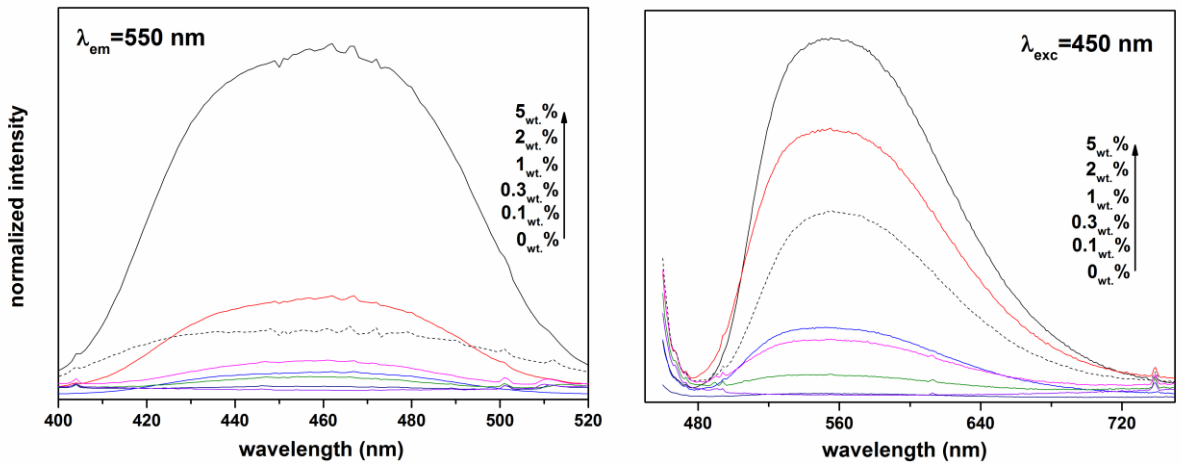

Figure 2.6. Excitation (left) and emission (right) spectra of Ce:YAG powder (dash), PMMA and Ce:YAG-PMMA composites (lines).

The emission spectra of the powder and of the composites were recorded using λ_{exc} = 450 nm as excitation wavelength which well matches the lowest energy $5d_1$ band of Ce^{3+}. In all case, the asymmetric spectra consist of a very broad band located around 550 nm associated with the 5d (2A1g)→4f ($2F_{5/2}$ and $2F_{7/2}$) transitions of Ce^{3+}. No band is observed in the pure PMMA. In the composites, the band intensity increases with the amount of Ce:YAG. Since it is well known that the luminescent intensity is related to the average distance between luminescent centres [8], this could be due to the concentration of Ce:YAG in the polymer. However, the maximum emission wavelength (λ_{max}) significantly changed and a shift of 15 nm was observed increasing the Ce:YAG amount, as reported in Figure 2.7. The value of λ_{max} of the Ce:YAG-PMMA loaded at 2 and 5wt.% is equal to the ones of the Ce:YAG powder.

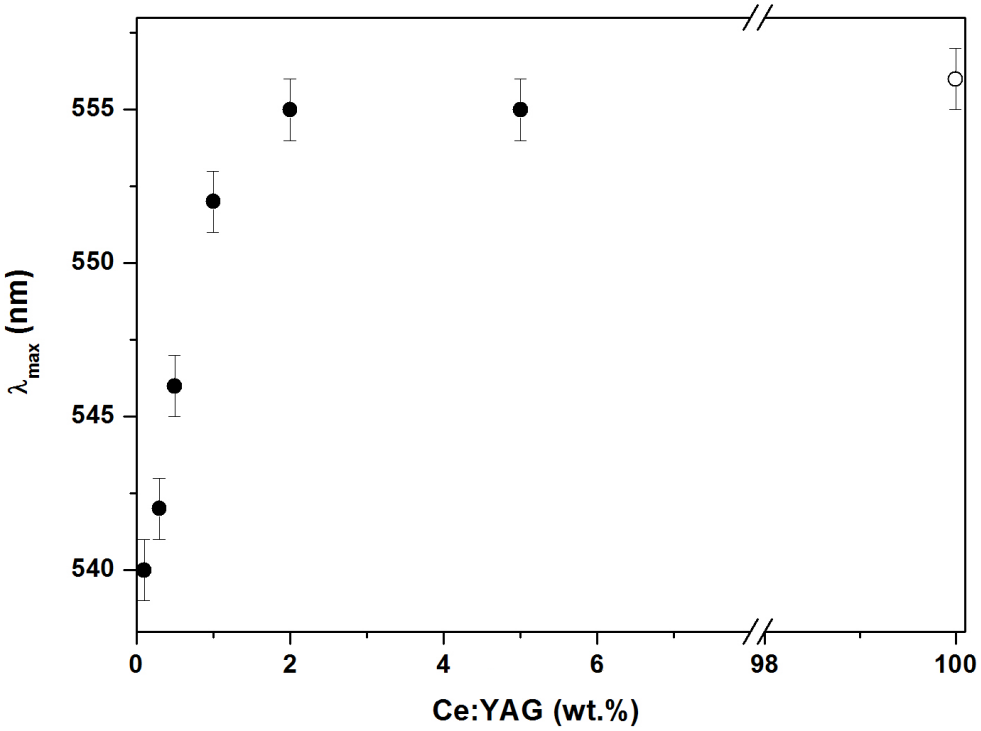

Figure 2.7. Position of the maximum of the emission band of the Ce:YAG powder (○) and of Ce:YAG-PMMA composites (●) as function of Ce:YAG amount.

This finding cannot to be ascribed to any significant shifts of the excitation bands, indicating that the shift of the emission band does not come from any significant variations in the energy position of the 5d electronic states of the Ce^{3+} ions, both in terms of their population and type. The crystalline structure is the same for each sample indicating that the observed shift in the emission band is not due to Ce:YAG modifications. Bhat et al. [9] demonstrated that the emission bands of phosphors can be tuned by varying the optical properties of the matrix. The interactions observed by NMR study can modify the probability of an electron transition between the electronic states. In my opinion, on the basis of these speculations, the observed shift was probably the result of specific interactions between the polymer chains and the Ce:YAG filler particles.

The quantum yield of the Ce:YAG powder and Ce:YAG-PMMA composites loaded with 5 wt.% were determined by using the integer sphere.

The values are 90.2% for the powder and 89.5% for the composite, they are very high and the similitudes indicate that the polymer doesn't affect this parameter.

2.2.1. Application of composite in White LED device

The Ce:YAG-PMMA composites were combined with a blue LED in order to test the composite efficiency and to verify its potential use as a white light source. The emission spectra and the relative CIE 1931 colour space of the resulting lights are reported in Figures 2.8A and 2.8B, respectively.

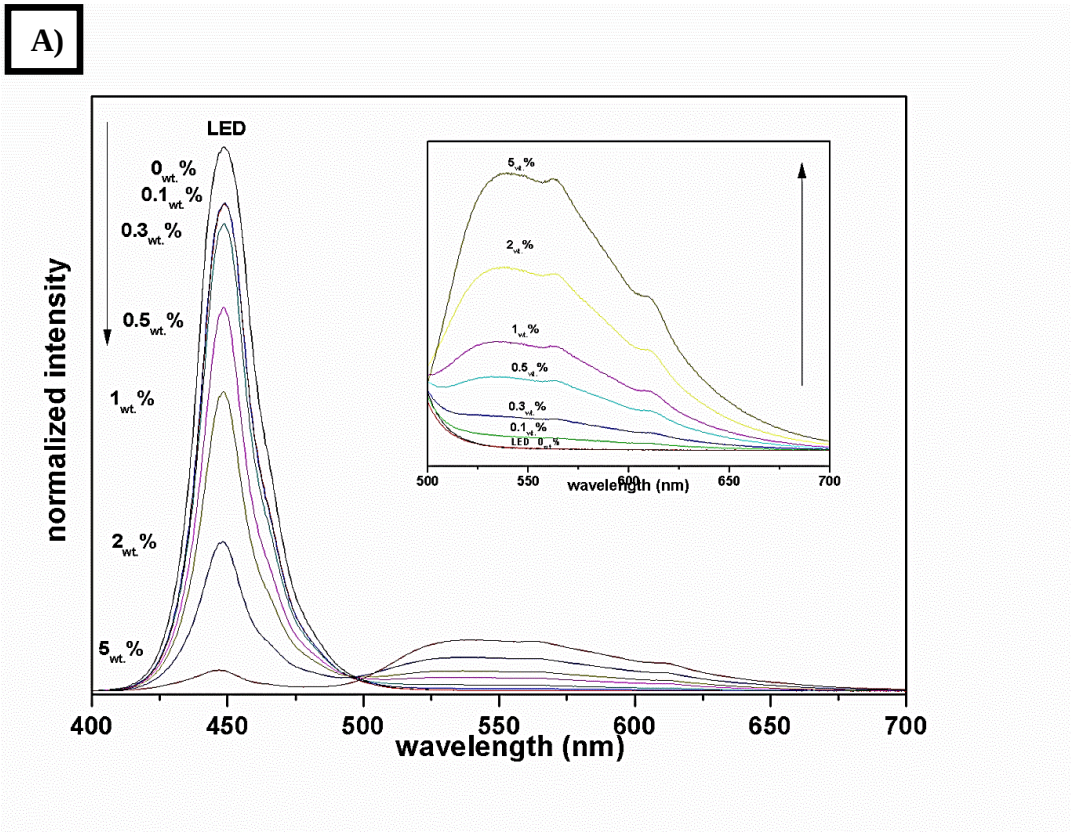

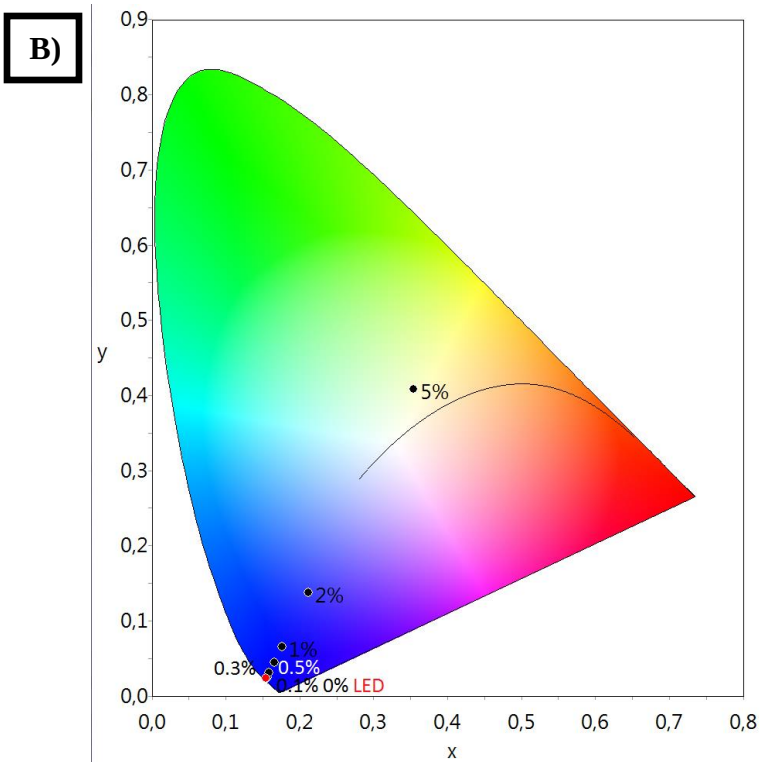

Figure 2.8. (A) Emission spectra and (B) and the relative CIE 1931 colour space of the resulting light.

The emission spectrum of the resulting light constitutes of two bands. The first, centred at 450 nm, is due to the blue LED, and the second one, centred at 550 nm, is due to the emission of the composite. The results show that by increasing the amount of Ce:YAG in the composite, the emission intensity at 450 nm decreased, while that at 550 nm increased.

The chromaticity coordinates, calculated from the emission spectra of the resulting lights, are reported in the Commission Internationale de l'Eclairage (CIE) chromaticity diagram (Fig. 2.8B). The CIE (x, y) coordinates of the lights obtained combining the blue LED with the composites loaded with up to 2 wt.% Ce:YAG are located in the blue region. Those of the lights obtained combining the blue LED with the composites loaded with 5 wt.% Ce:YAG are located in the white region. This composite is therefore more suitable for a white LED device. The reason of the observed behaviour could be ascribed to better balance of light between the emission from blue LEDs and the emissions from phosphor necessary to obtain white light

with proper colour rendering index and colour temperature [10]. The higher intensity of the emission of the Ce:YAG-PMMA loaded with 5 wt.% and the observed shift in the maximum of the band are the responsible of the better matching with the blue light of LED. This means that the good dispersion observed by TEM and the specific interactions investigated with NMR influenced the resulting light.

2.2.2. Considerations

A series of Ce:YAG-PMMA composites were prepared by melt compounding. The effect of the amount of Ce:YAG on the structure, morphology and optical properties of the composites was investigated. The results show that the particles are well dispersed in the polymer. The polymer is amorphous and the crystalline phase of Ce:YAG does not change in the composite. When increasing the amount of Ce:YAG, a shift in the emission spectrum occurred. This behavior was ascribed to electron donor-acceptor interactions between the carboxyl oxygen lone pair and the particle surface, as indicated by the changes in the relaxation times obtained by NMR.

The combination of the composites with blue LED gives the best white light for the Ce:YAG-PMMA composite loaded with 5 wt.% Ce:YAG. In this case, the obtained light better balances the light between the emission from blue LEDs and the emissions from Ce:YAG. The result clearly shows that the colour properties of light from white LEDs can be controlled by an appropriate selection of the phosphor in a composite.

§ 2.3. Effect of the Ce:YAG amount in PolyCarbonate matrix

The WAXS patterns of Ce:YAG, PC and of Ce:YAG-PC composites are reported in Figure 2.9.

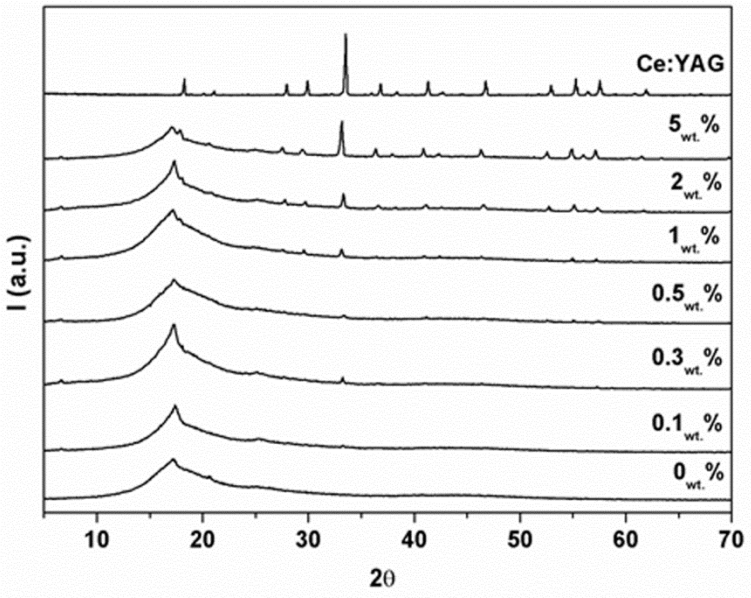

Figure 2.9. WAXS patterns of Ce:YAG, PC and Ce:YAG-PC composites.

The diffraction pattern of the Ce:YAG powder is typical of the garnet phase. The WAXS pattern of the pure PC shows a broad band centered around 17° and two bands of lower intensities typical of an amorphous material [11,12, 13].

A similar diffraction pattern is obtained for the composite loaded with 0.1 wt.% of Ce:YAG, indicating that the orientation of the PC chains was not influenced during the preparation process. The diffraction pattern of the composite loaded with 0.3 wt.% show a low intensity diffraction peak of the garnet phase. The intensity of this reflection increases with increasing Ce:YAG loading. No shift in the position of the garnet phase peaks with respect to the powder was observed, thus confirming that no structural modification occurred for the filler in the composite and that the cell parameter of the garnet phase remained unchanged.

The TEM micrographs of the Ce:YAG-PC composites loaded with 0.5 and 5 wt.% Ce:YAG are show in Figure 2.10.

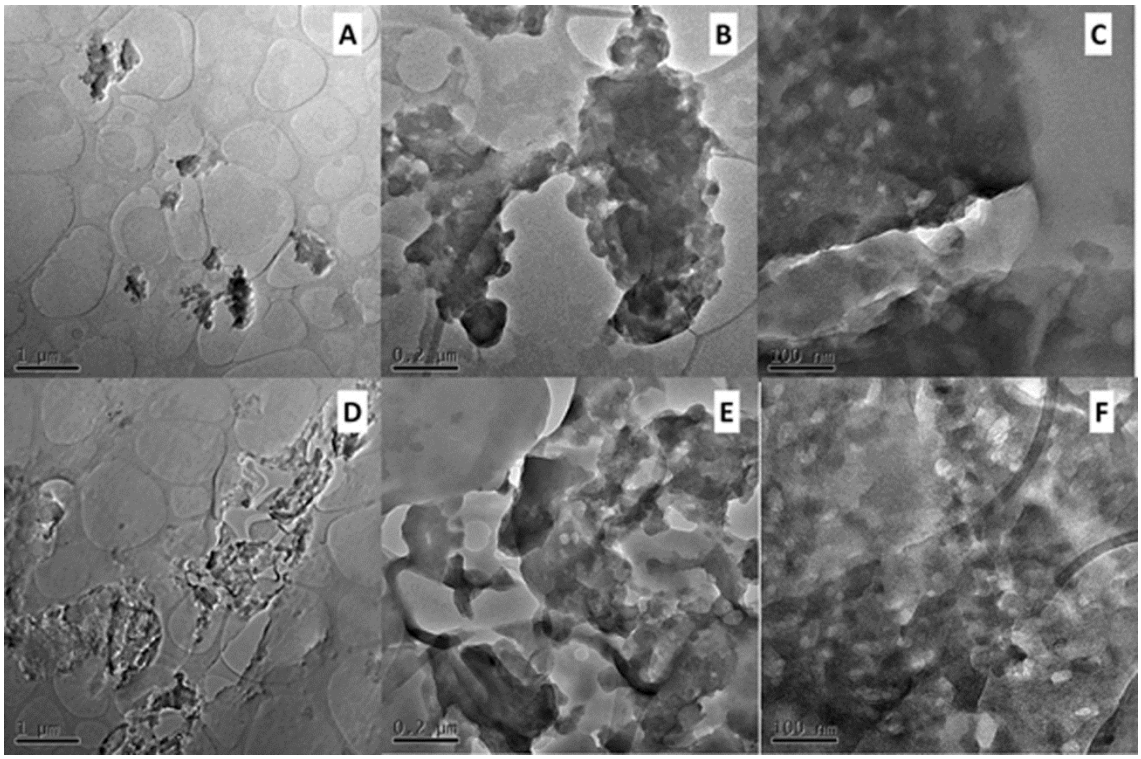

Figure 2.10. TEM micrographs of Ce:YAG-PC composites at different magnifications: (A-C) 0.5 wt.% (D-F) 5 wt.%.

The Ce:YAG particles have the same mean size in all the analyzed samples. Clusters containing several particles are uniformly dispersed in the composite. Their distribution is significantly different in the different samples. For the 0.5 wt.% composite, isolated clusters randomly distributed were present, while for the 5 wt.% composite a more uniform dispersion of clusters was observed.

^{13}C {^{1}H} CP-MAS NMR measurements were performed in order to investigate the interactions between the two components in the composites. The ^{13}C {^{1}H} CP-MAS NMR spectra of PC and the Ce:YAG-PC composites loaded with 0.5 and 5 wt.% of Ce:YAG are reported in Figure 2.11, together with the assignment of the ^{13}C chemical shifts of the polymer.

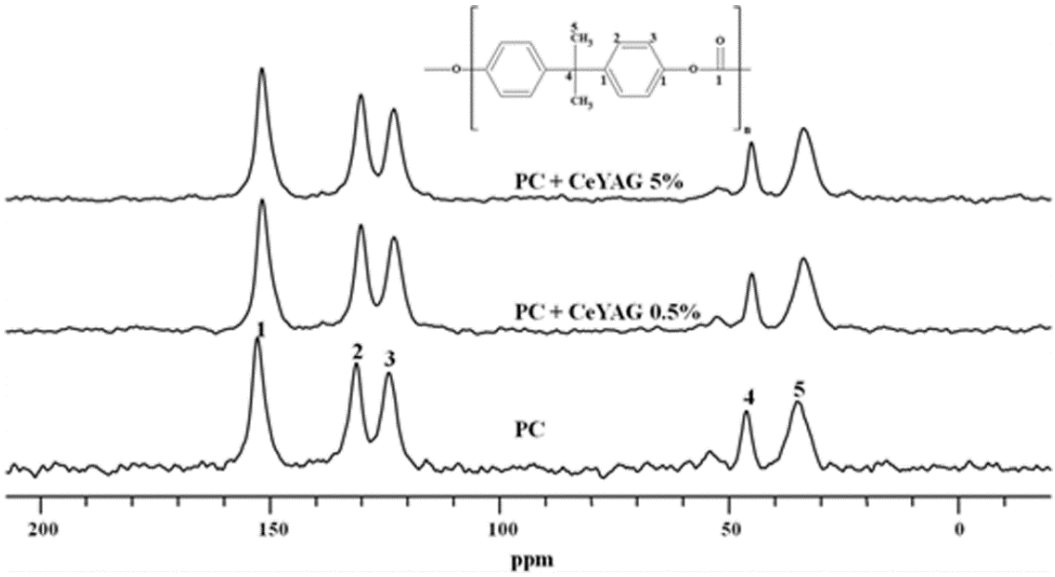

Figure 2.11. ^{13}C {^{1}H} CP-MAS NMR spectra of PC and of Ce:YAG-PC composites.

All the spectra show five resonances: peak 1 at 149 ppm is related to the quaternary carbons of the aromatic rings and to the carbonyl carbon, peak 2 at 127 ppm is related to the aromatic carbon in meta to the oxygen, peak 3 at 120 ppm is related to the aromatic carbon in ortho to the oxygen, peak 4 at 42 ppm is related to the quaternary carbon bonded to the methyl groups, and peak 5 at 31 ppm is related to the methyl carbons, according to literature [11,12,13]. No modification in the chemical shift and in the signal shape was observed in the presence of Ce:YAG. This confirmed that there was only a physical interaction between the polymer and Ce:YAG.

The proton and carbon spin lattice relaxation times in the rotating frame, $T_{1\rho}(H)$ and $T_{1\rho}(C)$, were determined through solid-state NMR measurements in order to detect dynamic changes in the polymer induced by the presence of the filler. Both the $T_{1\rho}(H)$ and $T_{1\rho}(C)$ values give information about molecular motions in the kHz range. However, for natural-abundance experiments the spin diffusion is less effective in the $T_{1\rho}(C)$ averaging, and this parameter is therefore a good probe for local mobility. The $T_{1\rho}(H)$ and $T_{1\rho}(C)$ values obtained from each peak in the ^{13}C spectra of all the samples are reported in Table 2.2.

Table 2.2. Relaxation time values for all the peaks in the ^{13}C spectra of PC and Ce:YAG-PC composites loaded with 0.5 and 5 wt.% of Ce:YAG.

		$T_{1\rho}$(H) (ms)			$T_{1\rho}$(C) (ms)		
Carbon	**ppm**	**PC**	**Ce:YAG-PC (0.5wt.%)**	**Ce:YAG-PC (5wt.%)**	**PC**	**Ce:YAG-PC (0.5wt.%)**	**Ce:YAG-PC (5wt.%)**
1	149	4.9 (2)	5.3 (3)	5.3 (3)	95.3 (3)	48.4 (4)	101 (2)
2	127.5	4.9 (2)	5.6 (1)	4.6 (3)	19 (2)	17.1 (2)	13.0 (2)
3	120	4.4 (2)	4.8 (2)	4.2 (2)	11.2 (2)	9.9 (2)	11.4 (2)
4	42	3.9 (2)	5.2 (2)	6.4 (3)	28.4 (3)	36 (2)	32.2 (2)
5	31	6.6 (3)	5.0 (3)	4.8 (2)	35 (2)	18.4 (2)	27.8 (2)

In both analyzed Ce:YAG-PC composites, the $T_{1\rho}$(H) values are of the same order of magnitude and slightly higher than those of pure PC, indicating that the materials can be considered homogeneous to the length scale of few nanometers. This is not a surprise considering the good dispersion of the particle observed by TEM.

For all the samples, the calculated $T_{1\rho}$(C) values for the different peaks randomly varied. However, for the Ce:YAG-PC composite loaded with 0.5 wt.% the $T_{1\rho}$(C) values of carbons 1 and 5 related to the quaternary carbons of the aromatic rings and to the methyl carbons were strongly affected by the presence of the Ce:YAG particles. For these signals, a decrease in values was observed, indicating that a minor contribution to the $T_{1\rho}$ relaxation arises from each molecular group that modulates the $^{1}H-^{13}C$ dipolar coupling. These variations can account for specific interactions between the polymer and Ce:YAG particles' surfaces, like electron donor-acceptor interaction between the carboxyl oxygen lone pair and the surface yttrium or cerium ions [7]. The $T_{1\rho}$(C) values of carbons 1 and 5 become similar to those of pure PC when 5wt.% of Ce:YAG is loaded. This behavior could be the resulting of a balance amongst packing tendency among aromatic rings in the pure polymer and a local disordering effect due to the establishment of the above specific interactions.

The excitation (PLE) and emission (PL) spectra of PC and the Ce:YAG-PC composites, measured at room temperature, are reported in Figure 2.12.

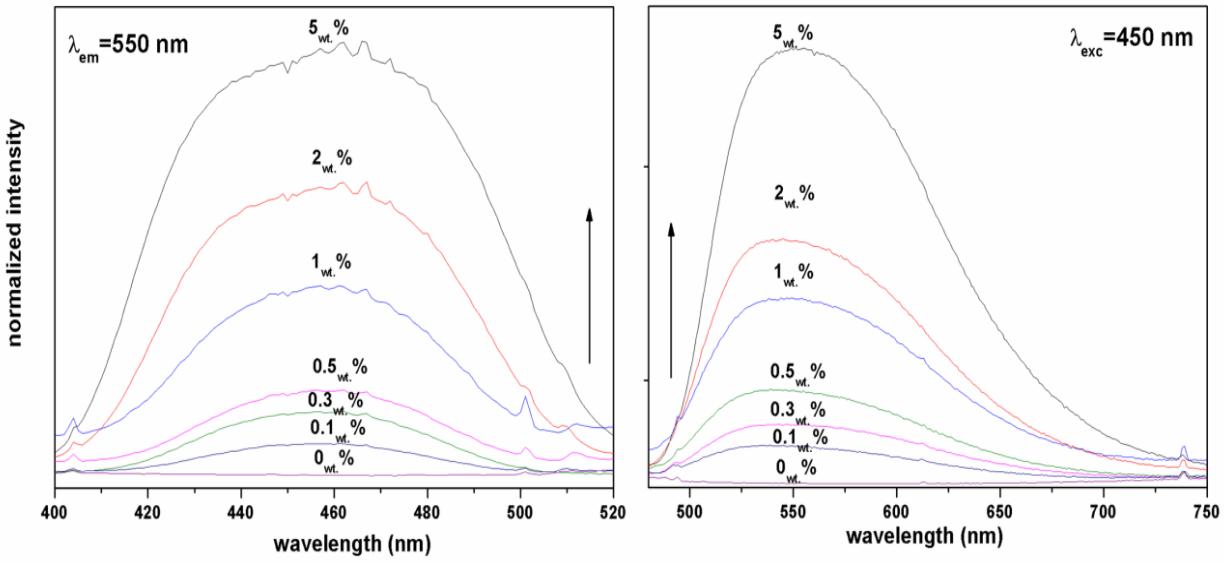

Figure 2.12. Excitation (left) and emission (right) spectra of PC and the Ce:YAG-PC composites.

The PLE spectra of the Ce:YAG-PC composites show a large band centered at 460 nm and assigned to the $^2F_{5/2} \rightarrow {}^5d_2$ absorption transition. The room temperature luminescence spectra were recorded using λ_{exc} = 458 nm as excitation wavelength, which well matches the lowest energy $5d_1$ band of Ce^{3+}. The asymmetric PL spectra consist of a very broad band located at 550 nm associated with the 5d $(2A_{1g}) \rightarrow 4f$ ($2F_{5/2}$ and $2F_{7/2}$) transitions of Ce^{3+}.

The PL intensity increased with increasing the Ce:YAG amount in the composite. The maximum emission wavelength changed significantly, and a red shift of 14 nm was observed, as reported in Figure 2.13.

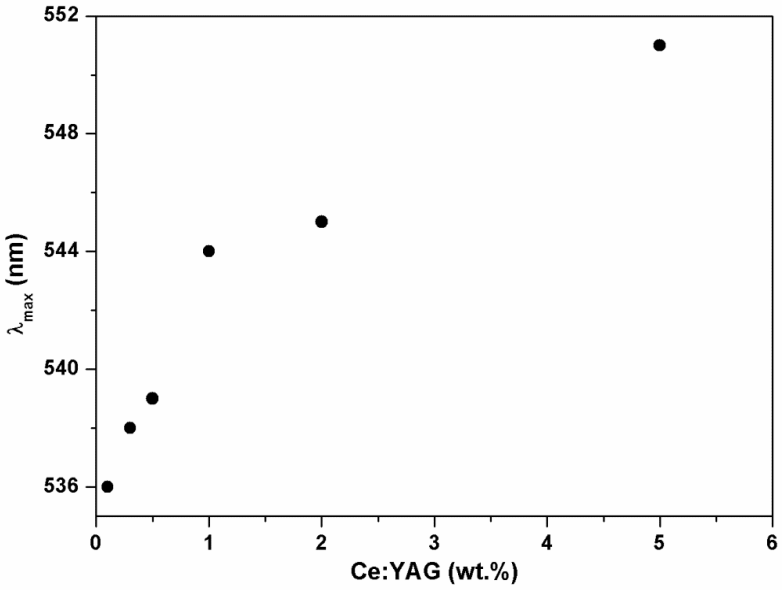

Figure 2.13. Position of the maximum of the emission band of the Ce:YAG-PC composites.

Considering the WAXS pattern of the composites, the observed red shift cannot be attributed to lattice distortions. Blasse and Brill [14] reported that the emission band shift can be due to a lowering of the 5d energy level of Ce^{3+}. In Ce^{3+} the interaction between the 5d-electron and the chemical surrounding can affect the level energies. It is possible that the presence of the polymer on the surface changed the environment around the Ce:YAG through its interaction with the filler, those causing the observed shift. Generally, as suggested by Chen et al., a red-shift in the spectrum has a significant influence on the luminescent properties of white LED [15]. However, Bhat et al. observed a blue-shift in the emission maximum with an increase in the refractive index [9]. Similar shift in the PL spectrum was observed in the composite Ce:YAG-PMMA prepared by *in situ* polymerization [6]. In that case, the composite derived by a polymerization of a mixture of methyl methacrylate (MMA) and 2-methacrylic acid (MAA) monomers. The different effect we are observing could be attributed to differences in the preparation method of the composite.

The quantum yield of the Ce:YAG-PC composites loaded with 2 wt.% was determined by using the integer sphere. The value is 89.9%. It is very high and similar to the powder one (90.2%).

2.3.1. Application of composite in White LED device

White LEDs were thus prepared by combining a blue LED and the prepared Ce:YAG-PC composites. The emission spectra of the resulting light obtained by combining the Ce:YAG-PC composites with a blue LED and the relative CIE 1931 color space are reported in Figures 2.14A and 2.14B, respectively.

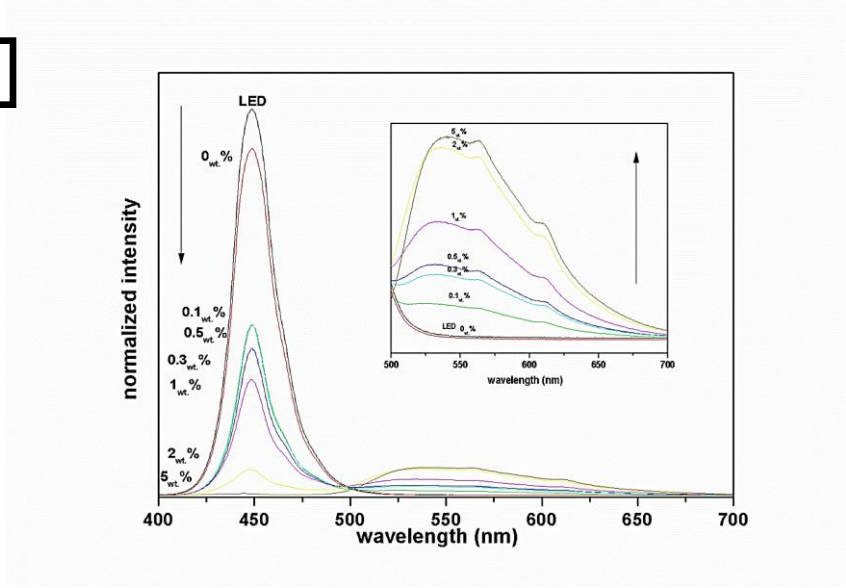

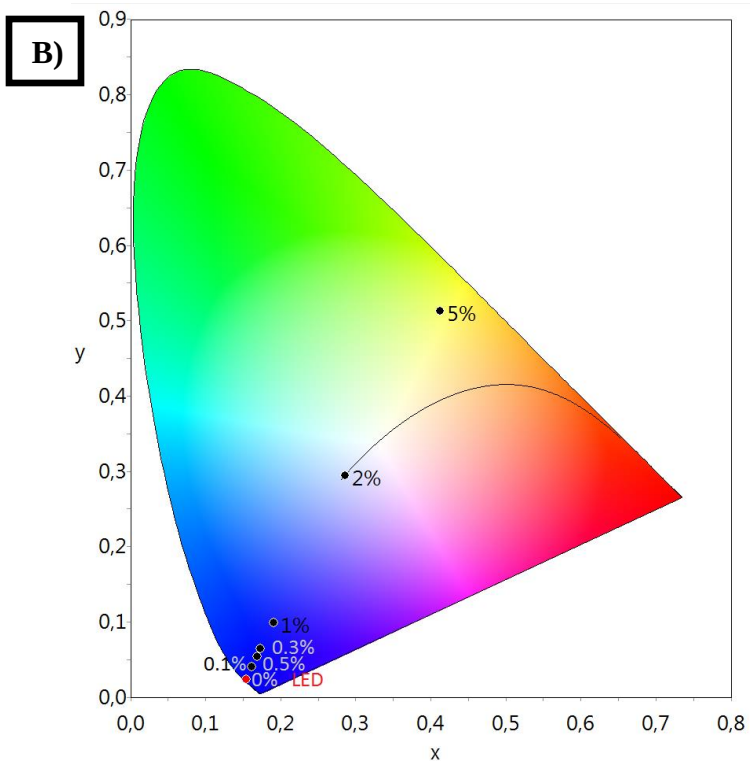

Figure 2.14. (A) Emission spectra and (B) the relative CIE 1931 colour space of the resulting light.

The emission spectrum of the resulting light consists of two bands. The first centered at 450 nm is due to the blue LED, the second one centered at 550 nm is due to the emission of the composite. The intensity of the emission at 450 nm decreases, while the ones at 550 nm increases with increasing amounts of Ce:YAG in the composite. The chromaticity coordinates, calculated from the emission spectra of the resulting lights, are reported in the Commission Internationale de l'Eclairage (CIE) chromaticity diagram (Fig. 8B). The CIE (x, y) coordinates of the lights obtained by combining the blue LED with composites loaded with Ce:YAG up to 1 wt.% are located in the blue region. The CIE coordinates of the lights obtained by combining the blue LED with composites loaded with Ce:YAG at 2 and 5 wt.% are located in the white and yellow regions, respectively. The better light is thus given by the Ce:YAG-PC composite loaded with 2 wt.% Ce:YAG, indicating that it is suitable for a white LED device. This is probably due to the observed red shift, which is enough to

compensate for the absence of red color in the phosphor. However, the emission intensity unfortunately also reduces.

2.3.2. Considerations

A series of Ce:YAG-PC composites were prepared by melt compounding. The effect of the amount of Ce:YAG phosphor on structure, morphology and optical properties of the composites was investigated. Results show that the particles are well dispersed in the polymer and that the polymers is amorphous and that the Ce:YAG maintains unvaried its garnet structure. The specific interactions between the carboxyl oxygen lone pair and the particle surface was identified. The emission of the composite is influenced by the amount of Ce:YAG, in particular a red shift was observed, probably due to the above interface interaction that could cause a different probability in the electronic transitions.

The combination of the composites with a blue LED demonstrated that the light which better balances the blue light and the emissions from Ce:YAG is given by polycarbonate loaded with 2 $_{wt.}$% of Ce:YAG. It, thus, can be used for a white LED device.

This is one of the first systematic study on Ce:YAG-PMMA and Ce:YAG-PC composites, with the aim to find a correlation between the optical properties and the physical and chemical interactions between the two components. In addition, the Ce:YAG-PC composites have been prepared and investigated for the first time. The deepen knowledge of the composites and of their properties creates the basis for the aware industrial production.

References

[1] M.L. Saladino, T.E. Motaung, A.S. Luyt, A. Spinella, G. Nasillo, E. Caponetti, Polymer Degradation and Stability, 97 (2012), 452.

[2] T.E. Motaung, A.S. Luyt, F. Bondioli, M. Messori, M.L. Saladino, A. Spinella, E. Caponetti, Polymer Degradation and Stability, 97 (2012), 1325.

[3] T.E. Motaung, A.S. Luyt, M.L. Saladino, D. F. Chillura Martino, E. Caponetti, Express Polymer Letters, 6 (2012), 871.

[4] V. K. Thakur, D. Vennerberg, S. A. Madboulyb, M. R. Kessler, RSC Adv., 4 (2014), 6677.

[5] E. Shobhana, International Journal of Modern Engineering Research, 2(3) (2012), 1092.

[6] M.L. Saladino, A. Zanotto, D.F. Chillura Martino, A. Spinella, G. Nasillo, E. Caponetti, Langmuir, 26 (2010), 13442.

[7] M.L. Saladino, D.F. Chillura Martino, M.A. Floriano, D. Hreniak, L. Marciniak, W. Stręk, E. Caponetti, The Journal of Physical Chemistry C, 118 (2014), 9107

[8] M.L. Saladino, F. Armetta, M. Sibeko, A. S. Luyt, D. F. Chillura Martino, E. Caponetti, J. of Alloy and Comp. 664 (2016), 726.

[9] S. V. Bhat, A. Govindaraj, A., C. N. R. Rao, Chemical Physics Letters, 422 (2006), 323.

[10] L. Lei Chen, C-C. Lin, C-W., Yeh, R-S. Liu, Materials, 3 (2010), 2172.

[11] T. E. Motaung, M. L. Saladino, A. S. Luyt, D. Chillura Martino, Composites Science and Technology, 73 (2012), 34–39.

[12] T. E. Motaung, A. S. Luyt, M. L. Saladino, E. Caponetti, Polymer Composites., 34 (2013), 164-172.

[13] T. E. Motaung, M. L. Saladino, A. S. Luyt, D.F. Chillura Martino, European Polymer Journal, 49 (2013), 2022–2030.

[14] G. Blasse, A. Bril, The Journal of Chemical Physics, 47 (1967), 5139–5145.

[15] J. Chen, Z. Deng, Z. Liu, Y. Lin, H. Lan, D. Chen, B. Fei, C. Wang, F. Wang, Q. Hu, Y. Cao, Optics Express, 2 (2015), 292-8.

CHAPTER III

Ce:YAG - PMMA nanocomposites

The conversion efficiency of Ce:YAG phosphors based white LEDs is primarily limited by the multiple scattering phenomena of emission from micrometer-sized phosphors [1]. Since the Rayleigh scattering intensity of a particle is proportional to the sixth power of the particle diameter [2], nano-sizing of phosphors is one of the solutions for enhancing the conversion efficiency in phosphor-based LEDs. Another limitation is thermal quenching of luminescence, especially for high power white LED. It may be also enhanced by scattering effect but also by the particles size (limited possibility of dissipation of thermal energy in nanocrystals + many surface defects in nanoparticles). It should be always some compromise between the size, not too small (see above), but also not too large (scattering). However, nanocrystalline phosphors (below ~100 nm in size) in the form of aggregates might be less effective in preventing the scattering loss. From this point of view, the colloidal type of nanophosphors would be expected to be more suitable to extract a better conversion efficiency.

In this chapter, three different methods of preparation of nanophosphors are reported in order to obtain separated particles having a size lower than 50 nm. This particle size could affect the optical properties of the final nanocomposites. Each method has been developed in order to evaluate the effect of the synthesis parameters of the nanoparticle features by investigating their structure and optical properties. The more promising nanophosphor has thus been used for the preparation of the nanocomposites.

§ 3.1. Nanophosphors synthesis

The synthesis of YAG nanophosphors take place by using methods which involve post-synthesis treatments at high temperature necessary to obtain the garnet phase avoiding the formation of secondary phases. Usually, the thermal treatment induces the formation of big agglomerated particles thus leading to a bad efficiency in terms of optical properties. For this reason, the optical properties of nanocrystals are expected to be dependent not only on the doping agent but also on the synthesis route that may influence particle size and its distribution and morphology [3,4,5]. In the last 10 years several chemical routes in solution such as co-precipitation [6,7], sol-gel [8,9], Pechini method [10], solvo-thermal synthesis [11] and others have been used. However, a few papers report a systematic investigation on the role of every parameter to the features of the final product connected to the optical properties. Looking for these aspects of the matter, the research has been focused to develop and to assess some **innovative** and **non-common methodologies** of synthesis able to give a **specific** and **controlled** features of Ce:YAG nanophosphors (particle size <50 nm) with good optical performances. The chosen methodologies are: glycothermal method, microemulsion assisted synthesis and Urea Glass Route. The main advantage of these synthetic routs is the fine control of particles size, although each method has some peculiar characteristics. The glicothermal allows to the formation, at low temperature, of stable YAG nanophosphor dispersions, the microemulsion permits to achieve a defined shape control and the Urea Glass Route is low cost and easy to scale up. Details on each methodology is reported in the following paragraphs.

3.1.1. Glycothermal Synthesis of Ce:YAG nanophosphors

The Glycothermal Synthesis has been chosen because it permits to obtain stable dispersions of garnet nanophosphor in one step avoiding the calcination process. Solvothermal synthesis are based on the conversion of precursors to crystalline nanophosphors in a supercritical fluid. Therefore, in this route the crystallisation occurs whilst the nanophosphors are suspended in a liquid medium avoiding the calcination stage. For example, supercritical fluids have been used to crystallize metal-organic or inorganic precursors into metal oxides. This route also avoids the high temperature heat treatments usually required [12].

Cabanas and co-workers [13] produced single phase YAG in supercritical ethanol and water mixtures using continuous synthesis. The solvent mixtures facilitated the crystallization of the precipitates obtained using ammonia solution at 385°C and 24 MPa. Zhang et al. [14] reduced the processing conditions to 290°C and 10 MPa in a batch type reactor by using a 2:1 ethanol–water mixture, nitrate precursors and ammonium hydrogen carbonate as the precipitant. They obtained monodispersed, spherical particles with a mean size of ~60 nm. Ramanujam at al [15] synthesized YAG nanoparticles of ~30 nm in size with spherical morphology by using 1-4 butanediol, acetate precursors at 300°C and 8.5 MPa for 2. Due to the good results obtained by other authors which use glycols as supercritical fluids a new class of solvothermal synthesis, called glycothermal, has been developed. This methodology was chosen for the synthesis of Ce:YAG nanophosphors on the basis of the good results there reported. The idea is to obtain nanophosphor having high dispersibility in a polymeric matrix (i.e. by adding a functionalizing agent [16]) for the preparation of optima nanocomposites.

3.1.1.1 Effect of reactants concentration

The study started with the set-up of the proper conditions for the preparation of pure Ce:YAG nanophosphors.

The organic precursors used were yttrium acetate hydrate ($Y(CH_3CO_2)_3 \cdot xH_2O$), aluminum isopropoxide ($Al(OCH(CH_3)_2)_3$) and cerium acetate hydrate

($Ce(CH_3CO_2)_3 \cdot xH_2O$). These provided the source of Y^{3+}, Al^{3+} and Ce^{3+} ions, respectively. 1,4-butanediol was used as the solvent medium. A conventional autoclave reactor from FKV s.r.l. equipped with Parr 4838 Reactor Controller, was used for the synthesis. The controller is managed by PID (Proportional-Integral-Derivate) able to program with Auto-tuning capability for precise temperature control and minimum overshoot. A scheme of the complete apparatus is reported in Figure 3.1.

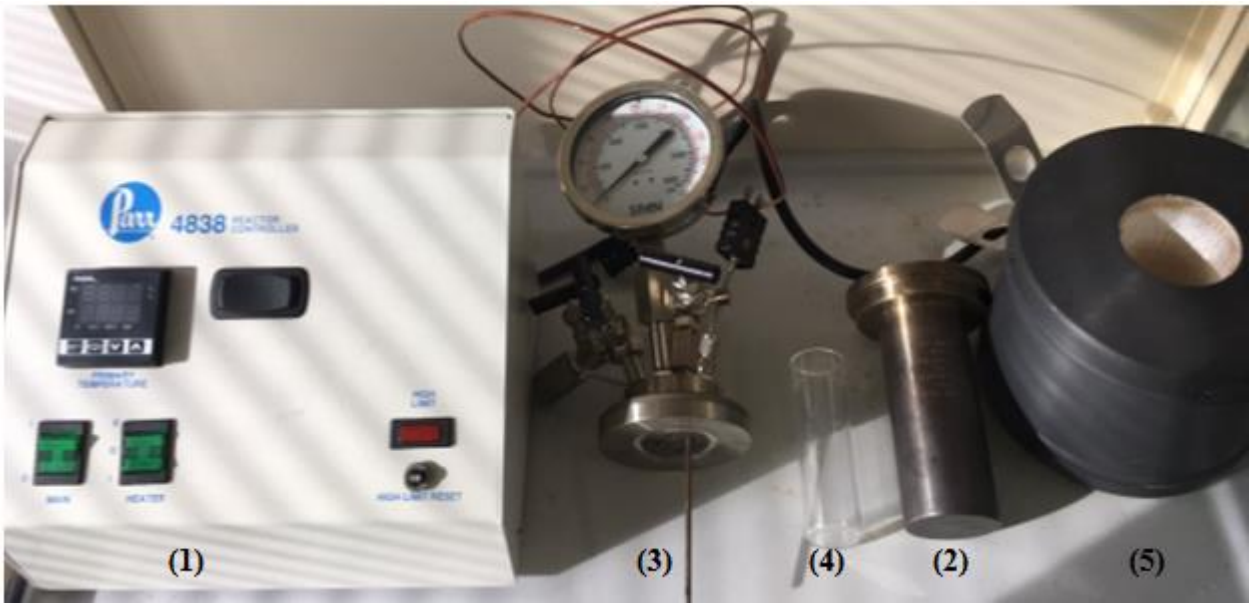

Figure 3.1. Photo of the complete apparatus. *(1)* temperature controller, *(2)* reactor, *(3)* head of reactor, *(4)* liner, *(5)* heater.

The yttrium, aluminum and cerium solutions were prepared by dissolving proper amounts of reactants in 1,4-butanediol in order to respect the formula $Ce_{0.06}Y_{2.94}Al_5O_{12}$. The heating ramp was executed as follows: from 25 to 150 °C in 15 minutes, then to 200 °C in 30 minutes, to 270 °C in 10 minutes and to 300 °C in 10 minutes. Each batch was thus maintained at 300°C for 2h. Several syntheses were performed by increasing reactants concentration in order to evaluate the effect of this parameter on the YAG formation. It is important both for crystalline phase formation and nanoparticles growth. Obviously, at low concentration the nuclei formation has a low possibility to growth. The used values are reported in Table 3.1.

Table 3.1. Reactants concentration used for each synthesis and maximum reached pressure as well.

Sample	Concentration (mol L^{-1})			P_{max} (bar)
	aluminum isopropoxide	yttrium acetate	cerium acetate	
1	0.025	0.014	0.0006	35
2	0.030	0.017	0.0006	43
3	0.058	0.035	0.0010	46
4	0.118	0.069	0.0021	54
5	0.178	0.104	0.0032	60
6	0.206	0.120	0.0038	70
7	0.234	0.138	0.0042	78

The maximum reached pressure as function of aluminum isopropoxide concentration is reported in Figure 3.2.

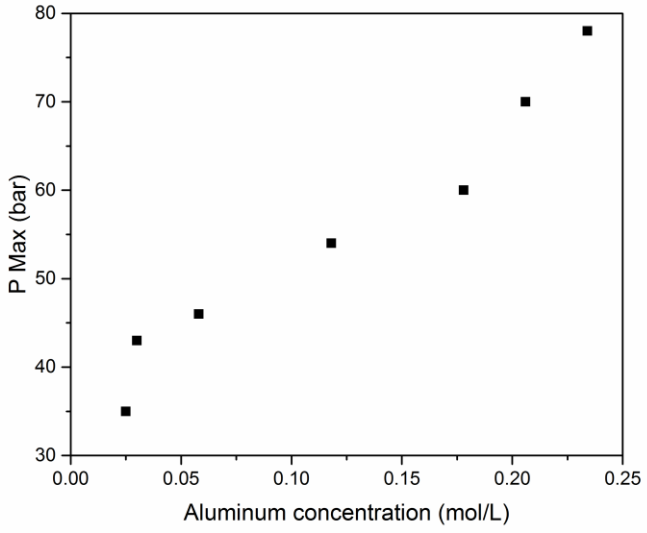

Figure 3.2. Maximum reached pressure for each batch of synthesis.

The pressure increase is ascribable by taking into account the transformation of 1,4-butanediol during the reaction. It has been reported that it transforms into tetrahydrofuran when the isopropoxide group is present. Tetrahydrofuran has a low boiling point (66°C), therefore, its formation and consequent evaporation can cause an increase of the autogenous pressure. Particularly, the pressure reaches a higher value on increasing the aluminum isopropoxide concentration.

After 2 hours in autoclave, the treatment was stopped. The obtained dispersion has a yellowish coloration (see Figure 3.3).

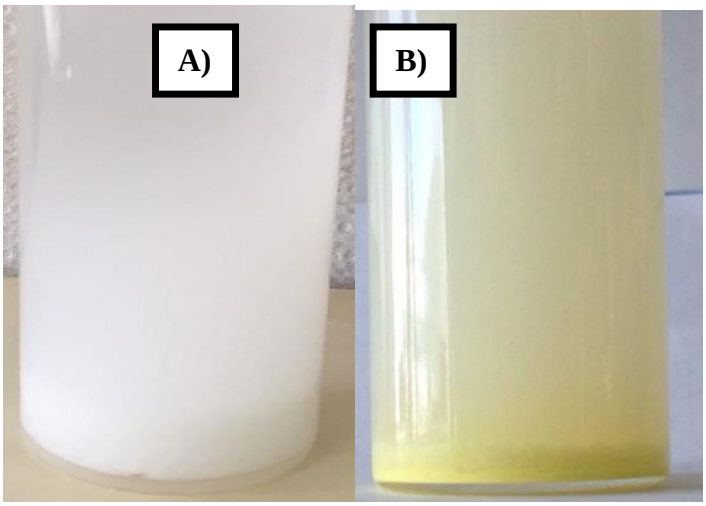

Figure 3.3. System 7 before (A) and after (B) the treatment in autoclave.

The resultant dispersion was centrifuged at 3500 rpm, washed three times using ethanol to remove the precursor residues, and then dried at 60◦C for 24 h before being ground using an agate pestle.

WAXS. In order to gain information about the crystalline phase of the obtained powders Wide Angle X-ray Scattering (WAXS) techniques was used.

The diffraction patterns of the obtained samples are reported in Figure 3.4.

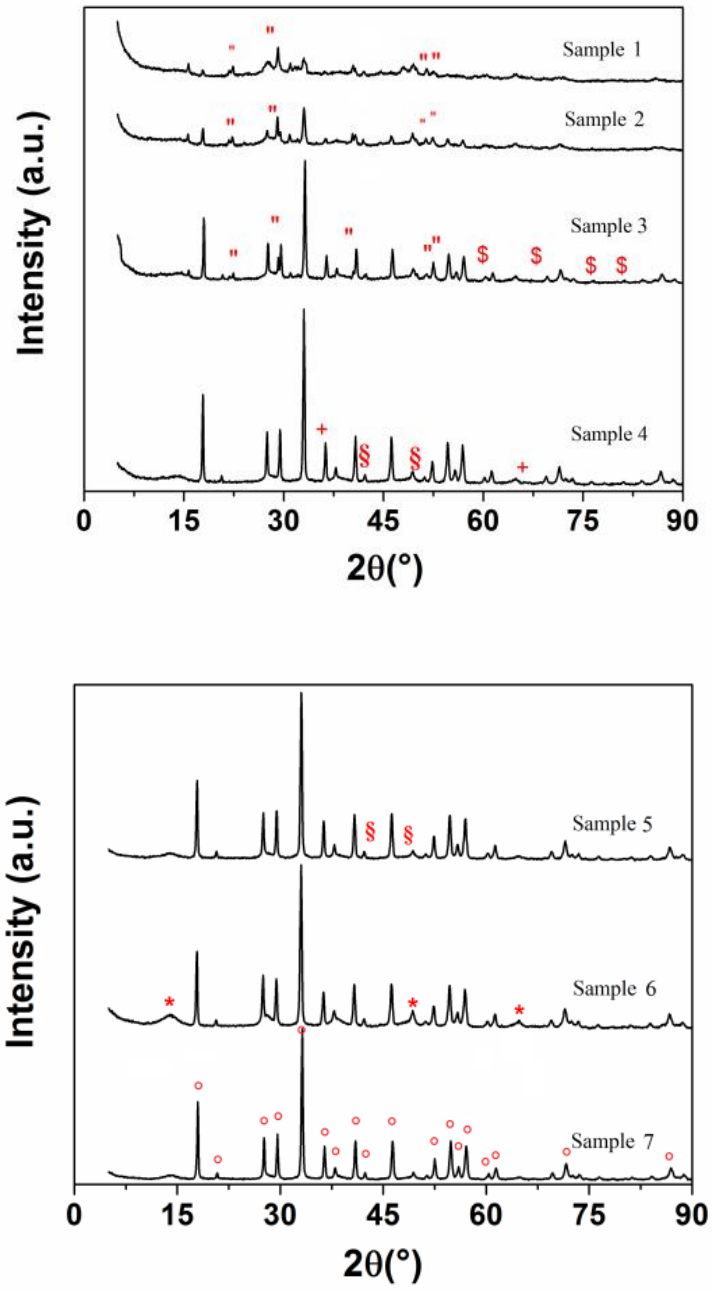

Figure 3.4. WAXS Patterns of samples obtained for the different batch. ° $Y_3Al_5O_{12}$ YAG; * γ-AlO(OH) boehmite ; + $Y_4Al_2O_9$ orthorhombic; § $Y_3Al_5O_{12}$ tetragonal; " YOOH monocline ; $ $Y(OH)_3$ hexagonal.

All patterns contain YAG peaks, together with other peaks due to secondary phases. In detail, samples 7, 6, 5 and 4 display several sharp peaks of boehmite, an aluminum oxide hydroxide (γ-AlO(OH)) as previously shown by Nyman et al. (layered alumina phase)[1] and Revaux at al. [17]. Samples 3, 2 and 1 display several phases and a strong decrease of the Intensity of the YAG peaks. Probably, the low pressures reached in these batch were insufficient to allow the reactants evolution to garnet phase. The identified phase for each pattern are resumed in table 3.2.

Table 3.2. Phases determination, obtained by the software X'Pert HighScore Plus of the WAXS patterns. Score reflects the quality of the intensity match.

Sample	Crystalline phases	Score
1	$Y_3Al_5O_{12}$, YAG, garnet	32
	$Y_3Al_5O_{12}$, YAG, tetragonal	21
	YOOH, monocline	60
	$Y(OH)_3$, hexagonal	32
2	$Y_3Al_5O_{12}$, YAG, garnet	52
	$Y_3Al_5O_{12}$, YAG, tetragonal	18
	YOOH, monocline	61
	$Y(OH)_3$, esagonal	19
3	$Y_3Al_5O_{12}$, YAG, garnet	56
	YOOH, monocline	54
	$Y_3Al_5O_{12}$, YAG, tetragonal	15
	$Y(OH)_3$, hexagonal	18
4	$Y_3Al_5O_{12}$, YAG, garnet	57
	$Y_3Al_5O_{12}$, YAG, tetragonal	19
	$Y_4Al_2O_9$, orthorhombic	16
5	$Y_3Al_5O_{12}$, YAG, garnet	56
	$Y_3Al_5O_{12}$, YAG, tetragonal	18
6	$Y_3Al_5O_{12}$, YAG, garnet	78
	γ-AlO(OH), boehmite orthorhombic	30
7	$Y_3Al_5O_{12}$, YAG, garnet	78
	γ-AlO(OH), boehmite orthorhombic	25

TEM investigation was performed in order to investigate the morphology and to evaluate the particle size of the powders obtained in batch 6 and 7, where the garnet phase is present in higher quantity. This information is required to know the morphology of the YAG particles obtained by using this method of preparation.

Some TEM micrographs at different magnifications of the samples 6 and 7 are reported in Figure 3.5. In the same figure, the SAED patterns and EDS spectra acquired on the observed objects are reported.

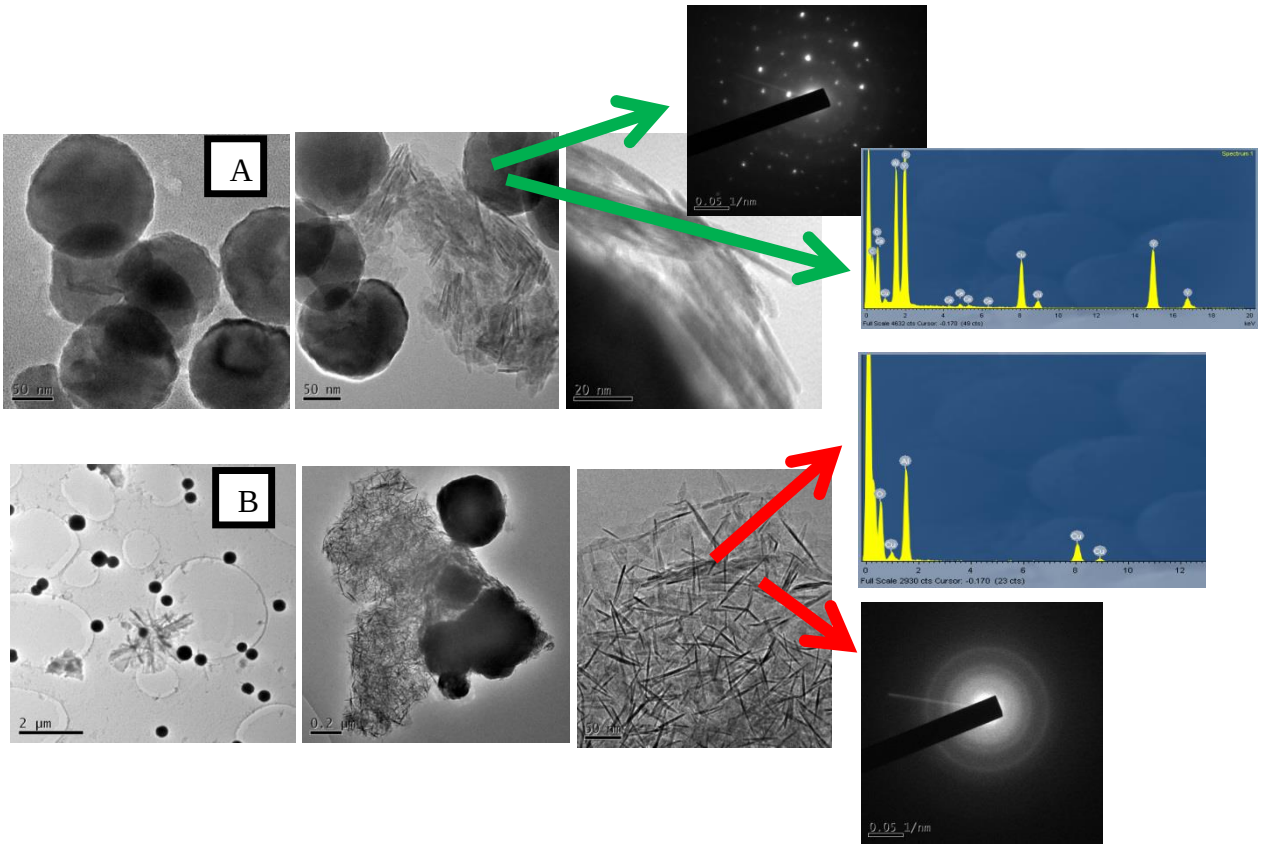

Figure 3.5. TEM micrographs, EDS spectra and SAED patterns of sample 7 (a) and 6 (b).

The samples are constituted by crystalline, not-aggregated spherical nanoparticles, whose average size is about 70 and 110 nm in sample 6 and 7, respectively. The EDS analysis confirms the presence of aluminum, yttrium and oxygen, indicating that they are YAG particles. In the case of sample 7 the particles seem to be more agglomerated than in the sample 6.

Long needles are also present in same samples. EDS reveals that they are mainly composed by aluminum and oxygen. It is possible to suppose that they are

constituted by the secondary phase, boehmite. This particles shape and SAED pattern justify the sharpness of the boehmite WAXS profile.

Results show that the glicothermal method in autoclave led to control of the particle morphology and the agglomeration occurring in the final powder and in the dispersion. The experimental conditions (temperature, pressure and reactant concentrations) influence the formation of the garnet phase as well as the nanoparticle features. Unfortunately, at the investigated experimental conditions, the pure YAG phase has not been obtained. By using the glicothermal synthesis, different results could be obtained as function of the reactor characteristic, as Nyman et al [1]. They have performed the synthesis in same conditions obtain particles with different dimension, reaching also different values of autogenic pressure. Probably, in this case an increase of concentration could permit to reach a proper value of pressure. However, since a concentration increase lead to an increase in particles size, looking for the goal of my research, the increase of this parameter is not reasonable. In addition, considering the maximum volume of solution used in the batch 7, by using this reactor, a higher pressure cannot to be obtain.

3.1.2. Synthesis of YAG and Ce:YAG nanophosphors by microemulsion assisted synthesis

It is well know that, the synthesis in microemulsion (a confined environment) gave optimal results, in terms of short heating time, small particle size and narrow particle size distribution [18]. The ability of surfactants to self-assemble into well-defined structures has constituted one of the main advantages for the design and synthesis of particles with nanosized dimensions. The microstructures formed by self-assembly of the surfactant have been used as nanoreactors or templates for the synthesis of nano- and meso-porous materials [19,20,21]. The accuracy and reproducibility of the self-assembly microstructures process have been seen as a way of achieving control of materials architecture at the nanometer scale. As a consequence, the number of papers dealing with surfactant-templated synthesis of inorganic materials has dramatically increased in the last 20 years [22,23,24]. Furman et al. obtained Ce:YAG nanoparticles having specific optical properties by an emulsion

route [25]. Jun at al. successfully prepared Nd:YAG nanoparticles with weak agglomeration and diameters of 40 and 80 nm using a novel approach called co-microemulsion–microwave heating [11]. Caponetti et al. prepared Nd:YAG nanopowders, constituted by small crystalline nanoparticles showing a low tendency to agglomerate, in a water/CTAB/1-butanol/n-heptane microemulsion [26]. The last system was chosen for the synthesis of Ce:YAG nanopowders.

3.1.2.1 Microemulsion Characterization

The possibility to characterize and control the structure of a microemulsion used in nanofabrication is of the uttermost importance in order to obtain a final product with the desired properties. Therefore, the microstructure of quaternary microemulsion, chosen to perform the synthesis, has been investigated as function of a component content. The results are presented in this paragraph.

Considering a quaternary microemulsion its composition could be described by three parameters, P, R, S defined as:

$$P = \frac{mol_{1-butanol}}{mol_{CTAB}}; \qquad R = \frac{mol_{water}}{mol_{CTAB}}; \qquad S = \frac{mol_{n-heptane}}{mol_{CTAB}} \tag{1}$$

The microemulsions were obtained by weighting the appropriate amount of n-heptane (the continuous oil phase), aqueous solution (the dispersed phase), CTAB (the surfactant) and 1-butanol (the cosurfactant). P and S were fixed at 4.1 and 13.3, respectively as reported in the literature [26]. R varied from 4.3 to 70.0 (respectively the minimum and the maximum solution amount that grants for a homogeneous system, respectively).

The yttrium, and aluminum nitrate solution (30, and 50 mmol L^{-1}, respectively) was prepared by dissolving $Y(NO_3)_3 \cdot 6H2O$ and $Al(NO_3)_3 \cdot 6H_2O$ in water. The microemulsions containing the aqueous solution of nitrates were prepared by using appropriate amounts of the 80 mmol L^{-1} aluminum and yttrium salts above solution at a 5:3 ratio. The microemulsions containing the ammonia solutions were prepared by fixing the ammonia concentration to 50 mmol L^{-1}. The latter condition was chosen

in order to get the proper pH (~ 10) to precipitate yttrium and aluminum hydroxides when equal amounts of the microemulsions containing nitrates and ammonia are mixed.

It is well known [27] that the differences in the structural organization of a fluid may lead to differences in its rheological properties. Therefore, a viscosimetric and conductometric study was performed on the two microemulsions containing the aqueous solutions of ammonia and aluminum and yttrium nitrates, respectively. The plots of the relative viscosity, η_r, and the logarithm of conductivity, σ, as a function of R-values for all compositions investigated are reported in Figure 3.6a and 3.6b.

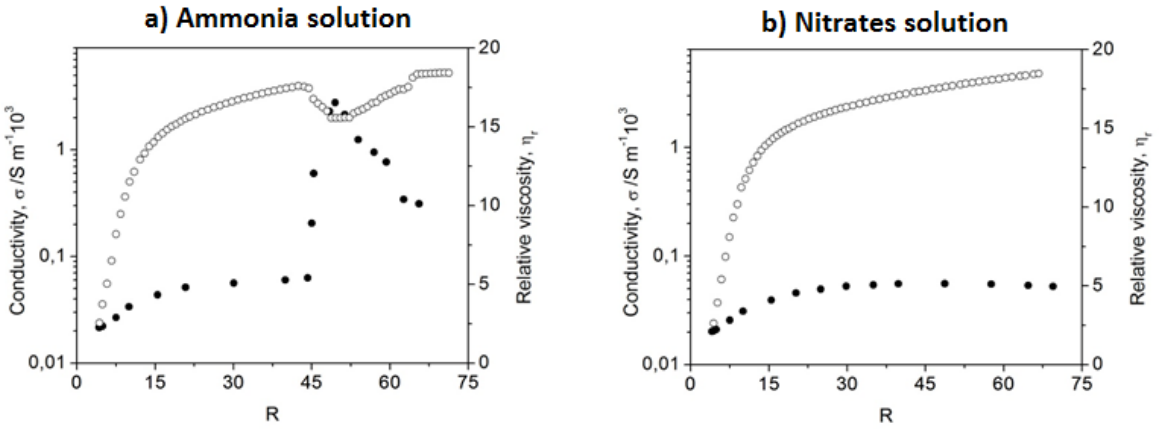

Figure 3.6. Electrical conductivity (open) and viscosity (close) for microemulsion containing: a) Ammonia solution and b) nitrates solution.

The trends reveal a variation of both viscosity and conductivity values on increasing the solutions content. Discontinuities and slope change appear for both properties around the same R-values indicating the occurrence of different phases. In particular, data (Figure 3.6a) obtained for the microemulsion containing ammonia solution suggest that a first phase exist for low R (lesser than approximately 8), a second one is present at 8 < R < 45, a third phase at 45 < R < 60 and finally a new phase appear at R > 60. Up to R = 45 the viscosity increases thus suggesting the presence of big aggregates or eventually the formation of entangled structures. The sudden increase

of viscosity at R = 45 indicates the occurrence of a new structure that became more fluidic by increasing the water content.

The trend observed for microemulsion containing nitrates solution (Figure 3.6b) suggests that a first phase exist for R < 10 while a second one is present at 10 < R < 70. The conductometric results confirm the presence of different phases at the same R value range as that determined by viscosimetry, furthermore allow deepen insight about their nature. As it can be seen in Figure 3.6, the plot of the logarithm of conductivity as a function of R presents a noticeable change of slope and this behavior can be reasonably ascribed to the presence of a percolation threshold as proposed by Moulik *et al*. [28]. In the dynamical percolation model, surfactant molecules act as charge carriers between water clusters dispersed in the oil phase and the charge transfer under the influence of an electric field occurs only when the distance between two clusters is small enough. On increasing the water content, the clusters size increases and consequently the average distance between them decreases in agreement to an overall increase in the conductivity of the microemulsion. Such increase continues till the distance between the clusters becomes so small that they connect and form a bicontinuous phase where charge transfer occurs directly via the movements of the charge carriers inside the aqueous phase. The value of the volume fraction corresponding at the formation of bicontinuous phase is named percolation threshold.

Evidences of a two-stage process are known in many fields [29,30] and recently a model for this process has been proposed [31], the percolation processes in microemulsion phase evolution have been studied by Borkovec et al. [32].

However, the two-stage process were observed by independently varying the water volume fraction or the oil volume fraction. In that case, the evolution from the w/o microemulsion to a bicontinuous one as well as the evolution from the o/w microemulsion to a bicontinuous one were observed without a macroscopic phase variation.

It is possible to correlate the conductivity before and after the percolation threshold to the volume fraction of the aqueous phase, ϕ [33]:

$$\sigma_1 = k(\phi_t - \phi)^{-s} \qquad \sigma_2 = k(\phi - \phi_t)^{\mu} \tag{2}$$

where σ_1 and σ_2 are the conductivity before and after the percolation threshold respectively, ϕ_t is the volume fraction at the threshold, *k* is a constant correlated to the conductivity of the dispersed phase (the aqueous phase, in this case), *s* and μ are constants typical of the system under investigation. The model doesn't cover the points near the percolation threshold.

The volume fraction of the dispersed phase was estimated via the following equation [33]:

$$\phi = 1 - (1 - w_0)\frac{\rho}{\rho_0} \tag{3}$$

where w_0 is the weight fraction of the dispersed phase and ρ and ρ_0 are the densities of the microemulsion and the dispersing medium (*e.g.* n-heptane), respectively.

Conductivity trend is the typical second section of a sigmoid percolation graph (just above the percolation threshold). Unfortunately, the system is biphasic at lower water content. The result of a nonlinear fitting of equation 4 to the experimental data is reported in Figure 3.7a and 3.7b.

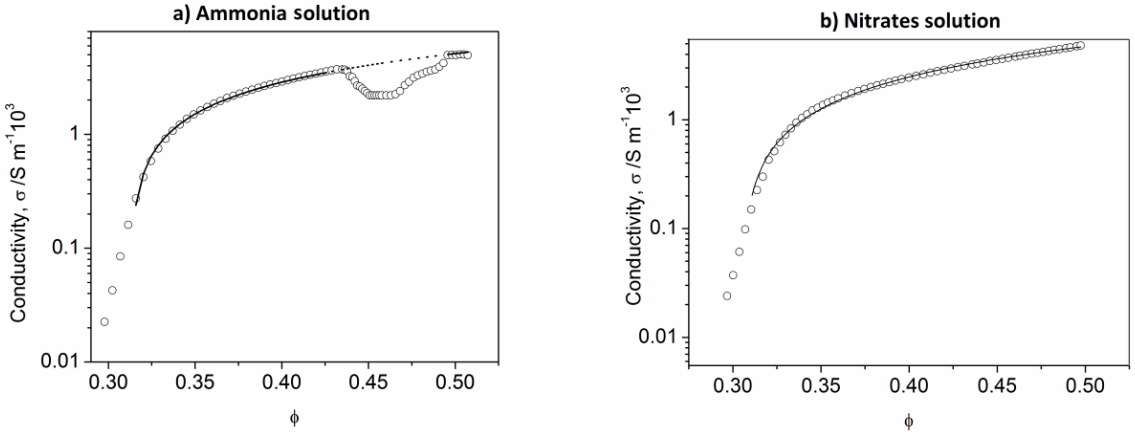

Figure 3.7. Electrical conductivity on increasing volume fraction of dispersed phase: a) ammonia solution and b) nitrates solution. Circles, experimental values; line, fit obtained with the percolation model described in the text.

The computed curve reproduces the observed data very satisfactorily corroborating the hypothesis of the presence of a percolation threshold for φ = 0.31 (corresponding

to R ≈ 7.5) that separates a water in oil microemulsion from a bicontinuous phase. It is worth noticing that the percolation threshold position remains unchanged for each microemulsion (R ≈ 7.5). The microemulsion σ values are consistent with this interpretation. In fact, conductivity increases from values around 10^{-4} S m^{-1}, typical of water in oil microemulsions, to 10^{-3} S m^{-1}, comparable with the conductivity of a conventional electrolyte solution as expected for a bicontinuous system. For the microemulsion containing ammonia solution, in correspondence of volume fraction higher that 0.43 there is a misfit. However, conductivity values computed by means of the same model for volume fraction higher that 0.48 are in fair good agreement with the experimental ones. In our opinion, this strengthens the goodness of the applied model. Moreover, the misfit in the range 0.43 – 0.48 is a direct consequence of the different structure of the system in this compositional range.

SAXS. In order to gain a detailed knowledge about the nature of the phases evidenced by these systems, Small Angle X-ray Scattering (SAXS) technique was used to investigate their structural organization in the same R range. The scattering intensities *vs.* Q obtained for the aqueous solutions/CTAB/1-butanol/*n*-heptane systems, at different compositions, are reported in Figure 3.8a and 3.8b.

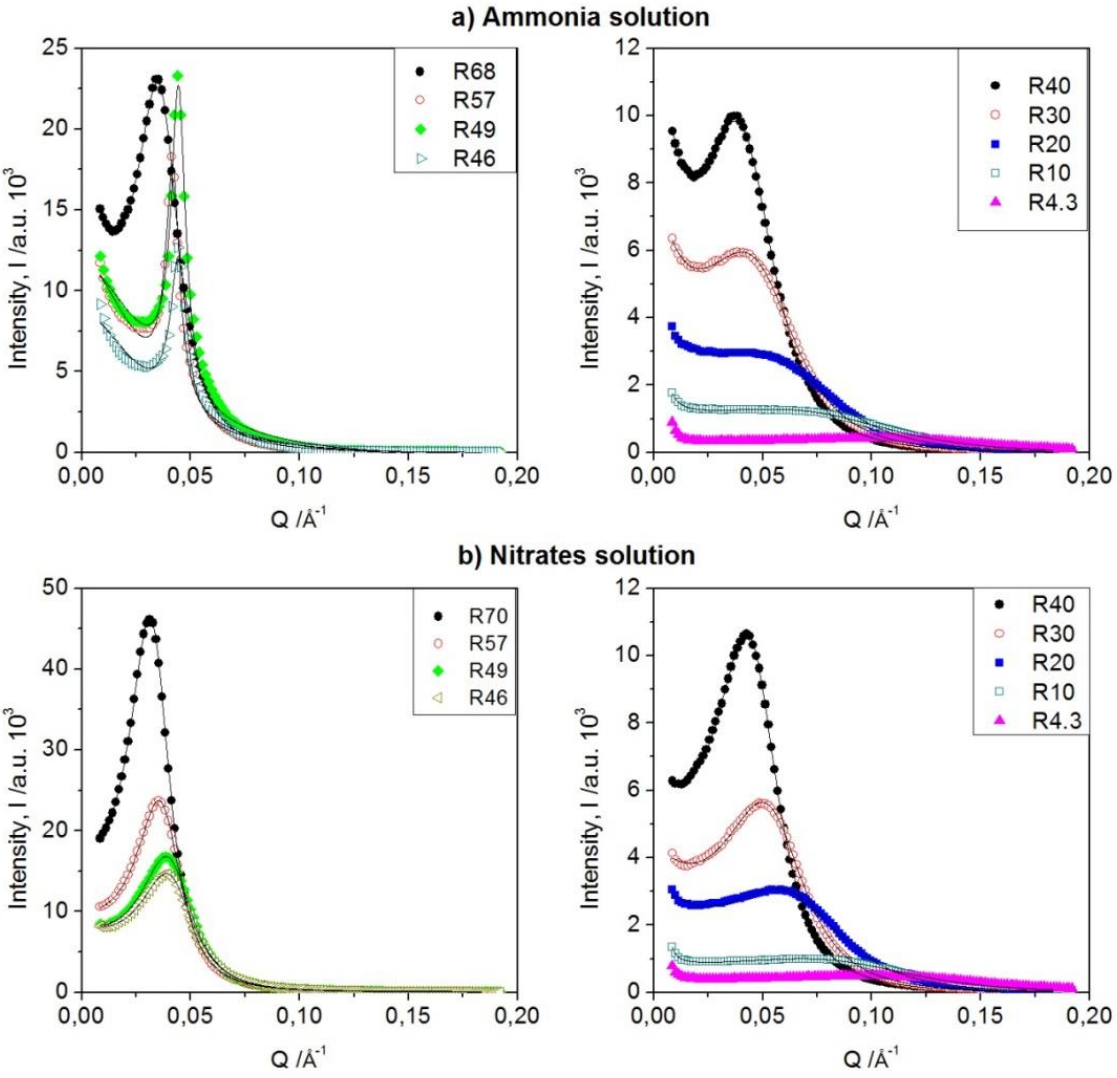

Figure 3.8. SAXS of solution/CTAB/1-butanol/*n*-heptane microemulsion with different water solution content: a) ammonia solution and b) nitrate solution. Symbols, experimental data; lines, fit obtained with decoupling approach for R = 4.3 and Teubner-Strey approach for other R-values.

The scattering patterns in Figure 3.8a present a peak that evolves in position and intensity on increasing R. The peak position moves toward lower Q values and the peak shape becomes narrower on increasing R up to R = 40. The peak position depends on the size and on the volume fraction of the dispersed phase. A displacement toward lower Q-values indicates that the size effect overcomes the volume fraction one. The observed data in the range 4.3 < R < 40 and at R = 70

suggest the presence of microaggregates or bicontinuous structures, as the two structures give similar patterns [34,35]. At 40 < R < 70 the peak becomes a cusp. The cusp peaks are typical of lamellar phase [36]. Moreover, the patterns present an intensity contribution for low Q values that is ascribable to critical scattering due to fluctuations of surfactants concentrations.

The scattering patterns in Figure 3.8b are different from the previous ones, as the peak intensity, shape and position evolves without the appearance a cusp, thus confirming a regular evolution in the structure without a phase transition.

At lower water content the system could be described by using a model consisting of micellar aggregates dispersed in a continuous medium (the oil phase) and the presence of a critical scattering at low Q values was taken into account as a contribution in the Ornstein and Zerniche [37] form.

For incompressible fluids the total scattering function is given by the linear combination of the scattering functions describing the two contributions [38]:

$$I(Q) = < F^2(Q,r) > + < F(Q,r) >^2 \ [S(Q) - 1] + \frac{I_0}{1 + \xi_0^2 Q^2} \qquad (4)$$

where F(Q,r) is the form factor, S(Q) is the structure factor, I_0 is a scaling factor and ξ_0 is the correlation length of the concentration fluctuations. The hard sphere potential has been used to model the structure factor. The fitting procedure was carried on using SASfit software [39].

As a first attempt, the form factor of spherical objects was considered. The fitting procedure hasn't been successful by using this form factor. By considering ellipsoidal objects, the fitting procedure reproduces satisfactorily the experimental data of nitrates microemulsion for R = 4.3, 10, 20, and 30 while the curve for R = 40 weren't reproduced. The parameters evaluated with this model are summarized in Table A1 of Appendix 3. A typical example for the fitted curve is shown in Figure 3.9a for the sample R = 30.

It is worth to emphasize that although the fitting procedure gave satisfactorily results for all the R ≤ 30, perusal of the obtained geometric parameters suggests that this description could not be adequate for R ≥ 4.3.

It is well known that a thermodynamic description of the global phase behavior of multicomponent mixtures provides an explanation of the gross feature of the microemulsion phase behavior. Thus, for the microemulsions with R ≥ 4.3, the model based on the phenomenological approach proposed by Teubner and Strey [38] was considered. In this approach the phenomenological Landau free energy is obtained from an order parameter expansion. This approach has already been successful used for the analysis of SAXS data of some microemulsions [40,41].

Data modeling by means of the phenomenological approach proposed by Teubner and Strey. This approach correlates the scattering intensity to the vector Q by the following equation:

$$I(Q) = \frac{8\pi c_2 \left\langle \varepsilon^2 \right\rangle / \xi}{a_2 + c_1 Q^2 + c_2 Q^4} + E \qquad (5)$$

Where $\langle\varepsilon^2\rangle = \phi_w(1-\phi_o)$ being ϕ_w the volume fraction of the aqueous medium, ϕ_o the volume fraction of the oil medium, $\langle\varepsilon^2\rangle$ is the mean of the squares of the difference in scattering length densities between the aqueous and the oil media, Q is the scattering vector previously defined and ξ is the correlation length. a_2, c_1 and c_2 are the coefficients appearing in the phenomenological Landau free energy expression obtained from an order parameter expansion of the free energy density; they are related to the stability of the system. For a peak to appear at nonzero wave vector in the scattering spectrum c_1 must be negative.

Alternative once a_2, c_1 and c_2 are known it is possible to calculate ξ, the correlation distance and d, that is a measure of the quasiperiodic repeat distance between polar and nonpolar environments [42] as in a lamellar phase.

$$\xi = \left[\frac{1}{2} \left(\frac{a_2}{c_2} \right)^{1/2} + \frac{c_1}{4c_2} \right]^{-1/2} \tag{6}$$

$$d = 2\pi \left[\frac{1}{2} \left(\frac{a_2}{c_2} \right)^{1/2} - \frac{c_1}{4c_2} \right]^{-1/2} \tag{7}$$

An amphiphilicity factor f_a that is indicative of the system stability and provides information about the degree of its structural organization was defined by Shubert [42].

$$f_a = \frac{c_1}{\sqrt{4\, c_2 a_2}} \tag{8}$$

For f_a value close to -1 the lamellar liquid crystal is the dominating phase in the phase diagram, a slight f_a decrease leads to an isotropic phase which is strongly structured as a bicontinuous microemulsion, a further decrease indicates a switch from a non-wetting to wetting phase.

The used equation for data fitting procedure is a linear combination of the Teubner-Strey (eq. 5) and the Orstein-Zernike (eq. 4) contribution.

In order to reduce the number of variables and to improve the fitting procedure, the following modified equation was obtained from eq. 6 and eq. 8, by a simple mathematical treatment:

$$I(Q) = \frac{I_{OZ}}{D + Q^2} + \frac{8\pi \langle \varepsilon^2 \rangle \sqrt{0.5\sqrt{A} - L/4}}{A + LQ^2 + Q^4} + E \tag{9}$$

where $I_{OZ} = I_0/\xi_0^2$, $D = 1/\xi_0^2$, $A = a_2/c_2$ and $L = c_1/c_2$. This allows reducing the number of fitting parameters from 6 to 4.

The obtained curves reproduce satisfactorily the observed data for all the R-values, as shown in Figure 3.9. A typical example of the two different contributions to the fitted curve is shown in Figure 3.9b for the composition R = 30.

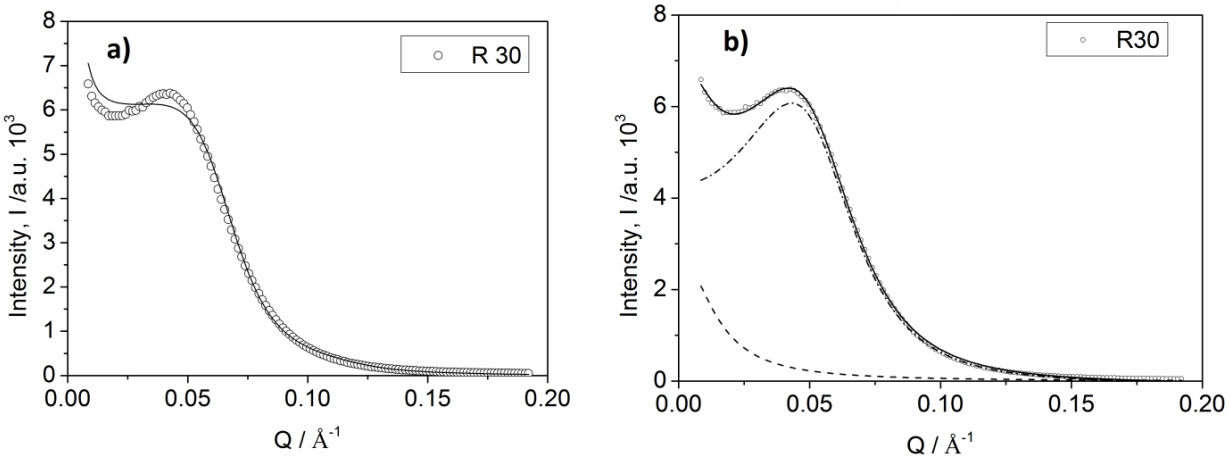

Figure 3.9. Fit (full line) of SAXS data (circle) of nitrate solution/CTAB/1-butanol/*n*-heptane microemulsion R30. a) decoupling approach b) phenomenological approach, the dash and the dash dot curves represent the contribute of Ornstein-Zernike and Teubner-Strey respectively.

Table A2 in Appendix 3, reports the results of the fitting procedure (eq. 9) to the experimental data obtained for R > 4.3.

The trends of the correlation distance, ξ, the quasiperiodic repeat distance, d and amphiphilicity factor, f_a on increasing the water content in the systems are reported in Figure 3.10.

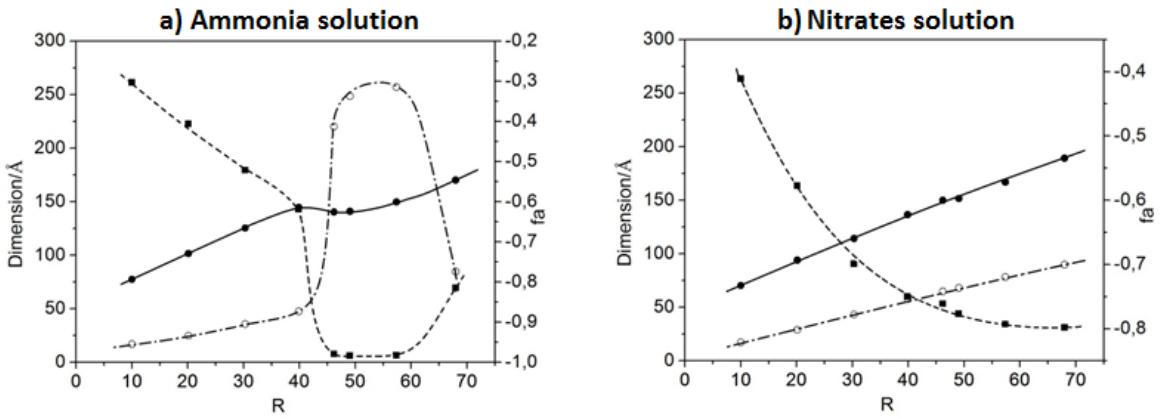

Figure 3.10. Teubner-Strey parameters vs R. Circles for the structural dimension d (close) and ξ (open), square for amphiphilicity factor f_a. The lines are plotted as trends guide. a) ammonia solution and b) nitrates solution.

The trends of ξ, d and f_a for the nitrates solution systems are regular. The amphiphilicity factor, f_a, decreases from -0.4 at R = 10 to -0.8 at R = 70 indicating an increase in the order of the system. These values are typically of a bicontinuous structure. It is worth to emphasize that there is a perfect overlap of these information with conductometric and viscosimetric data. ξ and d increase linearly on increasing the solution content.

The trends for the parameters obtained in presence of ammonia are rather different from the nitrates ones. It can be noted that the three parameters describing the structural organization show discontinuities around R = 46 and R = 60 indicating the presence of different phases. The amphiphilicity factor, f_a, decreases from -0.30 at R = 10 to -0.97 at R = 49, indicating an increase in the order of the system. At R = 70 it increases to -0.82. These values are typical of bicontinuous structure up to R = 40 and for R = 70 and typical of a lamellar structure for 40 < R < 70. A comparison with conductometric and viscosimetric results in Figure 3.6 clearly highlights that the discontinuities in all the trends are manifested at the same R-values. It is thus possible to ascribe the observed trends in conductometric and viscosimetric investigations to a transition from a bicontinuous to a lamellar phase. ξ and d increase linearly on increasing solution content up to R = 40 and exhibit the same trend observed for the amphiphilicity factor. For 40 < R < 70 the d variation is ascribable to its different meaning, in fact it is the quasiperiodic cylinders' distance of a wormlike structure as a

bicontinuous one ($R \leq 40$) that evolves to lamellae distance in lamellar structure ($40 < R < 70$) the value at $R = 70$ is in line with bicontinuous distances. The ξ strong variation could be ascribable to the different domain distribution.

Also in this case the information obtained from SAXS pattern analysis are consistent with viscosimetric and conductometric results. The first phase transition from water in oil microemulsion ($R = 4.3$) to a bicontinuous one ($R = 10$) is in agreement with the percolation threshold for which above $R \approx 7.5$ charge carriers can freely move in the water phase without any interruption as a consequence of the formation of a continuous phase. The lamellar phase observed at higher water content explains the viscosity behavior as reported in the literature [43]. The last return to low viscosity is coherent with the transition to the bicontinuous phase.

The effect of the solute addition to the system strongly depends on its nature. The different effect observed in the case of the two solutes may be explained taking into account the difference in the resulting ionic strength. In fact, it is well known [44] that the presence of charged species may significantly affect the phase behavior of self-aggregated systems such as a microemulsion, especially in the case of ionic surfactants such as CTAB. Specifically, the presence of dissolved salt screens the electrostatic repulsion between the charged head group, increasing the negative curvature of the surfactant. As a consequence, the high ionic strength causes an increasing of interface curvature favoring the bicontinuous structure formation in the nitrates solution thus preventing the lamellar structure formation. On the other hand, the behavior observed for ammonia solutions can be ascribed to the strength of the hydrogen bond among ammonium ions and water molecules [45]. In fact, it has been recently reported [44] on the basis of a theoretical approach that the main features of the hydrogen bond between NH-O are close to those of the OH-O bond in the isolated water dimer.

The phase behavior of nitrate microemulsion at the investigate compositions is summarized in the pseudo-ternary diagram in Figure 3.11 where the various domains are highlighted.

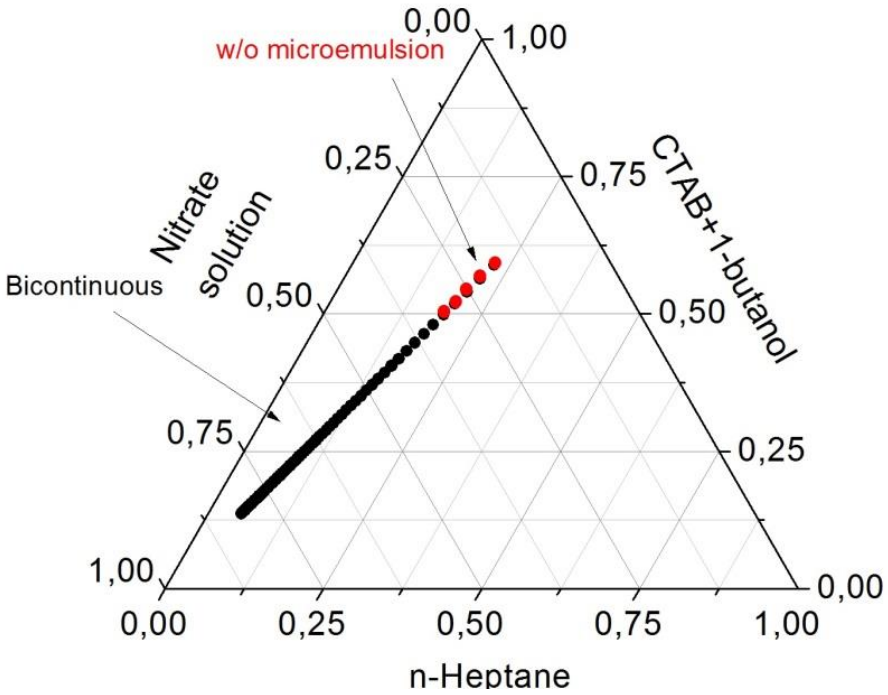

Figure 3.11. Pseudoternary diagram of the nitrate solution/CTAB/1-butanol/*n*-heptane microemulsion. Circles indicate the composition studied, ellipsoidal areas indicate the different phases observed.

3.1.2.2 Effect of microemulsion structure

Evaluated the different structure as function of the water solutions content, it was possible to decided which R value could be most promising for the synthesis. The precursor synthesis of YAG nanopowders was performed by mixing two microemulsions containing reactants at the same R, 20 and 70, respectively. These two microemulsions have the same structural organization with different domains size and order degree, so there are only two structural parameters which can affects the synthesis.

The microemulsion containing ammonia solution was added dropwise to the microemulsion containing nitrate solution maintained under constant stirring at room temperature. A white hue sol was instantaneously observed, indicating the formation of hydroxides. A complete precipitation occurred in 12 h. The precipitate

was filtered and repeatedly washed with water to remove residual ammonia, nitrate ions, and surfactant molecules. The presence of ammonia and nitrate ions were checked by means of concentrated hydrochloric acid and by using the brown ring test, respectively. The obtained white precipitate, labelled as R20Nps and R70Nps, was oven dried at 100 °C for a night and then calcined at 900 °C for 1 h. The production yield of the Ce:YAG powder reach (at the maximum) 40% in weight.

WAXS. In order to gain information about the crystalline phase of the obtained white precipitates WAXS technique was used. The diffraction patterns of the R20Nps and R70Nps samples are reported in Figure 3.12.

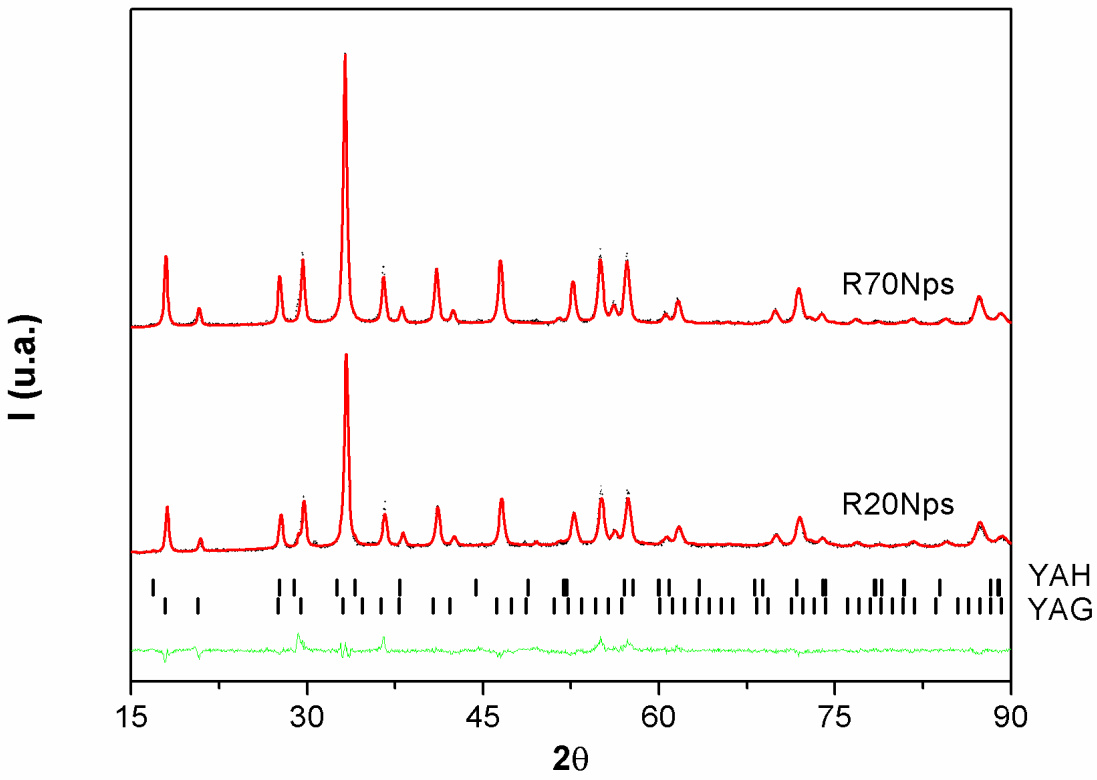

Figure 3.12. WAXS patterns (dots) and the Rietveld fits (continuous red lines) of the R20Nps and R70Nps samples. Bar sequences of YAG (COD code 2003066) and YAH (COD code 4341423) diffraction patterns (42) and the curve of residuals are shown along the bottom.

The patterns were analysed according to the Rietveld method [46] using the MAUD software [47]. The Rietveld best fit well reproduces the diffraction patterns of the two nanopowders.

The R20Nps sample is constituted by two crystalline phases, 98.9 (2) wt.% garnet YAG (cell parameter 12.0222 (6) Å) and 1.1 (2) wt.% hexagonal $YAlO_3$ (YAH, cell parameters a=3.680 (1) Å, c= 10.520 (9) Å), while the R70Nps sample is constituted by a pure garnet phase, with a lattice parameter value equal to 12.0182(7) Å. These results indicate that the features of the confined environment, where the precursors have been synthesized, have influence on the formation of the garnet phase.

TEM. Two representative TEM micrographs of R20Nps and R70Nps samples are reported in Figure 3.13.

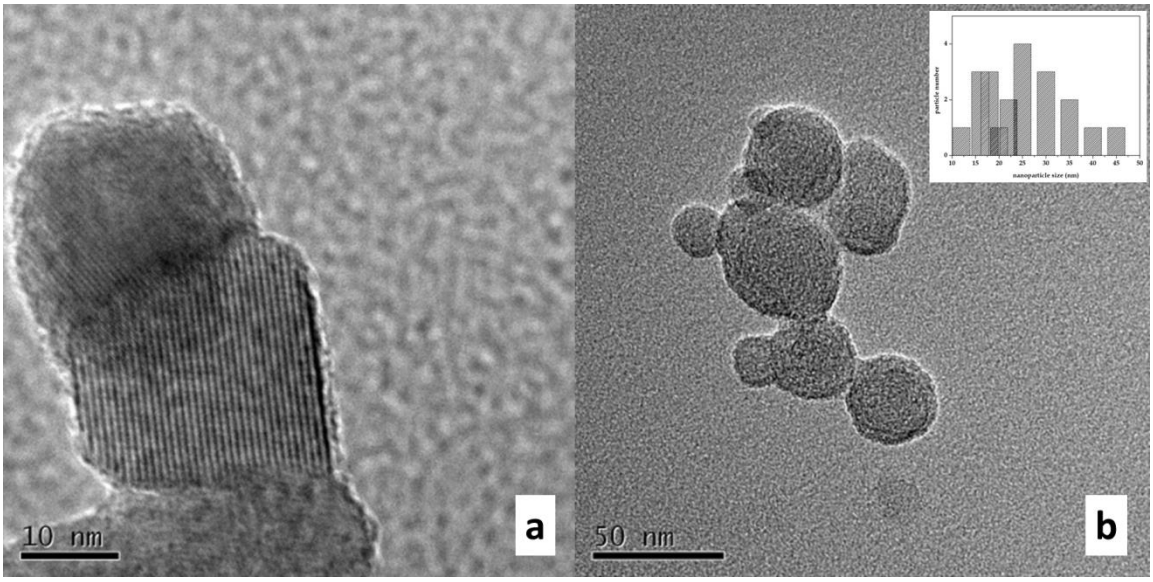

Figure 3.13. TEM micrographs of R20Nps (a) and R70Nps (b). Particle size distribution is reported in the inset of figure 3.13b.

The R20Nps sample is constituted by polygonal nanoparticle, whose average size is about 30 nm showing a certain tendency to agglomerate, while the R70Nps sample is constituted by well-defined spherical nanoparticles. The medium diameter is 25 nm, with the distribution shown in the inset of figure 3.13 b. The particles are less agglomerate then the previous and not sintered.

These findings further confirm the correlation between the structure of the confined environment and the structure and morphology of the obtained nanoparticles. The domain aqueous size affects the dimension of particles. In fact, the nanoparticles size is smaller when they are obtained from R20 microemulsion. The order degree determines the shape polydispersion and the agglomeration of nanoparticles. The nanoparticles have a well-defined shape and resulted less aggregated when prepared in the R70 microemulsion having the highest order degree.

3.1.2.3 Effect of thermal treatment

Considering the importance of nanoparticle physical features on optical properties and by taking into account the importance of temperature and duration of thermal treatment on the final properties of nanoparticles, the effect of the thermal treatment on the evolution of precursors, synthesized in the microemulsion toward the formation of YAG nanoparticles, has been also investigated.

The precursor synthesis of YAG nanoparticles has been performed following the procedure already reported in the paragraph 3.1.1.2. The two microemulsions were prepared at the same composition R = 70. This value was choice considering the morphological properties of the obtained particles and the high quality in terms of crystalline phase.

During the mixing a white hue sol was observed, indicating the formation of hydroxides. A complete precipitation occurred in 12 h. The precipitate was filtered and repeatedly washed with water to remove residual ammonia, nitrate ions, and surfactant molecules. The obtained white precipitate was over-night dried at 100 °C, then treated at 400 °C for 24 hours to remove the CTAB by complete oxidation. The obtained material was subsequently subjected to cumulative stages of thermal treatment at 500, 600, 700, 750, 800, 850, 900 and 950°C for 1 hour each. After each treatment, an aliquot was taken to be analyzed.

WAXS. The phase evolution process of the powder treated at various temperatures was followed by WAXS. The WAXS patterns of the samples treated at 400, 600, 800,

850 and 950°C are reported in Figure 3.14. The WAXS patterns of the samples treated at 500, 700, 750 and 900°C are reported in the Figure A1 of the Appendix 3.

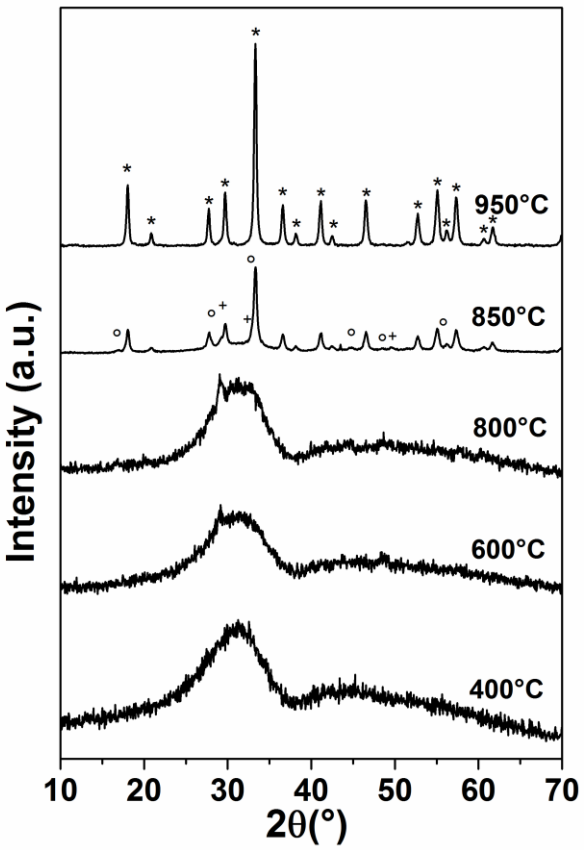

Figure 3.14. WAXS patterns of the samples thermal treated at 400, 600, 800, 850 and 950°C (YAG *, YAH ° and Yttria ⁺).

The sequence of patterns reported in the Figure 3.14 shows that the sample is completely amorphous up to 500 °C. The crystallization seems to occur at 600 °C for the thermal treatment conditions adopted.

In detail, the WAXS pattern of the sample treated at 600°C show a tiny peak at 29.1° ascribed to the (222) plane of the cubic yttrium oxide (Y_2O_3, yttria) phase. This peak, superimposed to the amorphous pattern of the hydroxides, indicates that, at this temperature small yttria crystallites are formed. The WAXS pattern of the samples treated at 700 and 800 °C does not significantly change: an increase of the (222) yttria

peak is observed together with the appearance of other tiny peaks at higher angles. The WAXS pattern of the sample treated at 850°C show a sequence of peaks superimposed to a fading amorphous band, thus indicating that the process of conversion of hydroxides into crystalline phases is effective in the range 750-850 °C. The crystalline pattern can be described in terms of three crystalline phases: yttria, yttrium aluminum garnet YAG and hexagonal yttrium aluminum oxide ($YAlO_3$, YAH).

The subsequent thermal treatment at 900 °C favors the complete crystallization process, since no discernible amorphous contribution can be detected above the background base line. Also in this case, the crystalline pattern is described in terms of yttria, YAG and YAH.

The WAXS pattern of the sample treated at 950 °C is described by only the garnet phase. Even if the sequence of phase transformation amorphous state - Yttria - YAH - YAG is well known [48], in this case the garnet phase is obtained at lower temperature. The pattern of the samples treated at 850, 900 and 950 °C were analyzed according to the Rietveld method [46] by using the MAUD software [47]. The Rietveld best fit well reproduces the diffraction patterns of each sample. WAXS patterns, the correspondent Rietveld fits and the residual plots are shown in the Figures A2 of the Appendix 3.

The results of the quantitative phase determination together with the cell parameter for each phase, crystallite size and lattice microstrain are reported in Table 3.3.

Table 3.3. The quantitative phase determination, cell parameter, crystallite size and lattice microstrain for each phase obtained by applying the Rietveld method to the WAXS patterns of samples treated at 850, 900 and 950 °C.

T (°C)	Phases	%$_{w/w}$	Cell parameter (Å)	D (nm)	microstrain
850	Amorphous	29 (2)			
	Yttria	1.7(1)	a = 10.615(5)	20(39)	0.0021(1)
	YAG	65.2(3)	a = 12.0247(4)	31.3(5)	0.0012(1)
	YAH	4.1(2)	a = 3.676(1) b = 10.499(6)	37(30)	0.0020(7)
900	Yttria	1.3(1)	a = 10.599(3)	30 (70)	-
	YAG	97.8(5)	a = 12.0197(6)	43.1(1)	0.0016(4)
	YAH	0.9 (1)	a = 3.676(5) b = 10.50(2)	36 (40)	-
950	YAG	100	a = 12.0196(5)	46.0(2)	0.0015(4)

The error is given in parenthesis. ICDD phase codes used: YAG 01-079-1891, Yttria 00-025-1200, YAH 01-074-1334

The cell parameter and the crystallite size, D, of the YAG phase are reported in Figure 3.15 as function of the temperature of the thermal treatment.

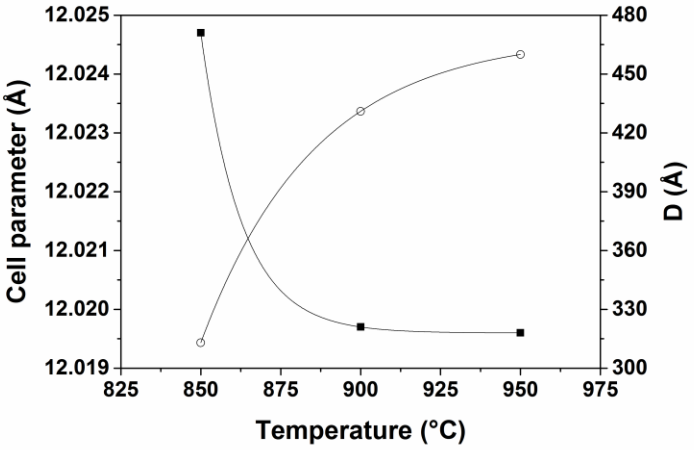

Figure 3.15. Cell parameter (■) and Crystallite size, D, (○) of YAG phase as function of temperature of the thermal treatment.

The contraction of the YAG lattice parameter as a function of the temperature is observed together with an increase of the crystallite size. Lines are guide eye only.

The cell parameter, *a*, decreases and approaches to the theoretical value (a = 12.016 REF ICDD) indicating that the crystalline lattice became neater on increasing the temperature. Various authors observed a similar trend for YAG powders doped with europium [49] and for variously doped YAG nanoparticles [50]. The cubic lattice parameter of the sample treated at lower temperature, larger than the equilibrium value in a crystal [51], indicates the presence of "homogeneous" disorder due to defects, vacancies and/or stacking faults in the garnet structure. Its decreases may be ascribed to the removal of this disorder and of impurities. The presence of appreciable line broadening was also evaluated within the Rietveld analysis. It is ascribable to small crystallite size D and to the presence of lattice microstrain, which is 0.0015 ± 0.0002 in average. The larger crystallite size at higher temperatures is in agreement with the already observed behavior of YAG nanoparticles [50].

TEM. TEM investigation was performed in order to investigate the morphology and to evaluate the particle size. This information is deemed necessary to speculate about the mechanism of formation of the garnet phase starting from precursors prepared via the microemulsion as confined environment. Some TEM micrographs at different magnifications of the samples treated at 400, 600 and 800 °C are reported in Figure 3.16. In the same figure, the SAED patterns acquired on the observed objects are reported.

The TEM micrographs clearly evidence various morphologies and sizes of the observed objects at the different temperature of treatment.

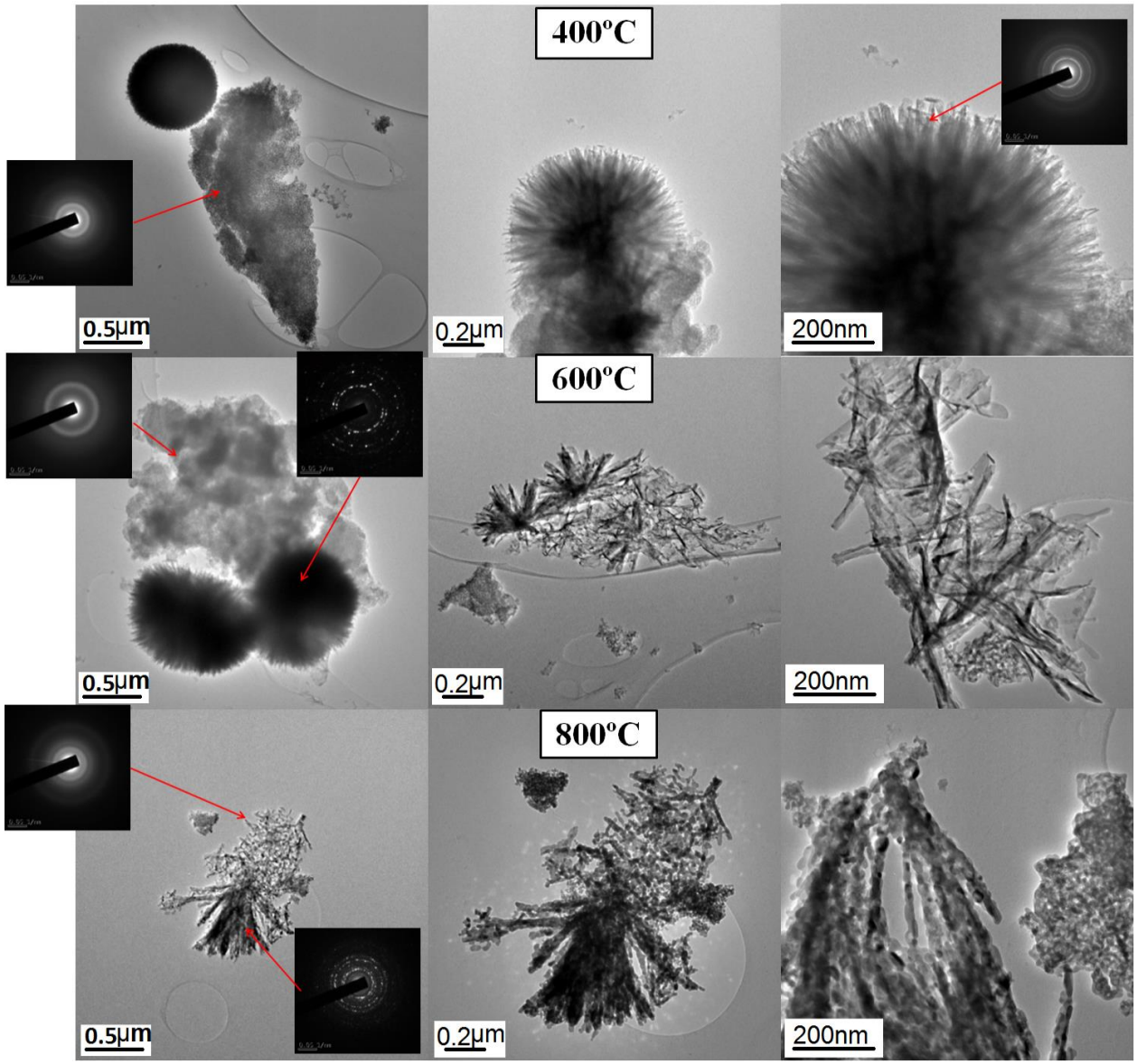

Figure 3.16. TEM micrographs and SAED patterns of the powders treated at 400, 600 and 800°C.

In detail, at 400 °C the system is constituted by big agglomerates and some hedgehogs (low magnification). Details of hedgehogs are given at higher magnification. The SAED pattern reveals that the agglomerates are amorphous. The hedgehogs of these aggregate are probably crystalline as suggested by the different contrast in TEM micrographs but the contribution to the SAED pattern is masked by the strong amorphous contribution. Moreover, the amorphous SAED pattern acquired on the hedgehogs indicates a different short-range structure as compared to

the one acquired on the amorphous particle. At 600 °C the system looks similar to that treated at 400 °C even if both the amorphous region and the hedgehogs seems to have a lesser electron density. It is relevant to notice that the SAED acquired on the hedgehog particles indicates their crystalline nature. This could be ascribed to the formation of a crystalline network growing radially from a central point thus maintaining the sunrays orientation. This is further confirmed at higher magnification; in fact micrographs evidence the presence of open hedgehogs of smaller size. The SAED pattern acquired on the amorphous particle is different from the one acquired at 400 °C thus indicating the formation of a more regular short-range structure. It has to be underlined that the diffraction ring (amorphous particle at 600 °C) lies at a very similar distance from the center as the crystalline spots (hedgehog at 600 °C). This could be assumed as an indication that the hedgehogs are the evolution, promoted by temperature, of the amorphous particles. At 800 °C the particles drastically change in shape and dimension. The hedgehogs appear lesser regular even if the wired structure maintains. Moreover, it has to be noticed that these wires are now formed by sequences of well-defined crystalline particles. This observed evolution indicates that the formation of the particles does not take place according to the Ostwald ripening phenomena. In order to get light on evolution of the system, the EDS analysis has been performed on the three observed objects. As an example, the EDS spectra of amorphous agglomerates and crystalline hedgehogs observed in the sample treated at 600 °C are reported in Figure 3.17. The EDS spectra of amorphous agglomerates, of crystalline hedgehogs and of the crystalline particles observed in the samples treated at 400 and 800 °C are reported in Figures A3 and A4 of the Appendix 3. In all spectra the signals of Ni and Cu, due to the grid, are present.

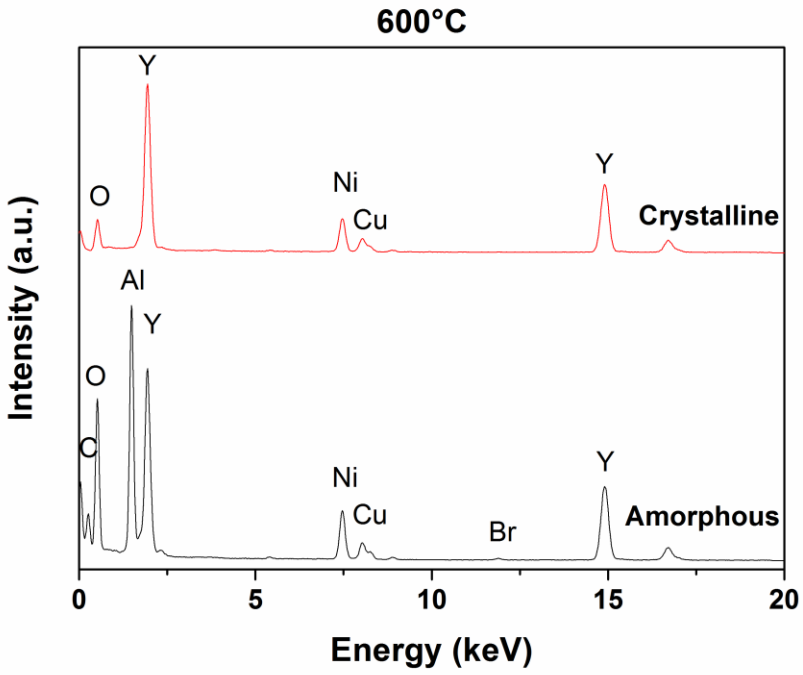

Figure 3.17. EDS spectra of the amorphous agglomerates and of crystalline hedgehogs observed in the sample treated at 600 °C.

The crystalline hedgehogs were mainly constituted by yttrium and oxygen while the amorphous agglomerates contained also aluminum. Furthermore, in the samples treated at 400 and 600 °C a peak of low intensity of bromine is also detected in the amorphous. This presence is unexpected because it is well know that the complete thermal degradation of CTAB take place at 400 °C [52]. Its presence is due to the yet not complete oxidation of bromide into bromine at the above considered temperatures probably as a consequence of the entrapment of this byproduct within the amorphous matrix, as considered for other processes [53]. It cannot be excluded the formation of a complex between aluminum ion and bromide due to their Lewis acid-base properties, this could improve the stability of bromide toward the oxidation reaction and affect the availability of aluminum to participate to the crystallization process.

On the basis of the above results, the crystalline hedgehogs are constituted by the yttria, in agreement with the WAXS patterns, which nucleation seems to occur

radially from a seeding point, followed by crystal growth, characteristic of dendrimer growth [54]. The formation of these germination nuclei is thermodynamically favored being the yttria phase stable at low temperatures [48]. To our knowledge, in literature yttria having these features has not been reported. This could be rationalized by considering a side effect played by the formation of byproducts. The bromide or, eventually, the aluminum bromide could interact with the yttria thus favoring its anisotropic growth along the (222) plane, as detected by WAXS. The drastic variation of the crystals morphology and particle size observed at 800 °C, where Al, Y and O are present within the particles, could be explained considering a combination of the oriented attachment mechanism [55] and the solid state diffusion governed by the Kirkendall effect. [55]. The first is responsible for the crystalline hedgehogs combination; the second for the mutual diffusion process through an interface of two metals having different diffusivity and occurs at the interface among amorphous aluminum oxide aggregates and yttria crystallites.

At this temperature, no evidence of bromine has been revealed in the EDS spectra, thus indicating that the oxidation process is complete. The absence of bromide makes aluminum fully available for the formation of mixed oxides.

Some TEM micrographs at different magnification of the samples treated at 850 and 950 °C are reported in Figure 3.18. In the same figure, the SAED patterns acquired on the observed objects are reported.

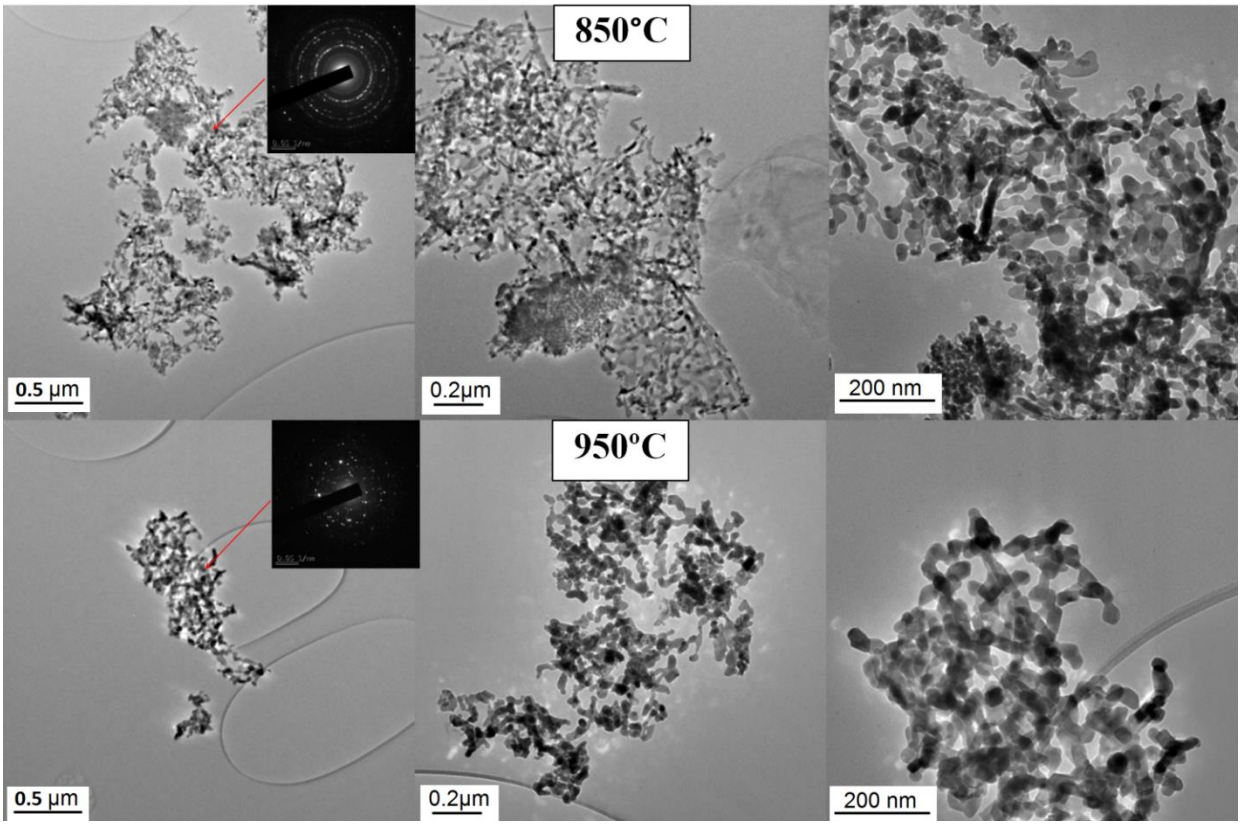

Figure 3.18. TEM micrographs and SAED patterns of the powders treated at 850 and 950°C.

Clusters of particles randomly distributed are detected at both temperatures. Regions of preferential agglomeration along one direction of these small particles are still present in the sample treated at 850 °C. The electron diffraction reveals their crystalline habits. The crowding of diffraction spots to form diffraction rings can be ascribed to the different orientation of small particles having the same crystalline structure. Increasing the temperature until 950 °C the system become homogenous and appears to be constituted by spheroidal particles of around 50 nm forming big agglomerate in which they are randomly distributed. The particles are crystalline, as evidenced by the SAED pattern in which the amorphous contribution is not appreciable anymore. Coalescence of some particles takes place.

In both samples, the EDS spectra (Figures A3 of the Appendix 3) show the presence of aluminum, yttrium and oxygen.

As a consequence of the treatment at 850 °C, knowing from WAXS pattern that the sample is constituted by yttria, YAH and YAG, the change in shape of the particles is

ascribable to the aluminum diffusion into the Yttrium rich particles. The driving force is a diffusion process promoted by the electrostatic attraction between the aggregates containing different elements, as claimed by Guo et. al [56]. This behavior can be yet explained in term of Kirkendal effect, generally, observed at the interface between core-shell systems [57].

The YAG particles formed at 950 °C appear to be strongly agglomerated and slightly irregular in shape as compared to the ones already reported in literature [58]. This indicates that the effect of the confined environment is determining in size control while the different thermal treatment could account for the different agglomeration. The one step thermal treatment reported elsewhere [58] could favor the formation of the YAG thermodynamically stable at high temperature, while the subsequent thermal treatment here investigated could favor the evolution of the yttria phase formed at lower temperature toward YAG.

On the basis of the proposed growth mechanism it is possible to exclude that the particles are connected as a consequence of the temperature effect as typically reported in literature [59]. This could be ascribed to the synthesis method that, due to the persistence of byproducts, influences firstly the formation of the yttria crystals then favors the anisotropic growth of particles.

It is well knows that the role of surfactants in microemulsion is the formation of confined environment that limits the particle growth [60]. After the separation of the precipitate from the medium, a small quantity of surfactant is electrostatically adsorbed on the hydroxides. As a consequence of the thermal treatments in air, it decomposes by oxidation producing volatile compounds. The presence of bromide as surfactant counterion, whose oxidation to bromide is considered quantitative around 400 °C, influences the formation of the crystalline phases and their growth in one direction, creating an alternative way to the well know evolution reported in literature for precursors synthesized by other wet chemical routes. The mechanism can be explained in terms of the oriented attachment mechanism at lower temperatures, while at higher temperatures the diffusion becomes dominant, probably by Kirkendall effect. Here, the surfactant plays a key role not only in the

synthesis of the precursors in microemulsion [58], but also in the second step of thermal treatment.

3.1.2.4 Effect of cerium Content

Cerium doping of the YAG crystalline lattice was performed in order to obtain the optical properties useful for the application in wLED. Considering the importance of doping agent content on optical properties [61], the effect of the cerium content on structure and optical properties of YAG nanoparticles has been investigated. The samples have been prepared in the bicontinuous microemulsion R70, resulted the more suitable to obtain separate nanoparticles in the previous study. The yttrium, aluminum cerium nitrate solutions (30 - x, 50 and x mmol L^{-1}, respectively) were prepared by dissolving proper amounts of $Y(NO_3)_3 \cdot 6H_2O$, $Al(NO_3)_3 \cdot 6H_2O$ and $Ce(NO_3)_3 \cdot 6H_2O$ in water in order to obtain 0.1, 0.2, 0.5, 1.0 and 2.0 % of cerium atoms with respect to total yttrium plus cerium atoms, according to the formula $Ce_xY_{3-x}Al_5O_{12}$.

Also in this case a white hue sol was instantaneously observed by the mixing with ammonia microemulsion. A complete precipitation occurred in 12 h. The precipitate was filtered and repeatedly washed with water to remove residual ammonia, nitrate ions, and surfactant molecules.

The obtained white precipitate was over-night dried at 100 °C, then treated at 900 °C for 1 hour. After calcination, a solid pellet is formed, the pellet has a yellowish coloration with tonality influenced by the cerium content.

WAXS. The WAXS patterns of the samples are reported in the Figure 3.19.

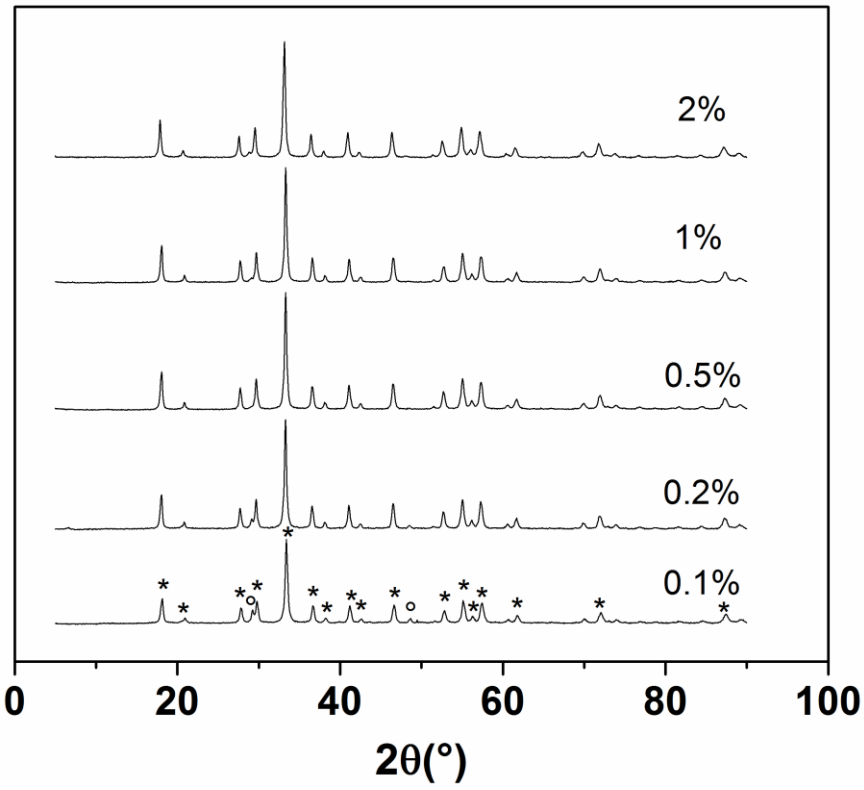

Figure 3.19. WAXS patterns of the samples, * indicates the YAG phase peaks, ° indicates the Y_2O_3 phase peaks.

Only the powders doped with 0.5% of cerium is constituted by the pure garnet phase while the others contain YAG and little amounts of yttria.

The patterns of the samples were analyzed according to the Rietveld method ([46]) by using the MAUD software ([47]). The Rietveld best fit well reproduces the diffraction patterns of each sample. WAXS patterns, the correspondent Rietveld fits and the residual plots are shown in the Figures A5 of the Appendix 3, pag.6. The results of the quantitative phase determination together with the cell parameter for each phase, crystallite size and lattice microstrain are reported in Table 3.4.

Table 3.4. The quantitative phase determination, cell parameter, crystallite size and lattice microstrain for each phase obtained by applying the Rietveld method to the WAXS patterns of samples at the different cerium content.

Ce %	Phases	%$_{w/w}$	Cell parameter (Å)	D (nm)	Microstrain
0	**YAG**	**100**	**a = 12.0182(7)**	**52(3)**	**0.00115(3)**
0.1	YAG	94(2)	a = 12.0249(6)	42(4)	0.00118(6)
	Y_2O_3	6(1)	a = 10.607 (1)	40(20)	----------
0.2	YAG	96(3)	a = 12.0263(4)	50(5)	0.00116(5)
	Y_2O_3	4(1)	a = 10.609(2)	39(4)	----------
0.5	**YAG**	**100**	**a = 12.0259(2)**	**50(4)**	**0.00149(1)**
1	YAG	98 (1)	a = 12.0255 (3)	54(5)	0.00153(2)
	Y_2O_3	1 (2)	a = 10.643 (5)	-----	----------
2	YAG	98(2)	a = 12.0262 (2)	46(2)	0.00124(2)
	Y_2O_3	2(1)	a = 10.659(4)	35(8)	----------

The error is given in parenthesis. ICDD phase codes used: YAG 01-079-1891, Y_2O_3 00-001-0831

The sample with 0.5% of cerium is constituted by the pure garnet phase, with a cell parameter value equal to a = 12.0259(2), higher than the undoped reference obtained at the same temperature (12.0182 (Å)). This is an indication of the presence of cerium into the garnet lattice. The cell parameters of the YAG and Yttria phases as function of cerium content are reported in Figure 3.20.

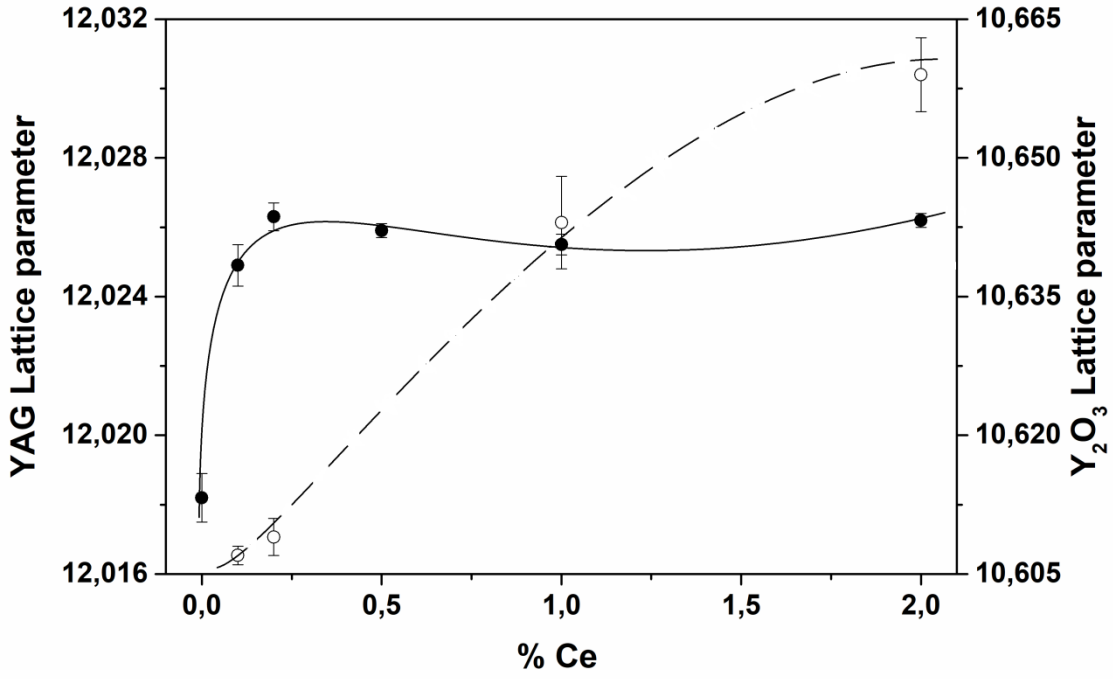

Figure 3.20. Cell parameter YAG (close) and yttria (open) phase as function of cerium content.

Lines are guide eye only. The increase of the YAG lattice parameter as a function of the cerium content is observed up to 0.5%. This increase is ascribable to the cerium substitution of yttrium into the cubic lattice, as other authors observed [50]. In case of 1 and 2% the lattice parameter is similar, in the limit of the error, to the one obtained doping at 0.5%, while there is a strong increase of the yttria lattice (yttria ref a = 10.599 Å). Probably, at these concentrations cerium is distributed in yttria more than YAG.

IR. The FT-IR spectra of Ce:YAG powders are shown in Figure 3.21.

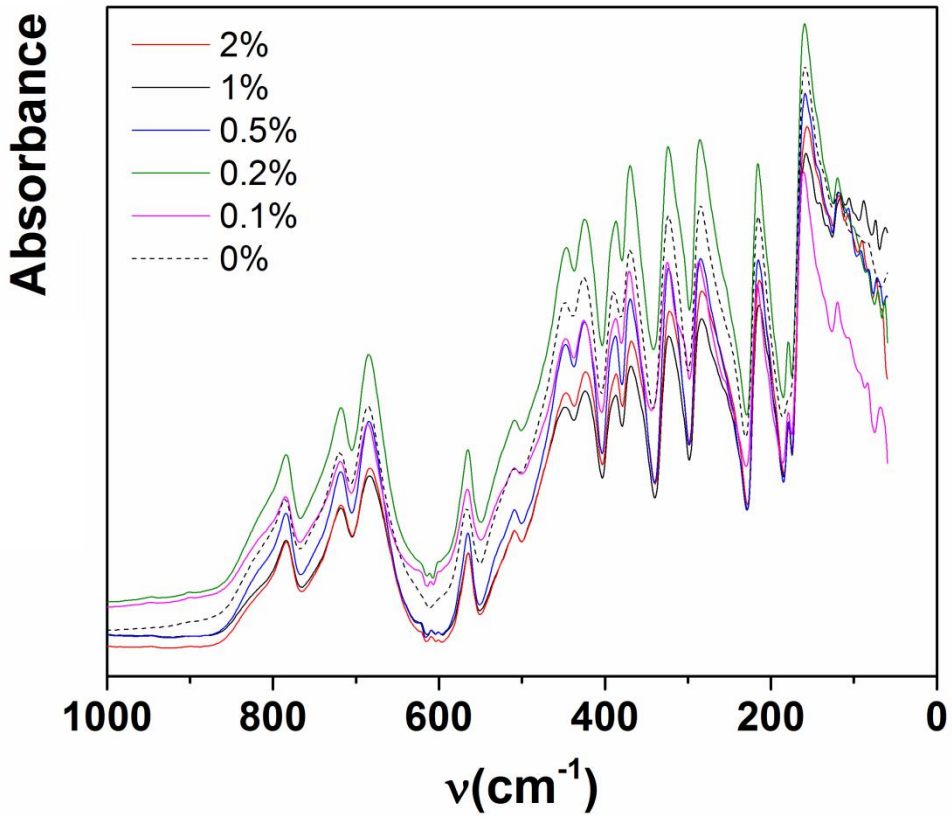

Figure 3.21. IR spectra of samples at different cerium content.

The same vibration bands are present in all spectra. The peak profiles is well sharp, which may be due to an high order degree of cations, in terms of the lattice positions. The peaks at about 790 and 684 cm^{-1} represent the characteristics Al–O metal–oxygen vibrations [62], while the peaks at about 720 and 565 cm^{-1} represent the characteristics Y–O metal–oxygen vibrations [63]. These characteristic metal–oxygen vibration absorptions are an indication of the formation of YAG structure. The characteristic yttria peaks at 560 e 700 cm^{-1} are covered by YAG bands [64].

However, on increasing Ce content; some small differences in terms of intensities ratio and shift of the vibration bands toward lower wavenumbers can be recognized. This observation suggests that Ce ions are statistically well dispersed into the YAG lattice, in agreement with the WAXS data.

In addition, a small new peak at 180 cm^{-1}, not present in the undoped YAG, appears.

No similar evidences are present in literature. It could be attributed to the one of the Ce-O vibration mode. Since this deepening is out of the scope of the thesis, this aspect was not considered.

TEM. TEM investigation was performed in order to investigate the morphology and to evaluate the particle size. Some TEM micrographs at different magnifications and EDS analysis of the samples at cerium content 0.5, 1 and 2% are reported in Figure 3.22. TEM micrographs evidence similar morphologies and sizes (~ 35 nm) of the observed objects at the different cerium content, similar the un-doped YAG obtained in the same conditions of microemulsion assisted synthesis. However, in some cases the particles agglomeration is different.

In detail, at 0.5% the system is constituted by clusters of particles randomly distributed. Increasing the cerium content at 1 and 2%, it is possible to identify clusters randomly distributed and the hedgehogs already seen during the study on the effect of thermal treatment. The EDS analysis was performed on all the investigated object. The agglomerates were constituted of aluminum, yttrium and cerium, while the hedgehogs contain only yttrium and cerium. This result confirms the WAXS and IR data analysis, evidencing the presence distribution of cerium both in YAG and yttria particles. Probably, the introduction of cerium into the yttria crystals avoids the phase evolution to YAG during the thermal treatment. On the other hand, Ce(III) could be insoluble in the garnet phase with the increase of cerium content, likely due to its ionic radius larger with respect to yttrium, according to the literature [50]. However, it is interesting to underline that generally in presence of cerium as dopant, the presence of cerianite phase has been observed at higher cerium contents. In the microemulsion assisted synthesis, where the surfactant interacts with the ions in the hydroxide precursors, not only it influences the particle size (see previous paragraph), but also the mechanism of formation, stabilizing the yttria phase respect to the cerianite. The cerium segregated from the garnet phase, which maintains the same cell parameter on increasing the cerium dopant, is thus solubilized in the yttria phase.

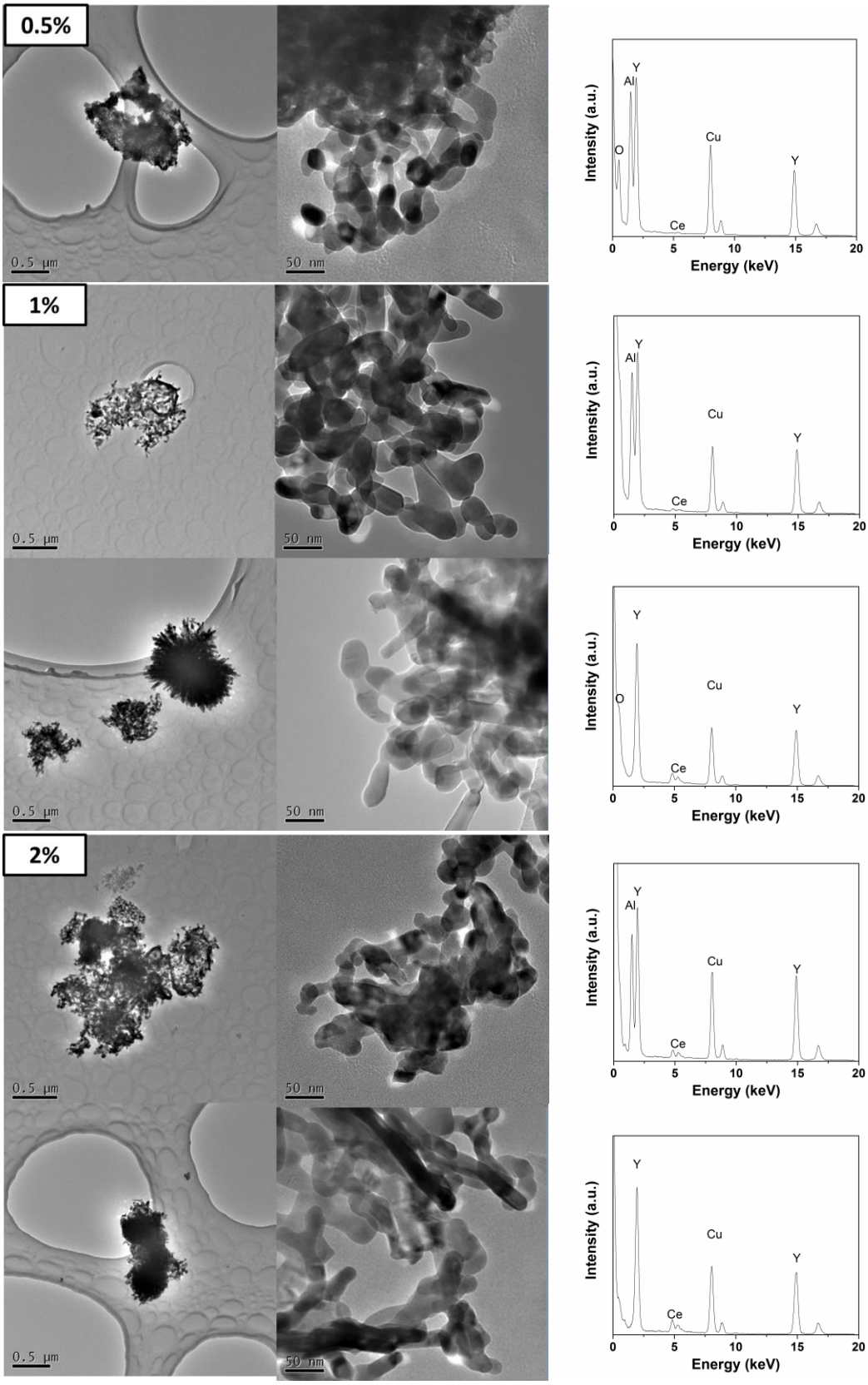

Figure 3.22. TEM micrographs and EDS spectra of the samples doped with 0.5, 1 and 2% of cerium.

Optical properties. In order to verify how the cerium content and distribution affects the optical properties of obtained materials, a detailed spectroscopic analysis was performed. The excitation and emission spectra of the powders at various cerium content are reported in Figure 3.23.

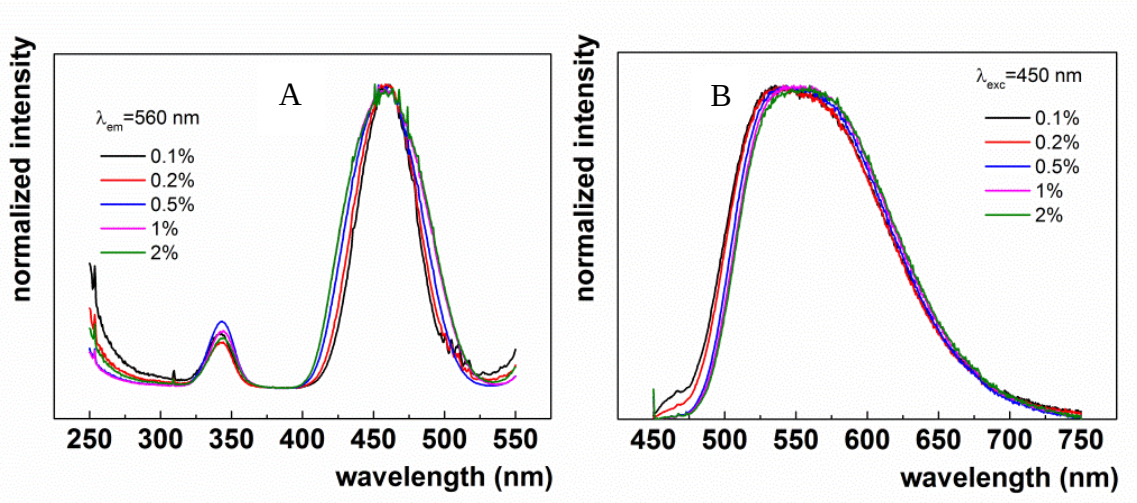

Figure 3.23. Excitation (A) and emission (B) spectra of the samples as function of cerium content.

The excitation spectra of obtained powders consist of two characteristic for Ce^{3+} ions absorption bands centred at 340 nm and 460 nm assigned to $^2F_{5/2} \rightarrow 5d^1$ electronic transition. Slight difference in relative bands' intensities can be found. Particularly, the intensity of 340 nm band is higher in respect to the 460 nm for the sample at 0.5% of cerium content. Emission spectra of obtained materials upon 450 nm excitation reveal the presence of inhomogeneity broadened emission that consists of two bands related with $5d \rightarrow {}^2F_{5/2}$ and $5d \rightarrow {}^2F_{7/2}$ electronic transition of Ce^{3+} ions. A little shift toward higher wavelength is observed on increasing cerium content.

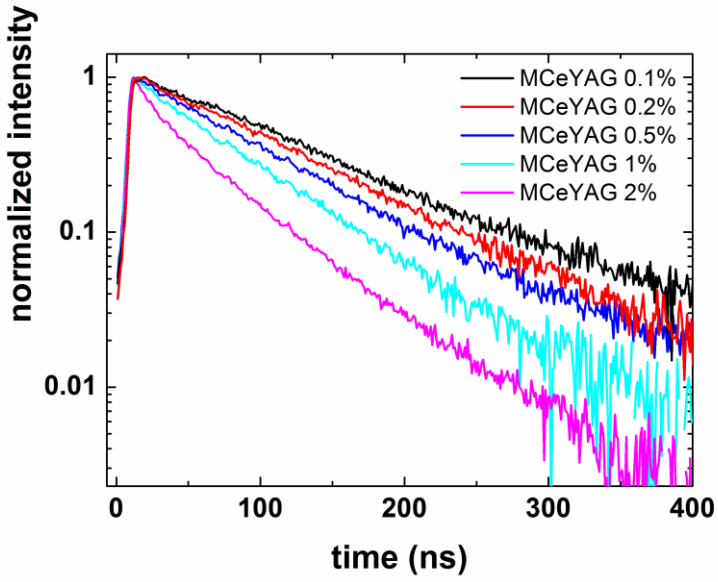

Figure 3.24. Room temperature luminescence decay profiles of Ce^{3+} ions of the powders as function of cerium content.

The analysis of the kinetics of excited state of Ce^{3+} ions reveals that the decay profile changes from simple single exponential to more complicated in case of higher cerium content, which may indicate that the cerium ions provide additional channels of nonradiative depopulation of $5d^1$ state.

The quantum efficiency of the Ce:YAG powders is reported in Figure 3.25.

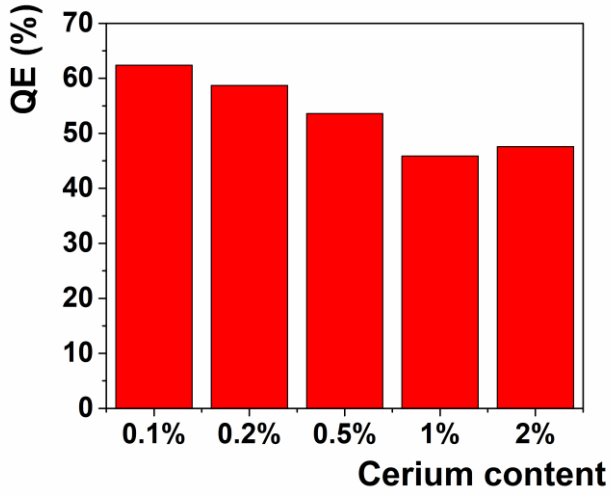

Figure 3.25 Quantum efficiencies of the powders as function of cerium content.

The QE reduction could be due to the nonradiative depopulation processes of the excited states related with the large amount of the Ce^{3+} ions is localized in the strongly defected surface area of the nanoparticle [49,50] according to kinetic observations. The effect of temperature on the powder at 0.5% is reported in Figure 3.26.

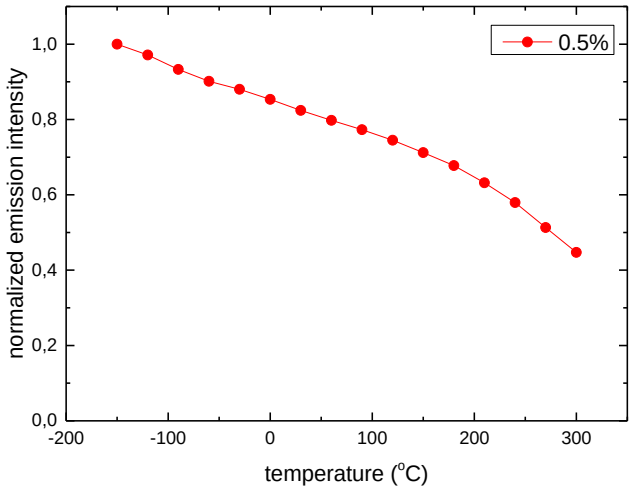

Figure 3.26. Emission intensity of the powders at 0.5% of cerium as function of temperature.

The emission intensity decrease on increasing temperature. At 300°C the emission is almost 55 % of the starting value.

The study reveals that Ce:YAG doped at 0.5% is the best system in terms of structural as well optical properties. It is composed of particles of pure garnet phase with a good distribution of Ce^{3+} ions. This structural characteristic confers good optical performances with high quantum efficiency and good thermal stability.

3.1.3. *Synthesis of Ce:YAG nanophosphors by Urea-Glass Route*

An alternative sol-gel based route (known as the Urea Glass Route, UGR [65]), previously established for the preparation of metallic nanoceramics has been here developed and tailored for the Ce:YAG nanophosphors.

The UGR was used thanks to its manifold advantages: it is simple, uses readily available and non-toxic precursors and requires lower reaction temperature compared to the classical ones. Thanks to the formation of an intermediate "gel-/glass-like" material (a complex between the urea and the metal precursor), the primary nanoparticles are stabilized during the heat treatment. In this way, the nanoparticles seeds can nucleate and growth but in a controlled way. These nuclei are loaded into an "intermediate" glass, an organic matrix formed upon decomposition of urea, which decomposes and leaves before the end of the reaction, avoiding post-synthesis purifications, and allowing the preparation of well-defined nanoparticles. Finally, by simplifying the reaction conditions the synthesis is also suitable for large scale production, knowing that a material, although valuable, has no practical applications when produced in small amounts [66,67].

3.1.3.1. Effect of Urea content

The formation of intermediate "gel-/glass-like" material is strongly dependent to the urea/metals molar ratio (R), therefore, it was decided to study the effect of this parameter on the physical and chemical properties of the starting materials. Results are presented in this paragraph.

273.9 mg of $YCl_3 \cdot 6H_2O$, 202.7 mg of $AlCl_3$ and 6.8 mg of $CeCl_3 \cdot 7H_2O$ were dissolved in 4 mL of ethanol. Proper amounts of urea were then added to the alcoholic salts solution to reach different R, according to the route of Giordano *et al.* [67]. A sample containing the metal salts with the same ratio, concentration and solvent, but in absence of urea (R0) has been prepared for comparison.

Figure 3.27. Photo of the starting materials obtained at different urea/metals molar ratio (R). The red square highlights the gel-like systems.

As shown in Figure 3.27, for R≤2 the starting materials are clear, homogeneous, colourless and form a colloidal dispersion. In Figure 3.28 it can be nicely observed the Tyndall effect in the R1 sample but not in the R0 using a red laser.

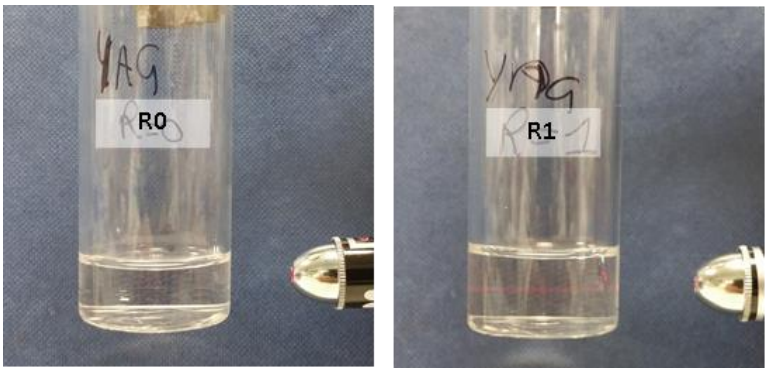

Figure 3.28. Tyndall effect observed by shining a red laser beam through the R=1 starting material (left), while no effect is observed in the R0 solution (right).

For R≥3, the formation of a white emulsion was observed, which separates within few hours.

In order to check the possibility to obtain YAG nanoparticles from the non-homogenous systems, the colloidal suspensions obtained at R ≥ 3 were calcined at 900°C and 1000°C. A white powder was obtained in each case.

The acquired WAXS pattern are reported in Figure 3.29.

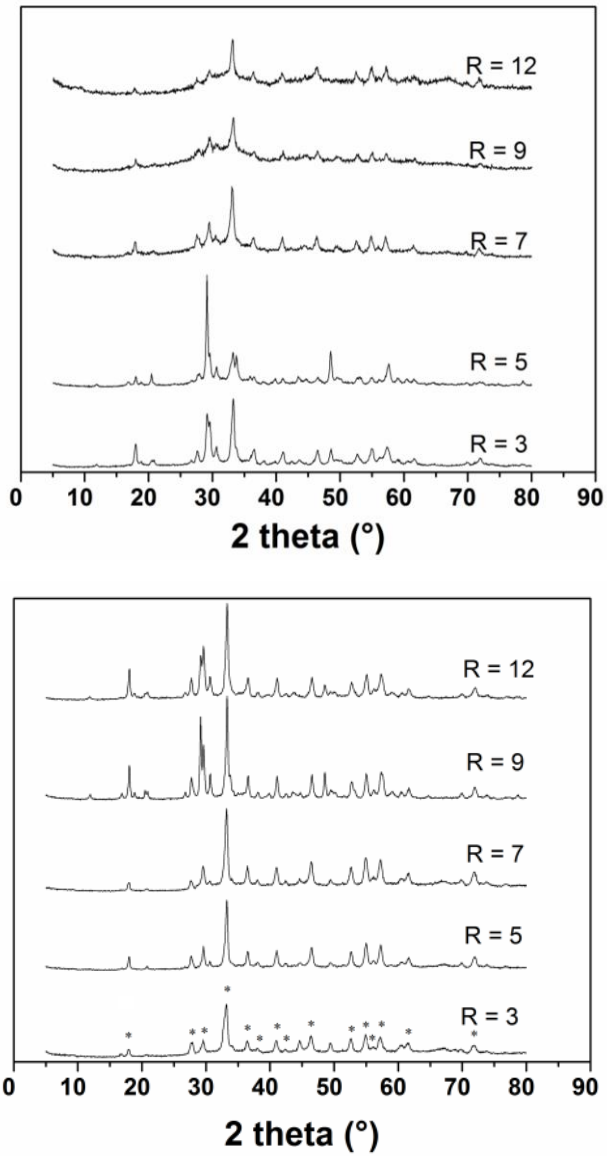

Figure 3.29. WAXS patterns of the powder obtained by thermal treatment at 900°C (up) and 1000°C (down) of suspension formed at several urea content. * YAG peaks.

All the patterns present the typical YAG peaks together with peaks of secondary phases. The patterns of samples treated at 900°C show the presence of amorphous, which disappear after treatment at 1000°C. The identified phase for each pattern of samples treated at 1000°C are resumed in table 3.5.

Table 3.5. Phases determination, obtained by the software X'Pert HighScore Plus of the WAXS patterns of samples obtained at 1000°C. Score indicates the probability of the phase assignation.

R	Crystalline phases	Score
3	$Y_3Al_5O_{12}$, YAG, garnet	81
	$Al_2Y_4O_9$, orthorombic	33
5	$Y_3Al_5O_{12}$, YAG, garnet	84
	$YAlO_3$, hexagonal	37
	$Al_2Y_4O_9$, orthorombic	49
7	$Y_3Al_5O_{12}$, YAG, garnet	76
	$YAlO_3$, hexagonal	41
	$Al_2Y_4O_9$, orthorombic	35
9	$Y_3Al_5O_{12}$, YAG, garnet	69
	$YAlO_3$, hexagonal	24
12	$Y_3Al_5O_{12}$, YAG, garnet	58
	$YAlO_3$, hexagonal	48

View the presence of secondary phases, also for samples treated at the highest temperature, the study has been continued on the systems where the homogeneous solution is obtained.

3.1.2.1 Gel-like precursors characterization

In order to tailor this method for the Ce:YAG synthesis, only homogeneous systems at R = 0, 1 and 2 (which are gel-like matrix) have been further processed.

IR. FT-IR investigations were performed in order to study on the nature of the gel-like starting materials. Spectra of the starting materials at R=0, 1 and 2, and R=1 prepared using aluminium and yttrium salts separately (respecting the total concentration used in the mixture) are shown in Figure 3.30. The IR spectra of pure urea and ethanol are also reported for comparison.

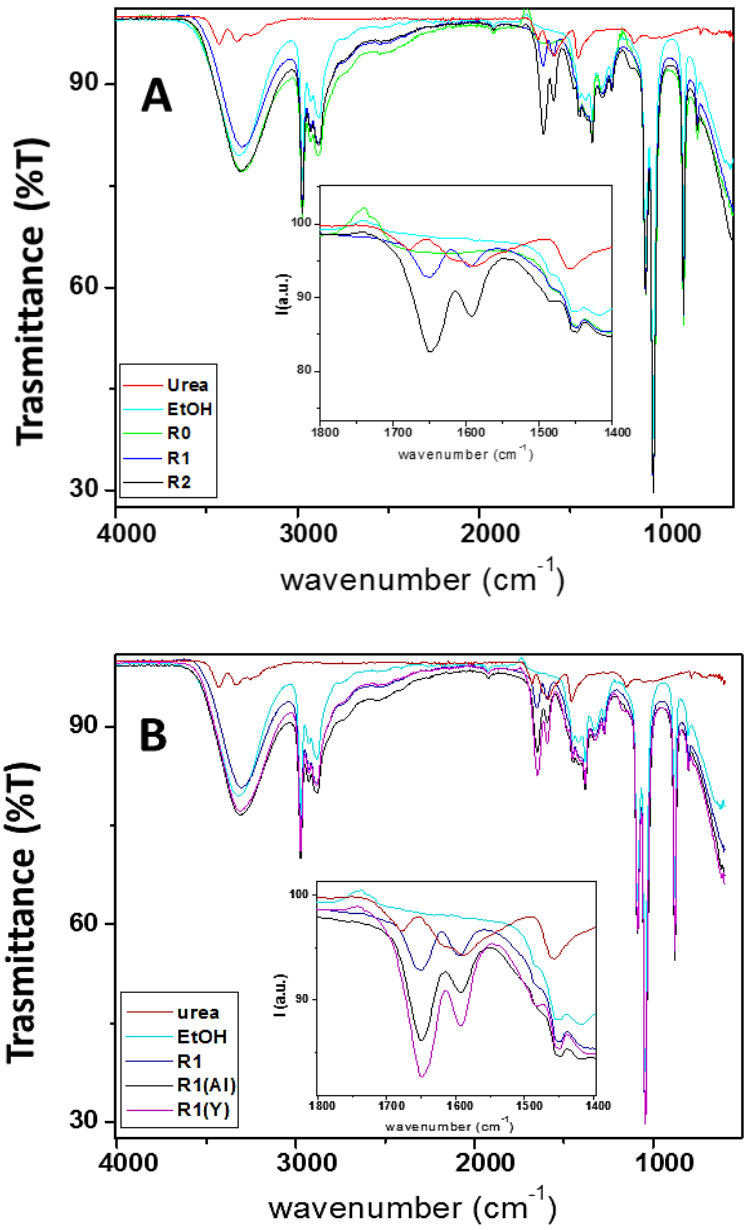

Figure 3.30. IR spectra of (A) the starting materials at R=0, 1 and 2 and (B) of system at R=1 containing alone yttrium and aluminum ions.

As it can be seen from Figure 3.30, the spectra are mainly dominated by the presence of ethanol, which seems to play the only role of solvating agent and does not take part to the coordination shell of the complex, as observed for instance for other urea metal complexes [67]. However, the urea carbonyl region (1650-1550 cm^{-1}) is free from solvent peaks and some considerations can be made. In this region for pure urea two bands can be observed, one centred at 1678 cm^{-1} and the other one at 1588 cm^{-1} (with a shoulder at 1616 cm^{-1}), attributed to the to the symmetric bending of NH_2 and to the

stretching of the C=O group (with the contribution of NH_2 asymmetric bending, as shoulder), respectively [68]. In the IR spectrum of the sample prepared at R=1, the small shoulder (due to the contribution of the NH_2 asymmetric bending) disappears and the C=O peak become sharper, slightly shifting to higher wavenumber (1595 cm^{-1} ← 1588 cm^{-1}). More interesting, the intensity of the peak of the symmetric bending of NH_2 increases appreciably and shifts to lower wavenumber (1650 cm^{-1} ← 1678 cm^{-1}). Although, both band shape and peaks position are different from those in the pure urea, they seem to be affected neither by R nor by the number of metal ions present in the complex (see Table 3.6).

Table 3.6. IR frequencies (cm^{-1}) for the metal-urea starting materials reported in Figure 3.30. The wavenumber of pure urea and corresponding attribution are reported for comparison.

Assignment	Urea	R1	R2	R1 [Y]	R1 [Al]
$\nu_s(NH_2)$	1678_{m}	1650_{st}	1648_{st}	1649_{st}	1649_{st}
$\nu_{as}(NH_2)$	1616_{sh}	--	--	--	--
δ (CO)	1588_{st}	1595_{m}	1592_{m}	1592_{m}	1593_{m}
***Legend**: s, as, ν, δ, indicate symmetric, asymmetric, stretching respectively. st, m, sh stand for strong, medium and shoulder.*					

On the other hand, the intensity of both peaks increases with increasing R and, more interesting, the ratio between the NH_2 and the CO peaks increase in the complexes (regardless of R).

On what concern the comparison between the spectra of sample R1 (which includes all metallic elements) and samples prepared with only one metal ion (Y^{3+} or Al^{3+} respectively) similar considerations can be done. In the monometallic samples, the carbonyl region shows two bands, centred at ~1650 cm^{-1} and ~1590 cm^{-1} in both cases, while the intensity and ratio of the NH_2 and the CO peak is very different, with a more intense NH_2 band.

Based on these findings, it is possible to assume that the presence of the metal ions might disrupt the H-bonds present in the urea network [69], and partially bond with

the NH_2 (possibly via electrostatic and dipole-dipole interactions). This seems to be confirmed by the disappearance of the $\delta_{as}(NH_2)$ contribution (as a shoulder in the CO peak) and the increase of the intensity for the $\delta_s(NH_2)$, which would indicate a difference in the dipole moment following the vibration. The presence of the metal ions close to the NH_2 groups might also shift the electron clouds on the N atoms, which would be slightly pauperize the C and come closer to the electron rich oxygen. The shift of CO band to higher wavenumber compared to pure urea (i.e. a stiffer C=O bond) seems to support this finding and excludes metal-urea bonds via oxygen bridges (the presence of the metal ion close to the oxygen would weaken and lengthen the C=O bond).

Thermogravimetry. The thermogravimetric (TGA) and the differential thermal gravimetric patterns (DTG) of the starting materials prepared with different ratios (R) are reported in Figure 3.31. For comparison and discussion purposes, the TGA and DTA curve of pure urea has also been included in the graphs.

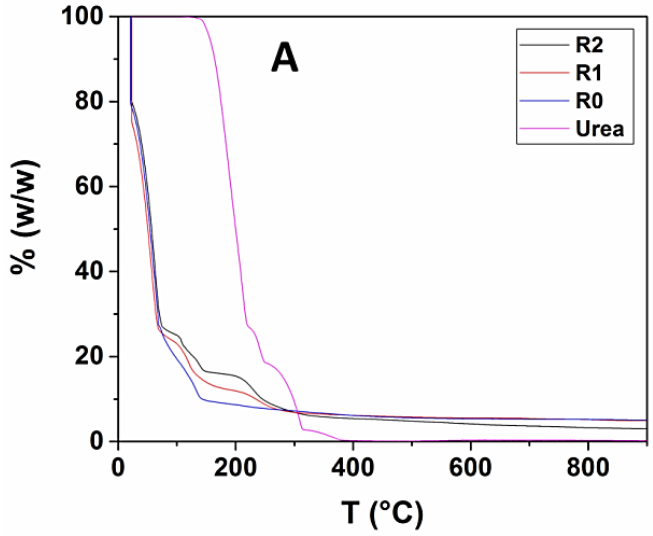

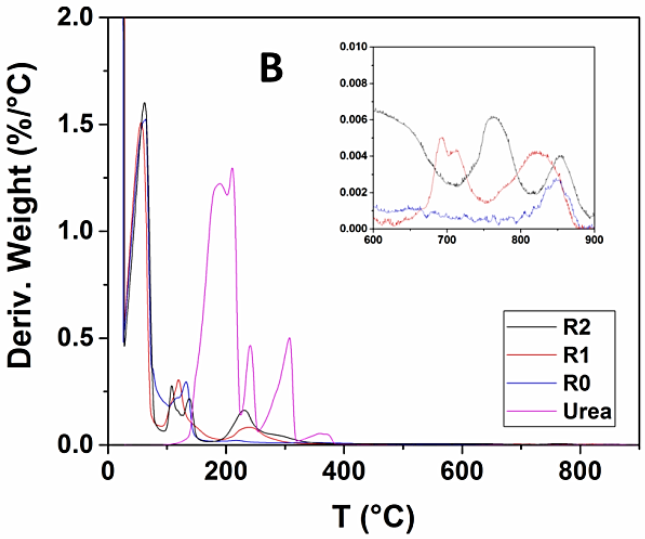

Figure 3.31. A) TGA and B) DTA patterns of the starting materials materials prepared with R=0, 1 and 2.

The TGA analysis reveals interesting discussion points. The dissimilarities between the decomposition patterns of pure urea and the sample prepared in absence of urea (R=0), with those of samples at R=1 and 2, confirm the formation of urea-metal complexes.

For pure urea (pattern recorded on the solid phase), decomposition starts at T~200°C and it is completed below 400°C as expected [70]. According to the work of Podsiadło, for the decomposition of pure urea under air three main steps are expected, involving the release of ammonia (up to T~250°C) and condensation reactions with formation of bigger molecules (including meleme and melone, up to T~300°C), which upon further temperature (T>300°C), increase decompose releasing mainly CO_x.

For the R=0 sample, after an initial solvent release (below 100°C) the final product is formed already at T~150°C and further temperatures increase might just assist the crystallization, as previously observed in similar studies [71,72].

For the complexes (R=1 and R=2), in both cases after an initial solvent release (below 100°C), samples decomposition takes place and it is completed below 300°C. However, the smoother decomposition of sample R=1 is similar to that previously observed for

urea-metal complexes [67], while R=2 decomposes in sharper steps, closer to those observed in the pure urea. This finding leads to think that only part of the urea is coordinated to the metal(s), while the rest is possibly allocating in an outer shell. More interesting, the complexes decomposition starts and it is completed at lower temperature compared to pure urea, which is opposite to what observed for other urea-metal complexes [67]. Together with the IR results (*vide infra*) it is possible to suppose that this behavior is due to the coordination of the central metal ion through the amine groups of urea (rather than via oxygen bridges as previously observed [73]), which would "break" the hydrogen bonding naturally presents in the structure of pure urea, and thus "de-structuring" the metal-urea network, which decomposes at lower T (compared to pure urea). On the other hand, according to the DTA, the formation of the final product occurs at higher temperature and passing by an intermediate.

3.1.3.2 Effect of thermal treatment

On the basis of the observed difference in the starting materials about thermal modification and ions-urea interactions, the effect of the thermal treatment on the evolution of the gel-like starting materials and the urea content, toward the formation of YAG nanoparticles has been investigated.

Samples at R < 2 were calcined up to 900°C (heating ramp 6°C/min). Thermal treatments at intermediate temperatures (300, 500, 700 and 800 °C) were performed to study the formation mechanism of the garnet phase. After reaching the final temperature and allowing 1 hour dwelling time, the samples were extracted from the oven and let cool down. The as-prepared material, after calcination and cooling down is a yellowish solid in form of small pellets, which were grounded in a mortar to obtain a fine powder (Figure 3.32).

Figure 3.32. Photo of the as-prepared powder from sample at R=1 calcined at 900°C.

WAXS. The corresponding powders, made without the use of any template, have been characterized by WAXS. The corresponding patterns are shown in Figure 3.33.

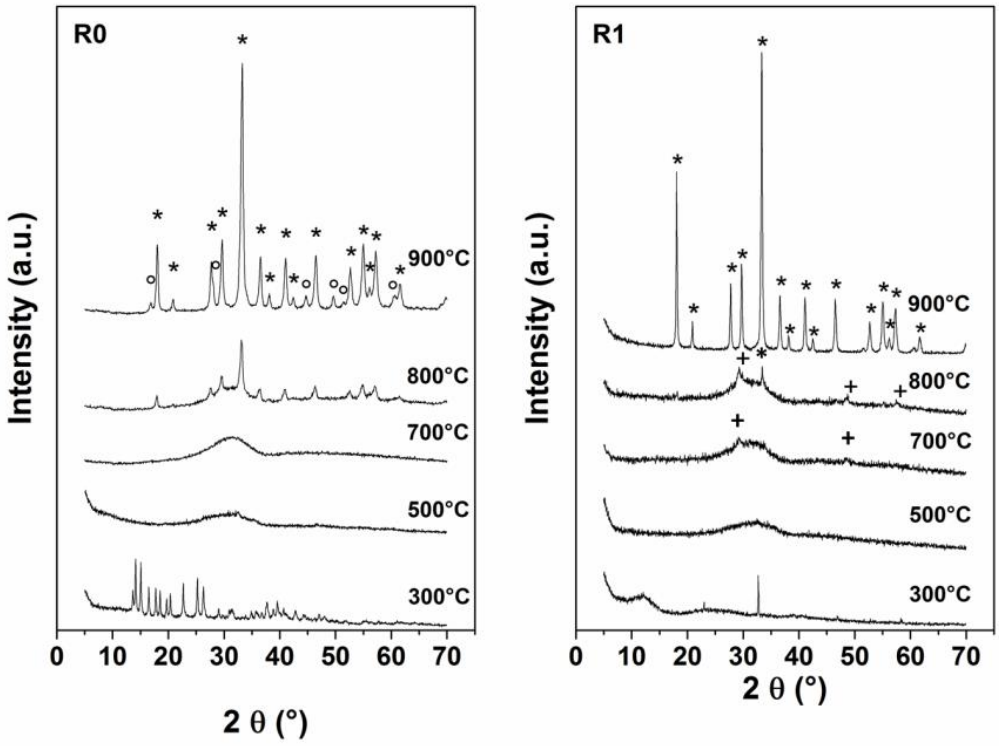

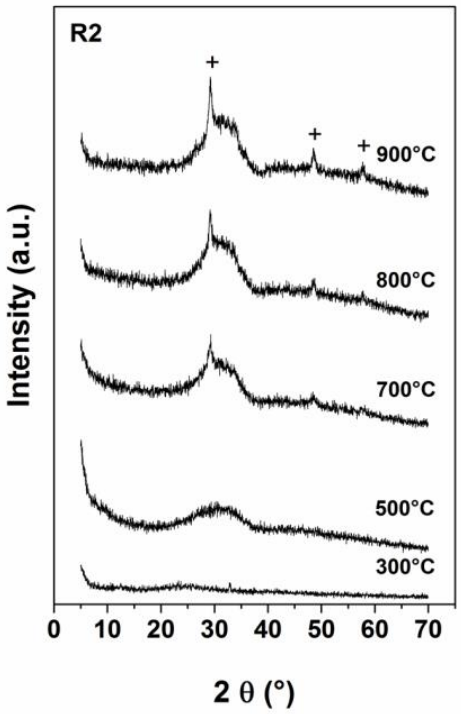

Figure 3.33. WAXS patterns of the samples obtained by thermal treatment of starting materials at R = 0, 1 and 2. Phases present at highest temperatures: * YAG, ° YAH and + yttria.

In the physical mixture of the metal salts prepared without addition of urea (R0), the crystalline phase after the treatment 300°C observed can be attributed to the mixture of reactants, $YCl_3 \cdot 6H_2O$ and $AlCl_3$ (see Figure A6 of Appendix 3), while only an amorphous phase can be observed at 500°C and up to 700°C. The formation of the crystalline garnet phase can be observed in the sample treated at 800 and 900°C, but together with large amount of an amorphous phase (55%) and of the hexagonal phase of yttrium aluminium oxide (YAH, 8.9%), respectively, according to the Rietveld refinement. For samples prepared with an initial ratio R=1 an amorphous halo is observed up observed up to 700°C. At 700°C, the two small peaks at 29.1° and 48.5°, superimposed to the amorphous, can be ascribed to the (222) and (440) planes of the cubic yttrium oxide (Y_2O_3, yttria) phase, while the WAXS pattern of the system treated at 800°C shows an increase of these peaks, alongside the appearance of the YAG main peak at ~33°. The pure garnet phase is observed at 900°C and no traces of other species are present. For the sample at R=2, mainly an amorphous phase can be

observed at any temperature, with traces of yttria observed for T>700°C. The intensities of these peaks increase with increasing T.

This finding indicates that for both samples (regardless of R) the formation of YAG does not start from a mere mixture of metal salts or hydrated salt, but follows the formation of the intermediate glass-like phase as expected within the urea-glass-route [67]. The intermediate phase is made by an organic matrix (resulting from the decomposition of urea), where the metal ions are loaded onto. During calcination, alongside the matrix decomposition, the nanoparticles start to nucleation and growth and, upon further increase of the temperature the nanoparticles crystallize. Noteworthy, the decomposition of the organic matrix (mainly constituted by C and N), creates a local reducing atmosphere which slow down the formation of oxides. The assistance of urea in creating a reducing atmosphere during the formation of YAG is somehow confirmed by the WAXS patterns of sample prepared at R=2, where the formation of the YAG phase cannot be observed even at T=900°C (only traces of yttria can be seen). On the other hand, in agreement with the IR data, these findings evidence the role of urea, which probably partially bond the aluminum and affect its availability to participate to the crystallization process, involving the formation of yttria, as reported by some of us in the case of YAG nanoparticles prepared via microemulsion assisted synthesis [74].

The Rietveld refinement [46] has been applied to the WAXS patterns of the samples treated at 800 and 900°C by using the MAUD software [47]. The Rietveld best fit reproduces well the diffraction patterns of each sample, the fit of sample R = 1 treated at 90°C is reported in Figure A7 of Appendix 3. The percentage of amorphous phase was determined by using the method proposed by Brindley et al.[75,76]. The results of the quantitative phase determination together with the cell parameter for each phase, crystallite size and lattice microstrain are reported in Table 3.7.

Table 3.7. The quantitative phase determination, cell parameters, crystallite size and lattice microstrain for each phase obtained by applying the Rietveld refinement to the WAXS patterns of samples.

Starting System	Temperature (°C)	Phase	%	Cell parameters (Å)	Crystallite size D (nm)	lattice microstrain
R0	800	amorphous	55.0 (1)	---	---	---
		YAG	44.1 (1)	a = 12.060 (3)	29 (1)	0.0033 (1)
	900	**YAG**	**91.1 (1)**	**a = 12.052 (4)**	**32 (3)**	**0.00233 (2)**
		YAH	**8.9 (3)**	**a = 3.674 (9) b = 10.522 (4)**	**32 (1)**	**0.0009 (7)**
R1	800	YAG	1.90 (1)	a = 12.015 (7)	45 (8)	err
		amorphous	97.0 (7)	---	---	---
		Yttria	1.10 (8)	a = 10.606 (5)	41 (9)	0.0049 (6)
	900	**YAG**	**100**	**a = 12.037 (5)**	**65 (2)**	**0.00160 (3)**
R2	800	amorphous	95.2 (15)	---	---	---
		Yttria	4.7 (3)	a = 10.600 (3)	26 (3)	0.0055 (5)
	900	**amorphous**	**92.2 (10)**	**---**	**---**	**---**
		Yttria	**7.8 (2)**	**a = 10.600 (3)**	**25 (1)**	**0.0060 (3)**

The error is given in parenthesis. ICDD phase codes used: YAG 01-079-1891, Yttria 00-025-1200, YAH 01-074-1334

The value of cell parameter of the garnet phase obtained from the starting system R = 0 treated at 800 and 900°C and R = 1 at 900°C is greater than the characteristic one (a=12.016 Å), indicating that the cerium ions have substituted the yttrium ions in the lattice. The presence of appreciable line broadening, also evaluated within the Rietveld refinement, is ascribable to small crystallite size D and to the presence of lattice microstrain.

It is worth to emphasize that the system R = 1 treated at 900°C give the highest production yield (100%) for YAG preparation in my knowledge.

TEM. To have a better insight of the nanoparticles size and morphology, TEM investigation has been performed. Micrographs of the powder R=1 at 900°C acquired

at different magnifications are shown in Figure 3.34. TEM reveals a plate-like shape of the nanoparticles in the powder (45±5 nm).

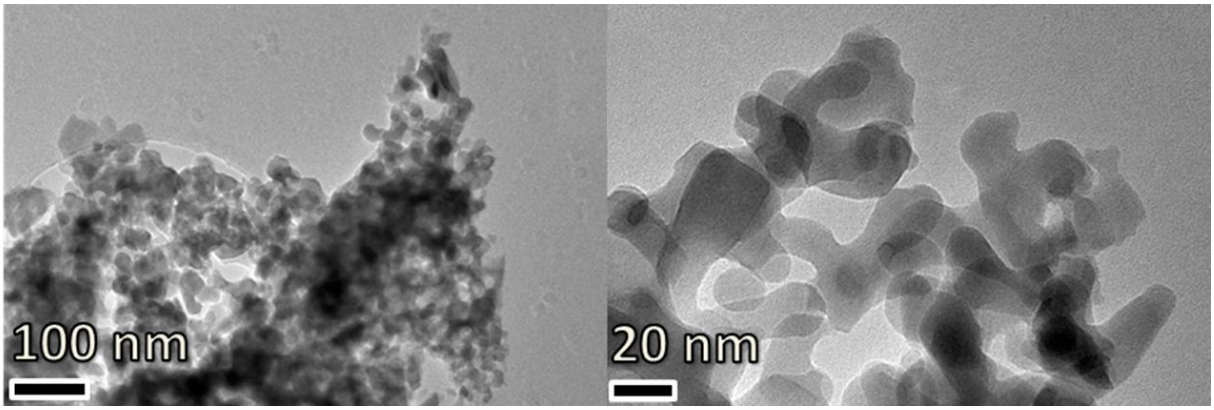

Figure 3.34. TEM micrographs of the samples obtained by calcining the starting material at R=1 at 900°C.

3.1.3.3 Effect of cerium Content

Considering the importance of doping agent content on optical properties [61], the effect of the cerium content on structure and optical properties of Ce:YAG nanoparticles has been investigated.

Solutions were prepared mixing $YCl_3 \cdot 6H_2O$, $AlCl_3 \cdot 6H_2O$ and $CeNO_3 \cdot 6H_2O$ in ethanol to give different cerium atoms content (0.1, 0.2, 0.5, 1.0 and 2.0 %) with respect to total yttrium plus cerium atoms according to the formula $Ce_xY_{3-x}Al_5O_{12}$. Proper amounts of urea were then added to the alcoholic salts solution to reach the optimum urea/metal salt molar ratio (R = 1), as reported in the previous paragraph. The obtained precursors solutions were thus calcined at 900°C to obtain crystalline powders. After calcination, a solid pellet is formed, the pellets have a yellowish coloration with tonality influenced by the cerium content.

WAXS. The WAXS patterns of the samples are reported in the Figure 3.35.

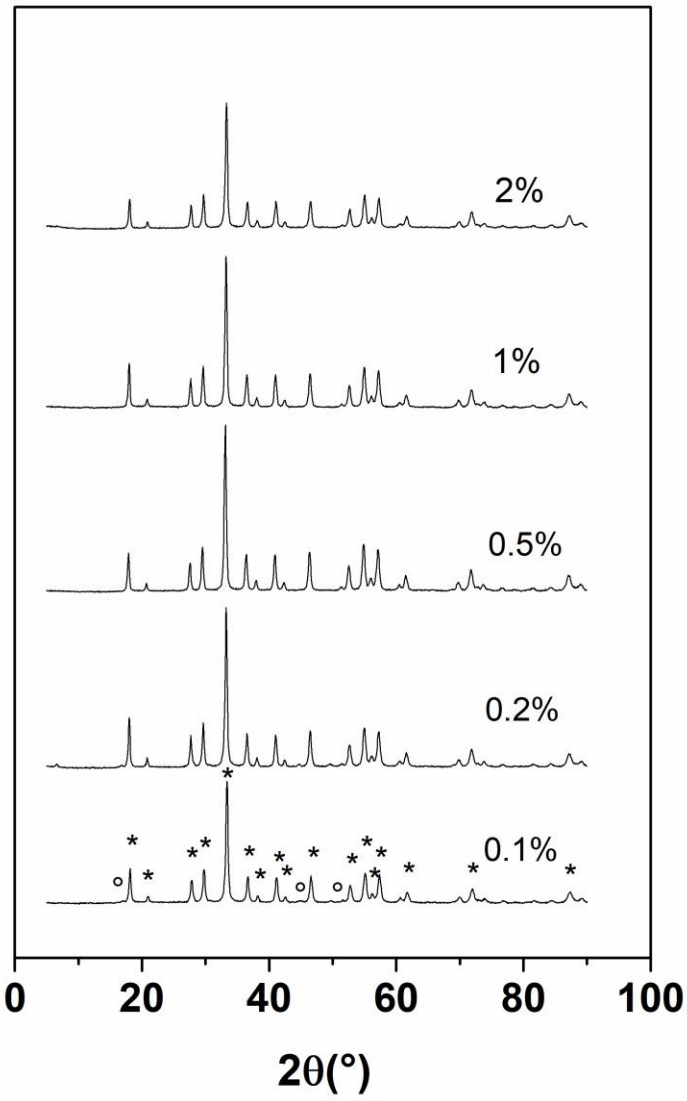

Figure 3.35. WAXS patterns of the samples, * indicates the YAG phase peaks and ° indicates the hexagonal aluminum and yttrium oxide phase peaks.

All patterns are described by the YAG garnet pattern.

The patterns of the samples were analyzed according to the Rietveld method (25) by using the MAUD software (26). The Rietveld best fit well reproduces the diffraction patterns of each sample. YAG cell parameter, crystallite size and lattice microstrain are reported in Table 3.8.

Table 3.8. YAG cell parameter, crystallite size and lattice microstrain obtained by applying the Rietveld method to the WAXS patterns of samples at the different cerium content.

Ce %	Cell parameter (Å)	D (nm)	Microstrain
0	a = 12.0429(6)	50(6)	0.00246(3)
0.1	a = 12.0433(6)	42(5)	0.00205(5)
0.2	a =12.0430(3)	50(6)	0.00206(3)
0.5	a = 12.0625 (4)	50(1)	0.00231(6)
1	a = 12.0497 (2)	54.5(4)	0.00240(3)
2	a = 12.037 (5)	65(1)	0.00232(6)

The error is given in parenthesis. ICDD phase codes used: YAG 01-079-1891

The cell parameters are higher that the *undoped* reference (12.0429 (Å)). This indicates that the cerium ions have substituted the yttrium ions in the lattice.

IR. The FT-IR spectra of Ce:YAG powders are shown in Figure 3.36.

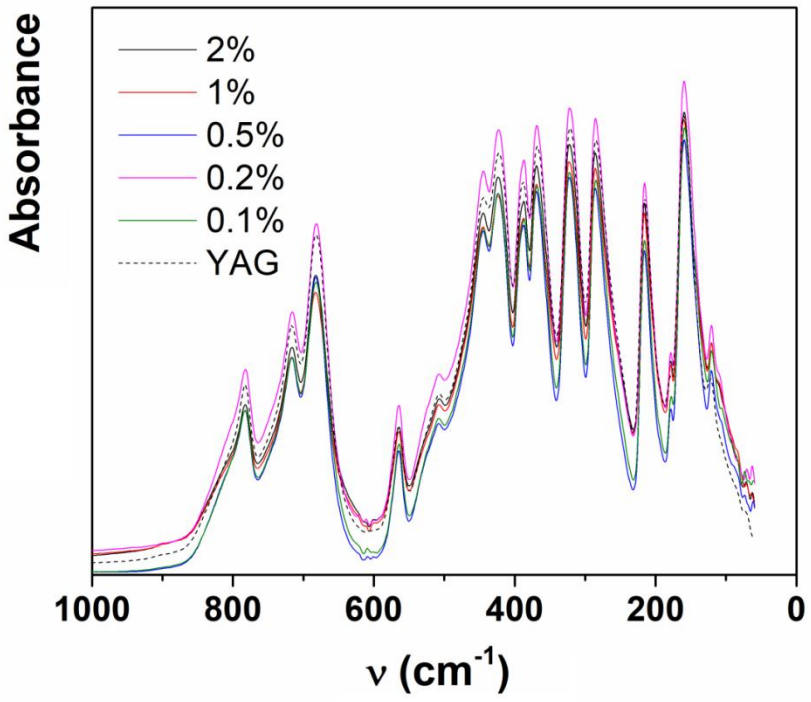

Figure 3.36. IR spectra of samples at different cerium content.

No signals are present at wavenumbers higher than 1000 cm^{-1}. The peak profiles are the typical of the YAG structure, as discussed in the paragraph 3.1.2.4. They are well sharp, indicating an high degree of ordering of cations, in terms of the lattice positions. This profile is sharper than the one obtained via microemulsion assisted synthesis. Also in this case it is possible to observe the appearance of a peak at about 180 cm^{-1} in the spectra of Ce:YAG samples.

Optical properties. In order to check how the cerium content affects optical properties of obtained materials, a detailed spectroscopic analysis was performed. The excitation and emission spectra of the powders at various cerium content are reported in Figure 3.37.

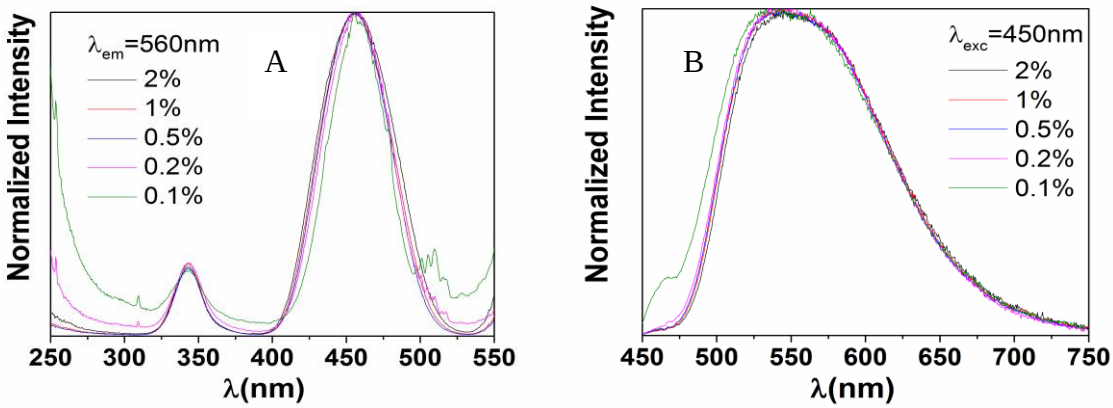

Figure 3.37. Excitation (A) and emission (B) spectra of the powders at 0.5, 1 and 2% of cerium

The excitation spectra of obtained powders consist of two characteristic for Ce^{3+} ions absorption bands centred at 340 nm and 460 nm assigned to $^2F_{5/2} \rightarrow 5d^1$ electronic transition. Emission spectra of obtained materials upon 450 nm excitation reveal the presence of inhomogeneity broadened emission that consists of two bands related with $5d \rightarrow {}^2F_{5/2}$ and $5d \rightarrow {}^2F_{7/2}$ electronic transition of Ce^{3+} ions. It is worth noting that an increase of the Ce content has negligible influence on the emission spectra what confirms good luminescent properties.

The quantum efficiency of the Ce:YAG powders is reported in Figure 3.38.

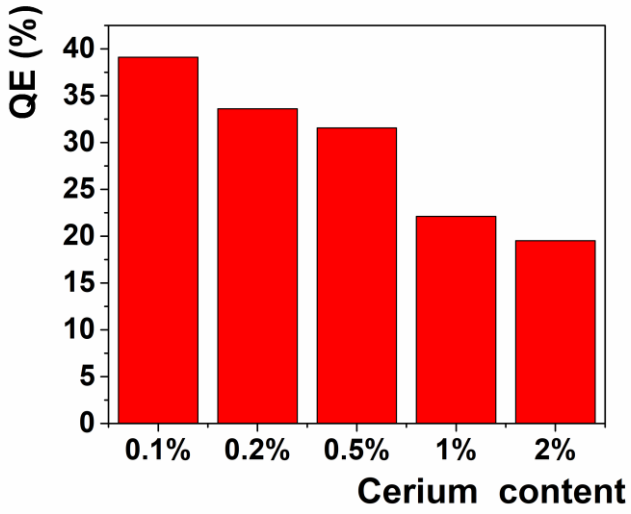

Figure 3.38. Quantum efficiencies of the powders as function of cerium content.

Also in this case the increase of Ce amount causes a reduction of the quantum efficiencies [49,50]. These values are smaller than the homologous obtained by microemulsion method, it could be due to the lattice microstrain, higher in the UGR powders.

The effect of temperature on the powders emission is reported in Figure 3.39.

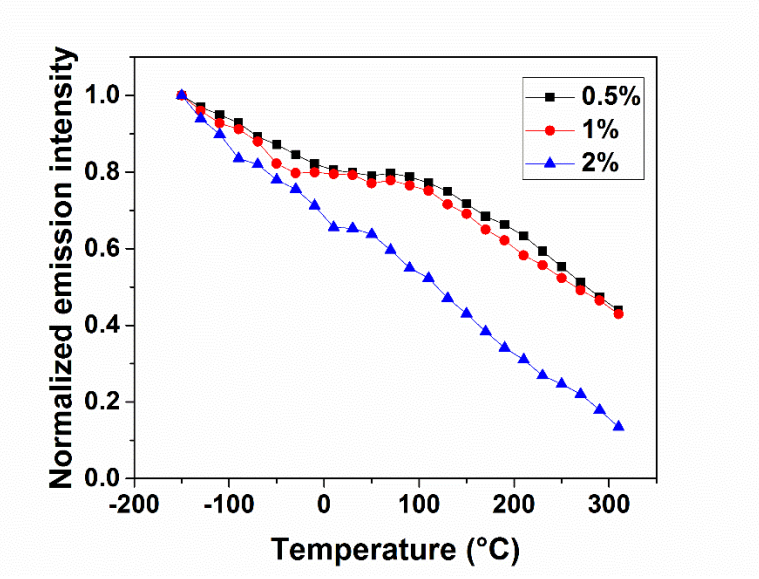

Figure 3.39. Emission intensity of the powders at 0.5, 1 and 2% of cerium as function of temperature.

As it can be seen, the emission intensity strongly decreases with the increasing temperature. The trend of the sample doped a 0.5 and 1% is similar. The emission of the system at 2% is more sensible to the temperature, particularly after 0°C there is a strong loss in emitted photons.

It is well know, that when the activator concentration in the host is too high, the luminescence is affected by so-called concentration quenching [77]. As the temperature increases, the electron transition distance and the probability of cross-relaxation are increased, leading to a loss of energy without light emission. The study reveals that Ce:YAG doped at 0.5% is the best system in terms of optical properties. It is composed of particles of pure garnet phase with a good distribution of Ce^{3+} ions. This structural characteristic confers an optimal optical performance with good quantum efficiency and thermal stability.

3.1.4 Considerations

Each synthesis method allows to the preparation of nanophosphors with different features.

The glicothermal synthesis provided nanoparticles with high amounts of secondary phases.

The microemulsion assisted synthesis allowed the production of pure garnet nanopowders with high quantum efficiency, at the proper amount of cerium ions, although big amounts of solvents and surfactants are required for the production of low quantities of powder (yield = 40% in weight), increasing the preparation's cost.

The Urea Glass Route (UGR) was the method giving the highest yield, and also using low amounts of ethanol as solvent. Furthermore, it can be considered economic, the readily available and non-toxic and efforts the possibility to a scaling up. Otherwise, the optical properties are lower than the ones observed in the nanoparticles from microemulsion.

Excluding the glicothermal ones, the developed synthetic routes gave good results.

On the basis of this observations the nanocomposites have been prepared by using the nanopowders prepared by UGR. The nanopowder with 0.5% of cerium content was considered the best system in terms of crystallinity and emission properties.

§ 3.2. Ce:YAG-PMMA Nanocomposites by solvent casting

The matrix polymer was PMMA (MW: 120,000 g mol^{-1}). PMMA was chosen as matrix for its good optical qualities.

PMMA dispersion have been prepared in chloroform. The dispersions of polymer were kept on shaker for 24 hours. Thus, Ce:YAG nanophosphor, obtained by UGR, were added to each dispersion in order to reach the 5%w/w respect to the polymer, following the better results reported in the Chapter 2, and sonicated for 1 h.

The nanocomposites are obtained by solvent casting method. The dispersions were poured into a circular silicon mold, kept at room temperature thus evaporating solvent in 24 hours.

For comparison with the composites, PMMA solution without filler was cast into another mold. The amount was chosen in order to obtain nanocomposites with different thickness.

Yellow solid nanocomposites disks, of diameter of 1 cm, composed of Ce:YAG nanoparticles in PMMA polymeric matrix, were obtained (Figure 3.40).

The thickness was measured by a micrometer (Table 3.9). The transparence of the nanocomposites decreases with the thickness.

Table 3.9. Thickness of the obtained Ce:YAG-PMMA nanocomposites.

Sample	Thickness (mm)
0.2	0.21
0.4	0.42
0.5	0.50
0.6	0.63
0.8	0.79

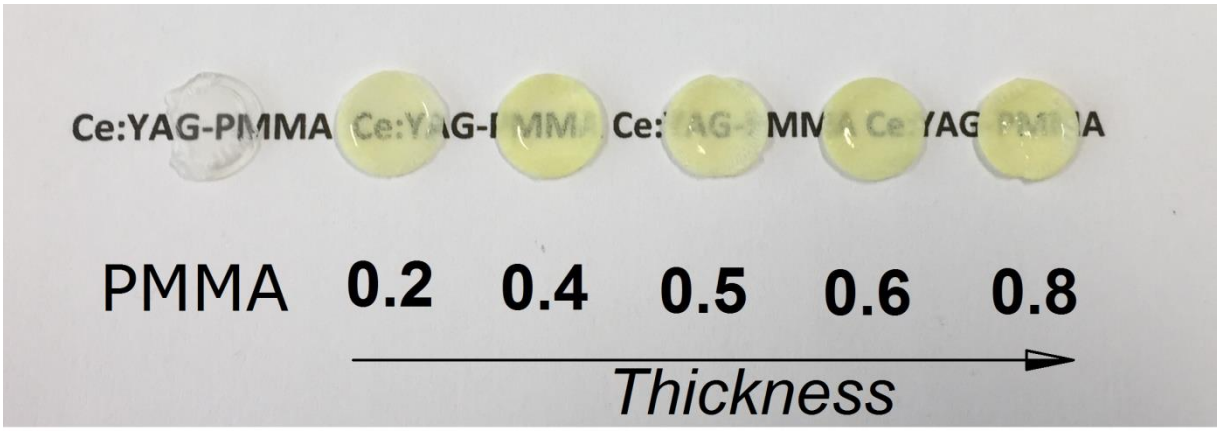

Figure 3.40. Ce:YAG Nanocomposite obtained by solvent casting at different thickness (mm). Pure PMMA is reported for a comparison.

3.2.1. Effect of nanocomposite thickness

The excitation and emission spectra of Ce:YAG nanopowder, of PMMA and of Ce:YAG-PMMA nanocomposites, measured at room temperature, are reported in Figure 3.41.

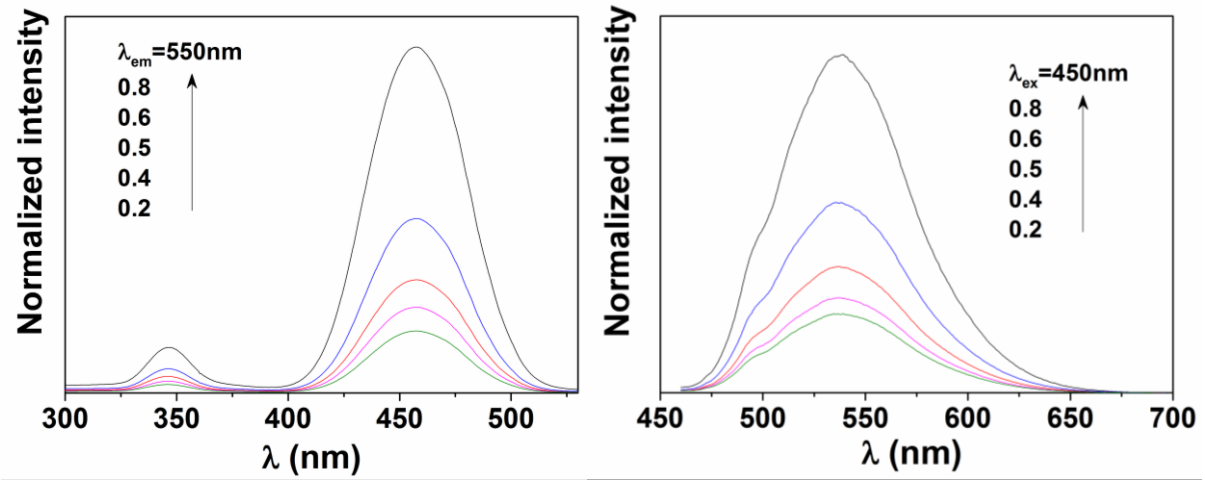

Figure 3.41. Excitation (left) and emission (right) spectra of Ce:YAG-PMMA nanocomposites.

The excitation and emission spectra of all nanocomposites show the large band centered at 460 and 540 nm, respectively, typical of Ce:YAG system. The band maximum increase with an increase in the thickness.

3.2.2. Application of nanocomposites in White LED device

White LEDs were prepared by combining a blue LED (InGaN, Quantum Light technology, Voltage 3.2 V, Current 350 mA) and the prepared Ce:YAG-PMMA nanocomposites. The emission spectra of the resulting light obtained by combining the Ce:YAG-PMMA nanocomposites with the blue LED and the relative CIE 1931 color space are reported in Fig. 42A and B, respectively.

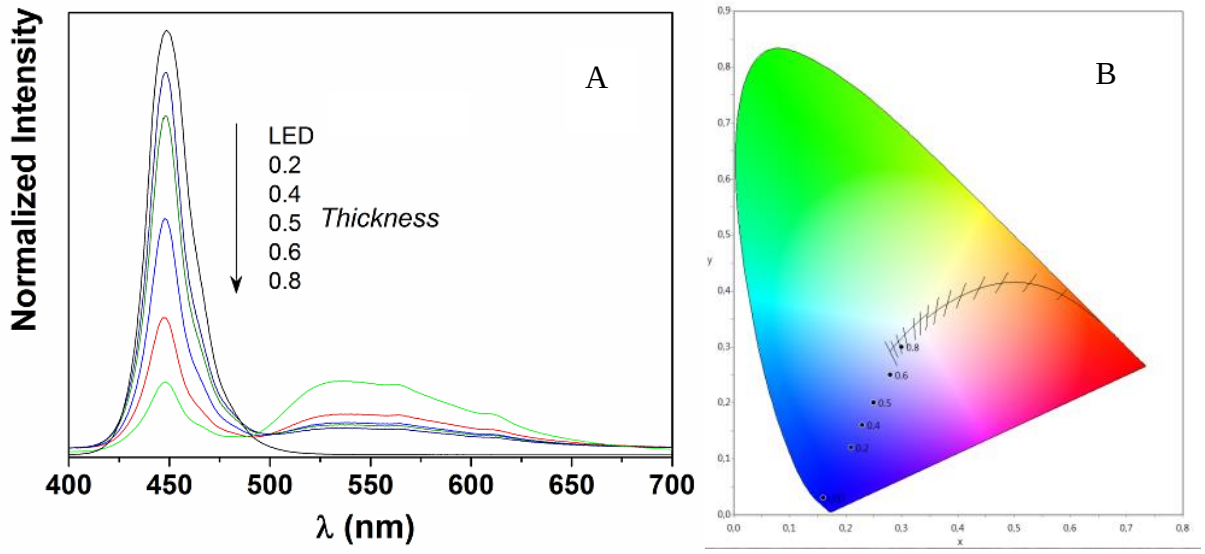

Figure 3.42. (A) Emission spectra and (B) the relative CIE 1931 colour space of the resulting light.

The emission spectra of the resulting lights consist of two bands centered at 450 nm and 550 nm. The first is due to the blue LED, the second one is due to the emission of the composite. The intensity of the emission at 450 nm decreases, while the one at 550 nm increases with increasing the composite thickness. The chromaticity coordinates, calculated from the emission spectra of the resulting lights, are reported in the Commission Internationale de l'Eclairage (CIE) chromaticity diagram (Fig. 42B). The CIE (x, y) coordinates of the lights shift towards white values on increasing the

thickness. The combination of the composites with a blue LED demonstrated that the light which better balances the blue light and the emissions from Ce:YAG is given by 0.79 mm thickness film. It, thus, can be used for a white LED device. It is worth to underline that white light is obtained by using a nanocomposite of 0.8 mm or composites of 3 mm in thickness.

3.2.3. Considerations

The solvent casting is a good method to obtain nanocomposites useful for the wLED device. The method is not expensive, requires low quantity of Ce:YAG nanophosphor and permits to modulate the white light modulating the thickness of the nanocomposites. The method can be select on the view of a scaling up of the process for the preparation of this kind of nanocomposites and processing on devices. In addition, since the shape of the nanocomposite can be tailored changing the shape of the container where the evaporation is done, the method can allow to obtain several objects in various shape and size, useful for a lot of kind of wLED devices. Respect to the composites obtained by using the commercial powders (see Chapter 2), the thickness of the more adequate nanocomposite is lower (3 mm respect to 0.8 mm). This could thus be a way to reduce the costs of the final product.

References

[1] M. Nyman, L.E. Shea-Rohwer, J. E. Martin P. Provencio, Chem. Mater., 21 (2009) 1536-1542.
[2] R. Kasuya, A. Kawano, T.Isobe, Appl. Phys. Lett., 91 (2007) 111916.
[3] J.A. Capobianco, F. Vetrone, T. D'Alesio, G. Tessari, A.Speghini, M.Bettinelli Phys., Chem. Chem. Phys, 2 (2000), 3203.
[4] R. Meltzer, S. Feofilov, S. P. Tissue, B. Yuan, Phys. Rev. , 60 (1999) R14012.
[5] M.L. Saladino, E. Caponetti, Optical Materials, 32 (2009) 89-93.
[6] E. Caponetti, S. Enzo, B. Lasio, M.L. Saladino, Optical Materials, 29 (2007) 1240-1243.
[7] X. Li, B. Zheng, T. Odoom-Wubah, J. Huang Ceram. Int., 39 (2013) 7983–7988.
[8] T.M. Chen, S.C. Chen, C.J Yu, Sol. State Chem., 144 (1999) 437.
[9] J. Marchal, T. Hinklin, R. Baranwal, T. Johns, R.M. Laine, Chem. Mater, 16 (2004) 822.

[10] M.L. Saladino, G. Nasillo, D.F. Chillura Martino, E. Caponetti, Journal of Alloy and Compounds, 491 (2010) 737–741.
[11] W.H.J. Byun, W.S. Song, Y.S. Kim, H. Yang, J. Phys. D: Appl. Phys., 43 (2010) 195401.
[12] D. Segal, J. Mater. Chem. 7 (1997) 1297–1305.
[13] A. Cabanas, J. Li, P. Blood, T. Chudoba, W. Lojkowski, M. Poliakoff, E. Lester, J. Supercrit. Fluids, 40 (2007) 284–292.
[14] X. Zhang, H. Liu, W. He, J. Wang, X. Li, R.I. Boughton, J. Alloys Compd., 372 (2004) 300–303.
[15] P. Ramanujama, B. Vaidhyanathana, J.G.P. Binnera, S. Ghanizadeha, C. Spacied, J. of Supercritical Fluids, 107 (2016) 433–440.
[16] R. Asakura, T. Isobe, J Mater Sci, 48 (2013) 8228–8234.
[17] A. Revaux, G. Dantelle, D.Decanini, A.M. Haghiri-Gosnet, T. Gacoin, J.P. Boilot, In Optical Materials, 33(7) (2011) 1124-1127.
[18] H. Jun, P. Qi, L. Xia, L.C. Jie, Bull. Mater. Sci., 36(7), (2013) 1191–1194.
[19] N. Jatupaiboon, Y. Wang, H. Wu, X. Song, Y. Song, J. Zhang, X. Ma, M. Tan, J. Mater. Chem., 3 (2015) 3130–3133.
[20] A.J. Zarur, J.Y. Ying, J.Y., Nature, 403 (2000) 65–67.
[21] M.L. Saladino, E. Kraleva, S. Todorova, A. Spinella, G. Nasillo, E. Caponetti, Journal of Alloys and Compounds, 509 (2011) 8798–8803.
[22] M.A. Scorciapino, R. Sanna, A. Ardu, F. Orrù, M. Casu, A. Musinu, C. Cannas, Journal of Colloid and Interface Science, (2013).
[23] C. Z. Dong, L. F. Zhang, S. Chen, M.X. Zhang, L. Feng, Z.M. Cui, Q.J. Zhang, Advanced Materials Research, (2013) 215–218, 652-654.
[24] L. Hu, C. Wang, S. Lee, R.E. Winans, L.D. Marks, K. Poeppelmeier, Chemistry of Materials, 25(3) (2013) 378–384.
[25] J.D.Furman, G. Gundiah, K.Page, N. Pizarro, A.K Cheetham, Chemical Physics Letters, 465 (2008) 67–72.
[26] E. Caponetti, D.F. Chillura Martino, M.L. Saladino, C. Leonelli, Langmuir, 23 (2007) 3947–3952.
[27] J.S. Pedersen, Current Opinion in Colloid & Interface Science, 4(3), (1999) 190–196.
[28] S.P. Moulik, B.K. Paul, Advances in Colloid and Interface Science, 78(2) (1998) 99–195.
[29] Y. Chena, F. Pana, Z. Guoa, B. Liuc, J. Zhangd, J. Mechanics and Physics of Solids, 84 (2015) 395–423.
[30] M. Sumita, K. Sakata, Y. Hayakawa, S. Asai, K. Miyasaka, and M. Tanemura , Colloid Polym Sci, 270 (1992) 134-139.
[31] X. Jia, J.-S. Hong, C. Yang, C.-Ji Fu, J.-Q. Hu, Microwave Conference (APMC), (2015) Asia-Pacific, IEEE Conference Publishing.
[32] M. Borkovec, H.-F. Eicke, H. Hammerich, B. Das Gupta, J . Phys. Chem., 92 (1988) 206-211.
[33] B. Lagourette, J. Peyrelasse, C. Boned & M. Clausse, Nature, 281(5726), (1979) 60–62.

[34] E. Caponetti, A. Lizzio, R. Triolo, Langmuir, 6(11) (1990) 1628–1634.
[35] S. H. Chen, S. L. Chang, R. Strey, Trends in Colloid and Interface Science IV (1990) 30–35.
[36] O. Diat, D. Roux, F. Nallet, Le Journal de Physique IV, 03(C8) (1993) 193–204.
[37] L. Blum, A. J. Torruella, The Journal of Chemical Physics, 56(1), (1972) 303–310.
[38] G. Gompper, M. Schick, Physical Review Letters, 65(9), (1990) 1116–1119.
[39] J. Kohlbrecher, I. Bressler , SASfit. PSI, Laboratory for Neutron Scattering ETHZ & PSI CH-5232 Villigen PSI, Switzerland, 2014, 0.94.6 edition http://kur.web.psi.ch/sansl/SANSS0ft/sasfit.html.
[40] M. Fanun, E. Wachtel, B. Antalek, A. Aserin, N. Garti, Colloids and Surfaces A: Physicochemical and Engineering Aspects, 180(1–2), (2001) 173–186.
[41] O. Regev, S. Ezrahi, A. Aserin, N. Garti, E. Wachtel, E. W. Kaler, Y. Talmon, Langmuir, 12(3), (1996) 668–674.
[42] K. V. Shubert, J. Chem. Phys., 101(6), (1994) 5343-5355.
[43] J. W. Falco, R. D. Walker & D. O. Shah, AIChE Journal, 20(3), (1974) 510–514.
[44] V. Vallet, M. Masella, Chemical Physics Letters, 618 (2015) 168–173.
[45] C. Houriez, M. Meot-Ner, M. Masella, The Journal of Physical Chemistry B, 118(23), (2014) 6222–6233.
[46] R. A. Young (ed.): The Rietveld Method, University Press, Oxford (1993).
[47] L. Lutterotti, S. Gialanella, Acta Mater, 46 (1998) 101.
[48] Y. Sang, Y. Lv, H. Qin, X. Zhang, H. Liu, J. Wang, X. Sun, R. I. Boughton, Ceramics International 38 (2012) 1635–1641.
[49] D. Hreniak, J. Holsa, M. Lastusaari, W. Strek, Journal of Luminescence 91 (2007) 122-123.
[50] M.L. Saladino, E. Caponetti, D.F. Chillura Martino, S. Enzo, G. Ibba, Optical Materials, 31 (2008) 261-267.
[51] M.L. Saladino, E. Caponetti, S. Enzo, Solid State Phenom., 128 (2007) 107.
[52] B. Wang, M. Zhou, Z. Rozynek, J.O. Fossum, Journal of Materials Chemistry, 19 (2009) 1816–1828.
[53] D. Chester Upham, Z.R. Snodgrass, M.T. Zavareh, T.B. McConnaughy, M.J. Gordon, H. Metiu, E.W. McFarland, Chemical Engineering Science 160 (2017) 245–253.
[54] P. Palmero, C. Esnouf, Journal of the European Ceramic Society, 31 (2011) 507-516.
[55] J. Qin, R. Yang, G. Liu, M. Li, Y. Shi, Materials Research Bulletin, 45 (2010) 1426-1432.
[56] D. Guo, L. Zhao, Y. Sang, H. Liu, S. Liub, X. Sunb, RSC Adv. 4 (2014) 55400.
[57] H.J. Fan, M. Knez, R.Scholz, D. Hesse, K. Nielsch, M.G. Zacharias, H. Shin, Nano Lett., 7 (2007) 993-997.
[58] F. Armetta, D. F. Chillura Martino, R. Lombardo, M.L. Saladino, M. Berrettoni, E. Caponetti, Colloids and Surfaces A: Physicochemical and Engineering Aspects, 511 (2016) 82-90.
[59] M. J. Kim, J.H. Park, K.Y. Lee, S. Lee, G.S. Han, H.J. Song, H. J. H. Shin, T.K. Ahn, H.S. Jung, ACS Appl. Mater. Interfaces, 6 (2014) 1145-1151.

[60] E. Caponetti, D.F. Chillura Martino, M.Leone, L. Pedone, M.L. Saladino, V. Vetri, J. of Colloid and Interface Science, 304 (2006) 413-418.
[61] C. Chien-Chih, T. Ming-Shyong, H. Min-Hsiung, J. Electrochem. Soc., 155(6), (2008) B517-B520.
[62] P. Colomban, J. Mater. Sci., 24 (8) (1989), 3002.
[63] P. Apte, H. Burke, H. Pickup J. Mater. Res., 7 (3) (1992), 706.
[64] R. Srinivasan, R. Yogamalar, A. Chandra Bose, Materials Research Bulletin 451165–1170 (2010).
[65] C. Giordano, M. Antonietti, Nano Today, 6 (4), (2011) 366–380.
[66] S. Glatzel, Z. Schnepp, C. Giordano, Angewandte Chemie, 52 (8), (2013) 2355–2358.
[67] C. Giordano, C. Erpen, W. Yao, B. Milke, M. Antonietti, Chem. Mater., 21 (21), (2009) 5136–5144.
[68] G. Clavel, V. Molinari, A. Kraupner, C. Giordano, Chemistry: Chem. Eur. J., 20 (2014) 9018-9023.
[69] K. A. Wood, R. G. Snyder, H. L. Strauss, J. Chem. Phys., 91 (9), (1989) 5255.
[70] S. Podsiadło, Thermochim. Acta, 256 (2), (1995) 367–373.
[71] P. Palmero, C. Esnouf, L. Montanaro, G. Fantozzi, Journal of the European Ceramic Society, 25 (2005) 1565–1573.
[72] E. Caponetti, M.L. Saladino, F. Serra, S. Enzo, Journal of Materials Science, 42 (2007) 4418–4427.
[73] Q. Gao, C. Giordano, and M. Antonietti, Small, 7 (23), (2011) 3334–3340.
[74] F. Armetta, M.L. Saladino, D. Chillura Martino, P. Livreri, M. Berrettoni, E. Caponetti, Journal of Alloys and Compounds, 719 (2017) 264-270.
[75] G. W. Brindley, Philos. Mag., 36 (1945) 347-369.
[76] J. C. Taylor, C. E. Matulis, J. Appl. Cryst., 24 (1991) 14-17.
[77] S. Shionoya, W. M. Yen, CRC Press, Phosphor Handbook, (1999) 108.

CHAPTER IV

Ln:YAG nanostructures on paper, cotton and glass wool

Up now YAG materials have been manufactured as single crystals, powders, ceramics or films and polymeric composites. In the last years, the researchers continue to create new materials with tailored and tuneable properties which enables them to be used in a broad range of applications, including optics, electronics, mechanics, protective coatings, sensors, functional textile fibres, drugs, biomedical materials, and many more. The possibility to prepare hierarchical nanostructures directly in one step process and to model previously the shape of the composite could be a great interest in order to improve the use of luminescent materials [1].

Biobased, eco-friendly, efficient procedures and economic template materials have been increasingly considered to give some novel and combined properties [2]. Some examples of hierarchical nanostructure are wood composites, utilized for a range of optoelectronics and energy efficient building materials [3], or mullite replica of hierarchical cellulose structures showing luminescence properties for fluorescent probes for sensing and detection as well as biological delivery systems [4]. In this research, the preparation of non-conventional hierarchical Ce:YAG nanostructures has been investigated.

The developed Urea Glass Route methodology, described in the Chapter 3, has been used for the preparation of hierarchical nanostructures. The gel-like starting material was used to embed three objects, called template, structurally different, i.e. paper (for integrating the present synthetic path with printing technique), cotton wool (for its natural "fluffy structure") and glass wool (for its fibres-like structures).

§ 4.1. Preparation by modified Urea-Glass Route

The gel-like starting material prepared with R=1 was used to embed three structurally different objects, namely paper, cotton wool and glass wool. Filter paper (Whatman), cotton wool (HypaCover extrafine) and glass wool (Assistent) were choice as templates. The samples were treated at 800°C and 900°C for 1 hour each. As previously observed for the case of metallic nanoceramics [5], also in the present case the macroscopic original shape of the template is remarkably preserved (Figure 4.1). As expected, calcining the templates in absence of the YAG precursors, the template loose its shape (Figure A7 of Appendix 3).

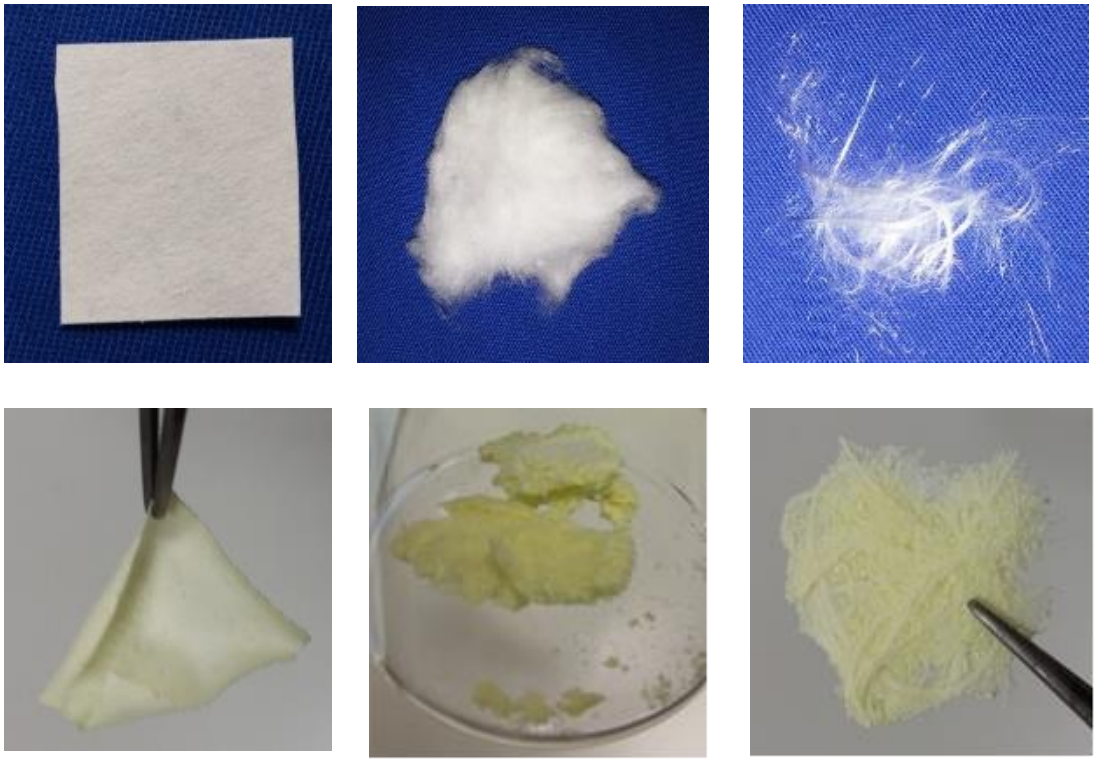

Figure 4.1. Photos of the template before calcination (up) and after calcination (previously soaked with the gel-like starting materials, down). From left to right: filter paper, cotton wool and glass wool, respectively.

For simplicity these systems will named "samples" (or using the name of the corresponding template). On the other hand, the sample prepared without any template will be named "powder".

4.1.1. Effect of temperature

The Wide Angle X-Ray Scattering (WAXS) patterns of the template samples are reported in Figure 4.2. For comparison, the WAXS pattern of the powder prepared in the same conditions without any template (at R = 1) is also reported.

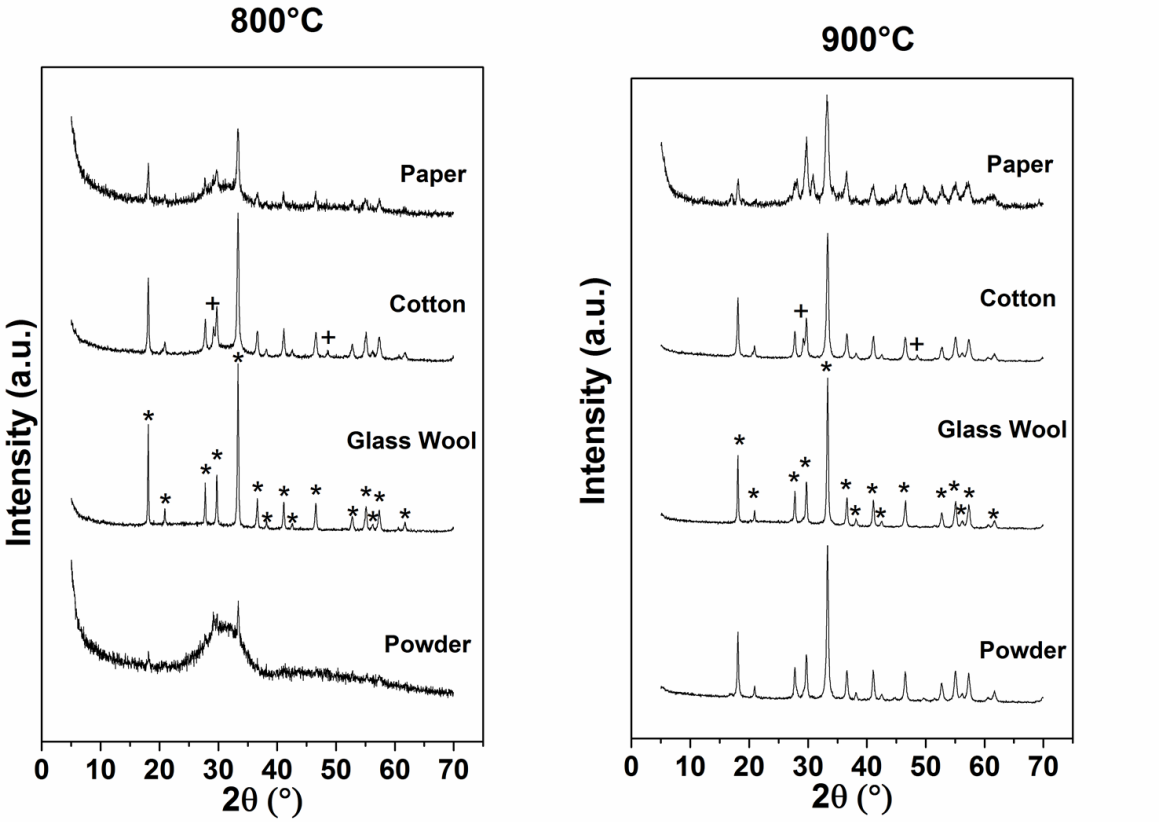

Figure 4.2. WAXS patterns of the powders and of the templated samples obtained by calcination at 800°C and 900°C with R = 1. * YAG, and + Yttria.

Differently than for the powder, in all samples prepared in the presence of a template crystalline phase(s) can be observed at both temperatures. However, only the WAXS patterns of the glass wool template samples, at both temperature, display the alone crystalline garnet phase. This finding is also unexpected because the powders obtained at 800°C is constituted by a mixture of garnet and yttria phase and amorphous. The results of Rietveld refinement to all WAXS patterns of the templated samples are reported in Table 4.1.

At both temperatures, for cotton and paper a mixture of different phases, more or less amorphous, can be observed. At 800°C, the YAG phase is 100%, 82% and 21% for glass wool, cotton and paper, respectively. At 900°C, the percentage of garnet phase increased in the cotton and paper samples but the amorphous phase is still present together with yttria as side products.

As for the powders, also in the glass wool template sample, the value of cell parameter of the garnet, obtained in the same conditions, is greater than the characteristic one (a = 12.0429 Å), indicating that the cerium ions have substituted the yttrium ions in the lattice. The crystallite size in the glass wool template sample is similar to the ones in the powder after the calcination at the same temperature, while the lattice microstrain is higher in the glass wool template sample obtained at 900°C indicating a more distorted garnet structure.

Nitrogen adsorption-desorption isotherms were obtained to gather information on the specific surface area (S_{BET}) area. The S_{BET} was 36.6 ± 0.1 m^2 g^{-1}, one order of magnitude greater than that of the same material obtained by co-precipitation method (3.15 ± 0.06 m^2g^{-1}) confirming that particles are smaller and/or their degree of aggregation is lower. Similar value has been obtained for nanoparticles prepared in microemulsion [6]. For the glass wool templated samples obtained at 800 and 900°C (GW800C and GW900C, respectively), the S_{BET} values are 9.36 ± 0.5 and 8.55 ± 0.4 m^2 g^{-1}, respectively. Both values are lower respect to the powder and very close to the S_{BET} of the glass wool (3.84 ± 0.6 m^2 g^{-1}) indicating that the two materials are similar to the glass wool used as support.

Table 4.1. The quantitative phase determination, cell parameters, crystallite size and lattice microstrain for each phase obtained by applying the Rietveld refinement to the WAXS patterns of the YAG-based nanostructures.

Support	Temperature (°C)	Phase*	%	Cell parameters (Å)	Crystallite size D (nm)	lattice microstrain
Powder	800	YAG	5.7 (3)	a = 12.023 (7)	46 (2)	err
		Yttria	1.6 (3)	a = 10.620 (1)	27 (4)	err
		amorphous	92 (12)	----	----	----
	900	**YAG**	**100**	**a = 12.037 (5)**	**65 (2)**	**0.00160 (3)**
Paper	800	YAG	21.4 (2)	a = 12.040 (4)	46 (4)	0.0021 (3)
		Yttria	1.4 (4)	a = 10.640 (3)	27 (9)	err
		amorphous	77 (10)	----	----	----
	900	YAG	60.9(2)	a = 12.111 (7)	28 (3)	0.0054 (4)
		Yttria	1.5(1)	a = 10.659 (4)	35 (9)	0.002 (1)
		YAH	8.5(3)	a = 3.677 (3) c = 10.51(1)	76 (4)	0.0032 (8)
		YAM	29(10)	a = 7.409 (8) b = 10.46(1) c = 11.13(2)	22 (2)	err
		amorphous	2(1)	----	----	----
Cotton	800	YAG	82.4 (1)	a = 12.035 (9)	49 (1)	0.0017 (1)
		Yttria	7.5 (2)	a = 10.609 (3)	28 (2)	err
		amorphous	10.1 (5)	----	----	----
	900	YAG	96.53 (1)	a = 12.036 (7)	42 (2)	0.00214 (2)
		Yttria	3.47 (9)	a = 10.606(2)	50 (4)	0.0017 (2)
Glass wool	**800**	**YAG**	**100**	**a = 12.030 (8)**	**103 (4)**	**0.00153(7)**
	900	**YAG**	**100**	**a = 12.041 (6)**	**74 (1)**	**0.00213(3)**

The error is given in parenthesis. ICDD phase codes used: YAG 01-079-1891, Yttria 00-025-1200, YAH 01-074-1334

Optical and electron microscopy studies were performed in order to investigate the morphology and to evaluate the particle size both in the as-prepared powder and in the glass wool templated samples. Optical microscope images of glass wool and of glass wool template samples obtained at 800°C and 900°C (GW800C and GW900C,

respectively) are reported in Figure A8 of the Appendix 3. The images show that the glass wool template samples obtained at 800°C are similar to the original glass wool (before calcination) even if the fiber are shorter and covered by particles.

SEM micrographs at different magnifications of the glass wool templated samples are reported in Figure 4.3. SEM micrographs of the original glass wool and of the powder are also shown. It is worth to note that the original glass wool shows a very smooth surface (Figure 4.3A) and that after the calcination at 800°C the fibers are melted and coalesced (Figures A9 of the Appendix 3).

On the contrary, GW800C sample had inherited the backbone of the original glass wool, converted however into a closely packed, well-structured and homogeneous layer of nanoparticles. The presence of "craters" on the structure of the templated sample (visible in the Figure 4.3B at higher magnification) clearly shows that the nanoparticles are not just lying on the surface but are part of the whole structure. The nanoparticles in the templated sample are plate-like but of more defined sizes, ranging from 20 to 40 nm.

The GW900C (Figure 4.3C) did not maintain the fibrous appearance of glass wool. Blocks from coalesced fibers are observed; unorganized clusters of nanoparticles, mainly plate-like and with sizes ranging from 20 to 50 nm are present, similar to the ones observed in the powder (Figure 4.3D).

The local composition of the obtained templated samples were investigated by EDS. The X-ray fluorescence spectra acquired for some nanoparticles (Figure A10 of Appendix 3), show the peaks of yttrium, aluminum and cerium present in the samples, including calcium, potassium, sodium, magnesium, and silicon of the glass wool.

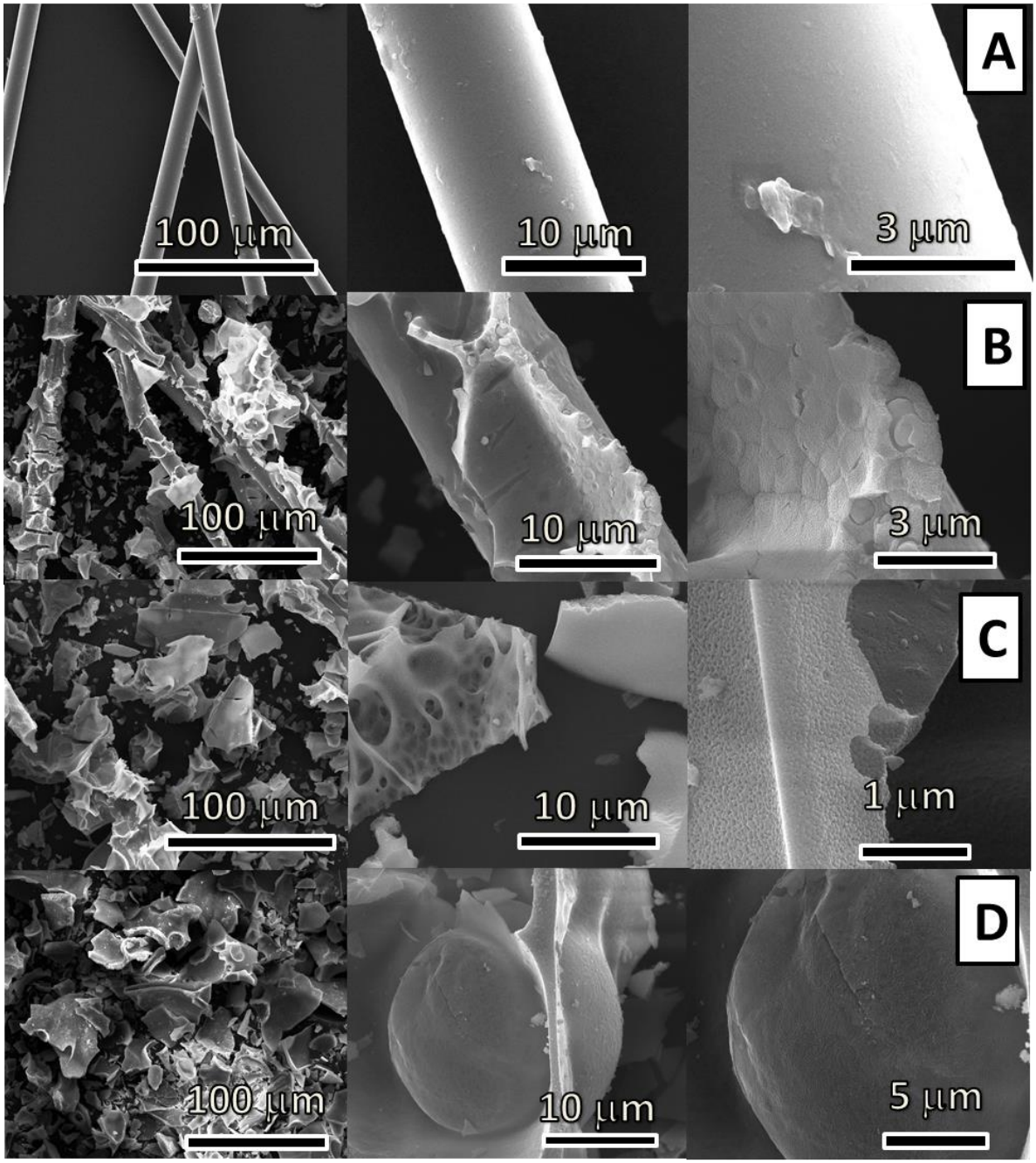

Figure 4.3. SEM micrographs of (A) glass wool as template, glass wool templated samples treated at (B) 800°C and (C) 900°C, (D) powders obtained at 900°C.

To have a better insight of the nanoparticles size and morphology, TEM investigation has been also performed. TEM micrographs of the powder and templated samples acquired at different magnifications are shown in Figure 4.4.

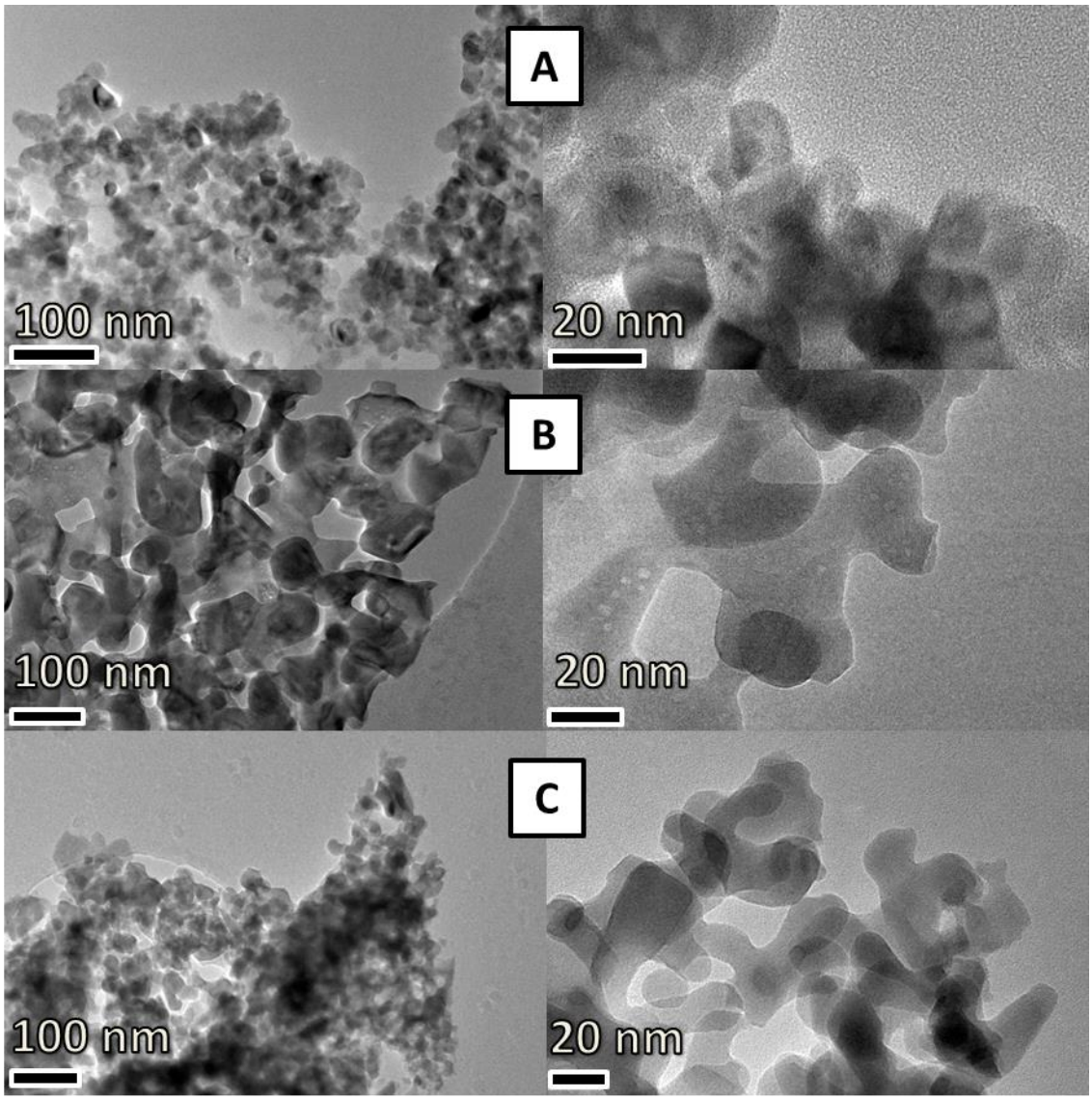

Figure 4.4. TEM micrographs of glass wool templated samples treated at (A) 800°C and (B) 900°C and of (C) powder obtained at 900°C.

The glass wool sample treated at 800°C presents homogeneous clusters of interconnected but not agglomerated nanoparticles but they are not agglomerated and having polygonal shape (15±5nm). TEM confirms the plate-like shape of the nanoparticles both in the powder (45±5 nm) and the templated sample (17±5nm) treated at 900 °C. The particle size distributions are reported in Figure A11 of Appendix 3.

4.1.2. Effect of cerium content in the glass wool nanostructure

Considering the importance of doping agent content on optical properties, in this study the effect of the cerium content on structure and optical properties of Ce:YAG glass wool templated samples has been investigated.

The gel-like starting material prepared with R=1 was used to embed glass wool. Solutions were prepared mixing $YCl_3 \cdot 6H_2O$, $AlCl_3 \cdot 6H_2O$ and $CeNO_3 \cdot 6H_2O$ in ethanol to give different cerium atoms content (0.1, 0.2, 0.5, 1.0 and 2.0 %) with respect to total yttrium plus cerium atoms according to the formula $Ce_xY_{3-x}Al_5O_{12}$. The samples were treated at 800°C and 900°C for 1 hour each. The macroscopic original shape of the template was preserved and yellowish coloration with tonality influenced by the cerium content was obtained.

The WAXS patterns of the templated samples obtained from calcination of GW embedded with precursors are reported in the Figure 4.5.

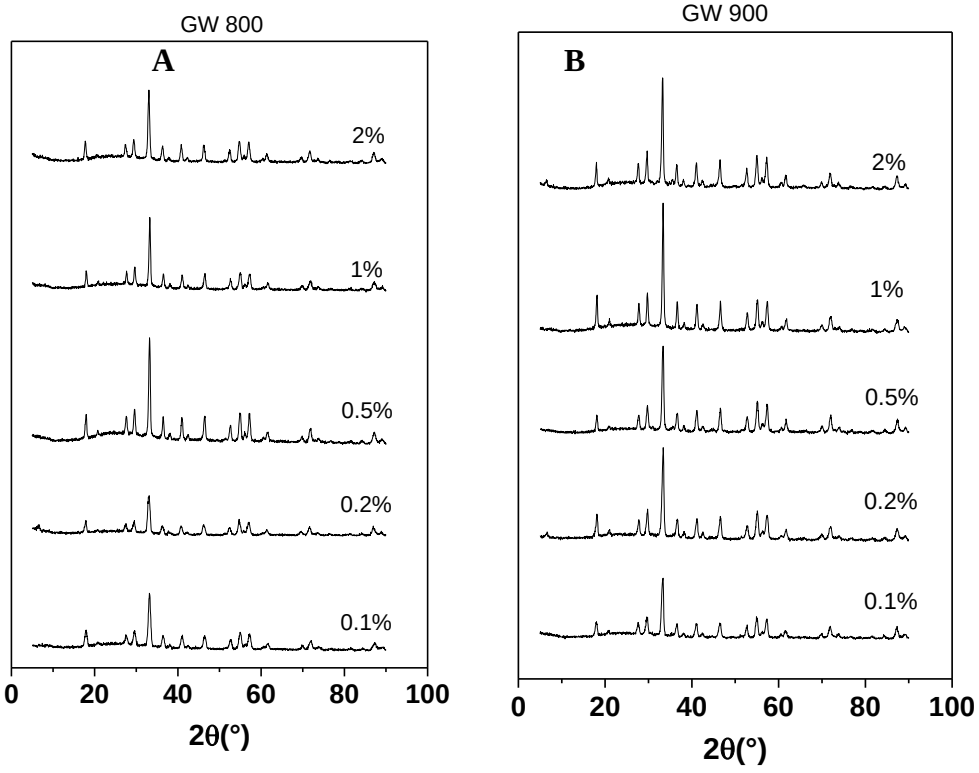

Figure 4.5. WAXS patterns of the GW templated samples obtained by calcination at 800°C (A) and 900°C (B) as function of cerium amount.

For both series, the patterns can be described in terms of YAG phase and an amorphous band. Rietveld method [7] by using the MAUD software [8]. The Rietveld best fit well reproduces the diffraction patterns of each sample. YAG cell parameter, crystallite size and lattice microstrain are reported in Table 4.2.

Table 4.2. YAG cell parameter, the average crystallite size (D), lattice microstrain and amount of amorphous phase (% w/w) obtained by applying the Rietveld method to the WAXS patterns of samples at the different cerium content and treated at 800 and 900 °C.

800 °C				
Ce %	**Cell parameter (Å)**	**D (nm)**	**Microstrain**	**% amorphous**
0.1	a = 12.0521(8)	27(1)	0.0028(2)	29(2)
0.2	a = 12.0957(9)	28(2)	0.0031(1)	20(1)
0.5	a = 12.0570(5)	43(1)	0.00224(7)	40(3)
1	a = 12.0448(6)	44(2)	0.00240(3)	40(2)
2	a = 12.0985(9)	37(1)	0.00256(1)	26(1)
900 °C				
Ce %	**Cell parameter (Å)**	**D (nm)**	**Microstrain**	**% amorphous**
0.1	a = 12.0442(7)	32(1)	0.0021(2)	21(1)
0.2	a = 12.0211(6)	33(1)	0.00221(7)	18(2)
0.5	a = 12.0197(6)	37(1)	0.00161(3)	16(3)
1	a = 12.0139(4)	48(2)	0.00215(8)	27(2)
2	a = 12.041 (6)	74 (1)	0.00213(3)	26(4)

The error is given in parenthesis. ICDD phase codes used: YAG 01-079-1891

The cell parameters of the samples treated at 800 °C are higher that the undoped reference (12.0429 (Å) obtained by using the same method), indicating that the cerium ions have substituted the yttrium ions in the lattice. In the case of samples treated at 900 °C the values are lower than the undoped reference. This finding could be due to

the presence of the amorphous in the WAXS patterns or to a "contamination" of the garnet lattice with the elements coming from the GW.

The IR spectra of the templates are reported in Figure 4.6.

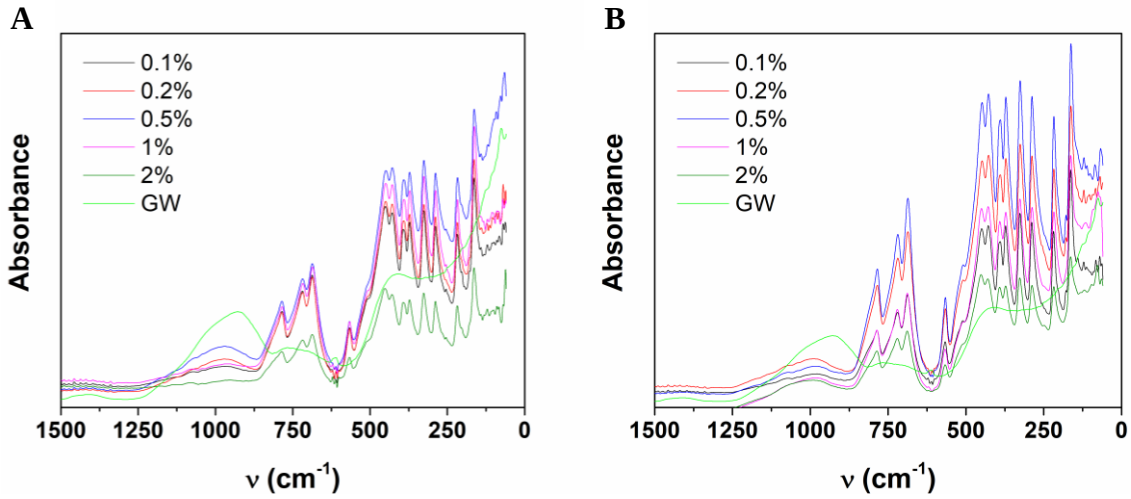

Figure 4.6. IR spectra of the GW templated samples obtained by calcination at 800 °C (A) and 900 °C (B) as function of cerium amount.

The vibration signals of YAG and GW are present in the IR spectra. The IR spectrum of GW shows strong peaks at around 900, 760, and 400 cm^{-1} due to asymmetric, symmetric, and bending modes of SiO_2, respectively, typical of siliceous materials.

The strongest absorption bands for the silica structure in the range between 1000 and 1300 cm^{-1}, are due to asymmetric stretching vibration mode of the bulk Si-O-Si groups, whereas the peaks at 806 and 460 cm^{-1} are due to the symmetric stretching of the Si-O-Si groups and to bending vibrations, respectively. The band at 966 cm^{-1} corresponds to the stretching vibration of Si-O-H surface groups. Finally, the bands at 3461 cm^{-1} and at 1652 cm^{-1} correspond to the O-H stretching ν(O–H) and O-H bending δ(O–H) shift vibration modes, respectively [9,10]. In the GW templated samples, the band at around 1000 cm^{-1} of the GW composed of asymmetric stretching vibration of Si-O-Si and stretching vibration of Si-O-H surface groups is strongly modified, while the contribute of Si-O-H vibration is lost. The observed variation could indicate an

interaction between YAG and GW surface. This effect is stronger in the case of GW templated samples treated at 900 °C.

The YAG peaks are well sharp in the case of the GW templated sample calcined at 900°C, which may indicate an higher degree of ordering of cations, in terms of the lattice positions for these samples. The peaks at about 460, 685, 720 and 790 cm^{-1} are due to the metal-oxygen bonds (Y–O and Al–O) vibrations. For some peaks a shift to higher frequencies is observed in the case of the GW templated samples, indicating a physical interaction between the YAG and the GW.

In order to verify how the cerium content and distribution affects the optical properties of obtained materials, a detailed spectroscopic analysis was performed. The excitation and emission spectra of the GW templates at various cerium content and different temperature are reported in Figure 4.7.

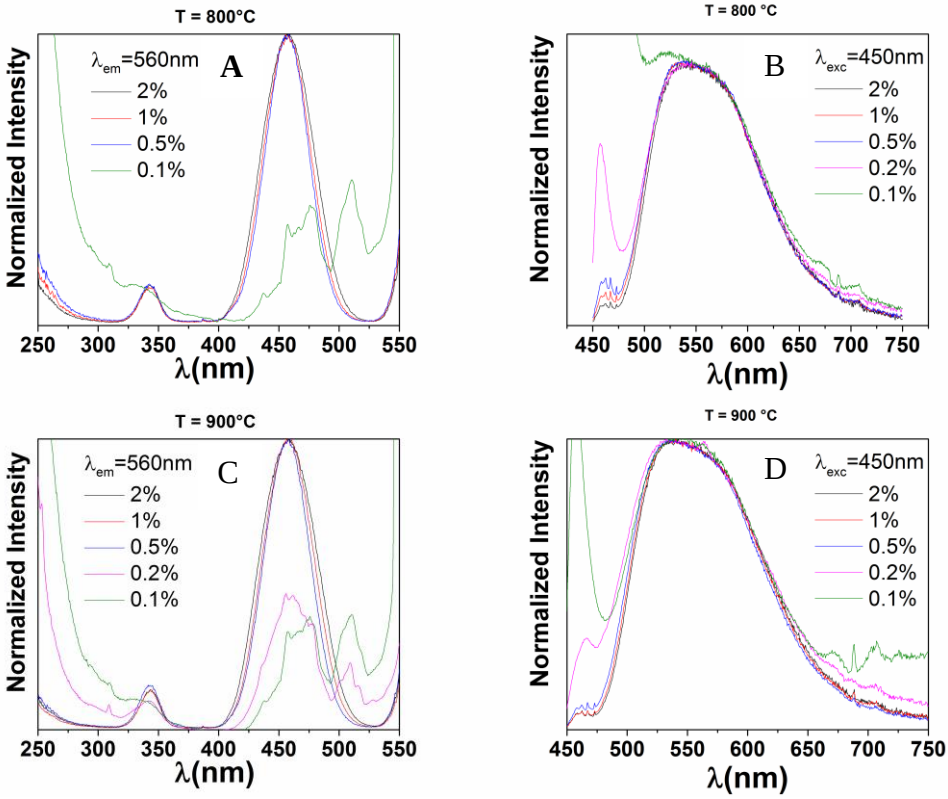

Figure 4.7. Excitation (A- C) and emission (B-D) spectra of the powders at several cerium content treated respectively at 800°C and 900°C.

The excitation spectra of GW templated consist of two characteristic for Ce^{3+} ions absorption bands centred at 340 nm and 460 nm. Slight difference in relative bands' intensities can be found. Particularly, the intensity of 340 nm band slightly decreases in respect to the 460 nm on increasing the cerium content. Emission spectra of obtained materials upon 450 nm excitation reveal the presence of inhomogeneously broadened emission that consists of two bands related with $5d \rightarrow {}^2F_{5/2}$ and $5d \rightarrow {}^2F_{7/2}$ electronic transitions of Ce^{3+} ions. No significant difference can be found in the shape of emission spectra. The quantum efficiency (QE) of the GW templates is reported in Figure 4.8.

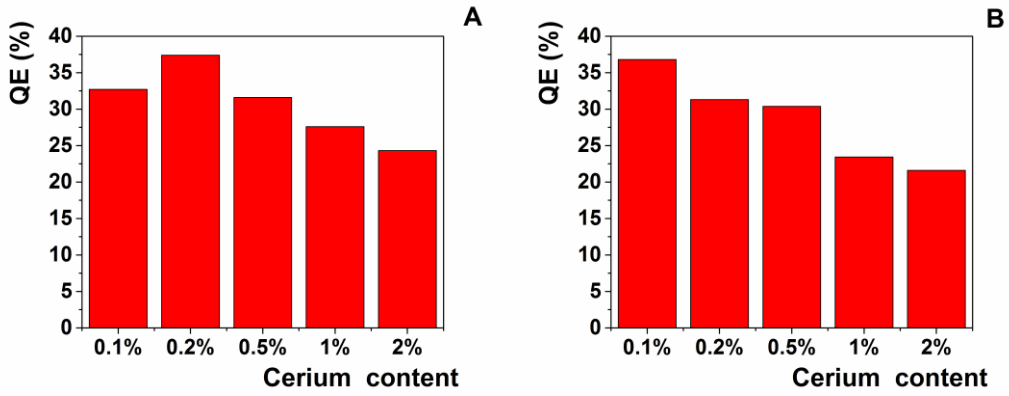

Figure 4.8. Quantum efficiencies of the nanostructure at several cerium content. Sample treated at 800 °C (A) and 900 °C (B).

Considering the two temperature sets, the QE reduced on increasing the cerium content. As already observed, also in this case the trend could be due to the nonradiative depopulation processes of the excited states related with the large amount of the Ce^{3+} ions localized in the strongly defected surface area of the nanoparticle [11,12]. The templates obtained at 800°C are a bit more efficient than 900°C ones, as observed and explained in the previous paragraph.

§ 4.2. Considerations

An unique synthetic pathway for the preparation of Ce:YAG nanostructures has been developed. The synthesis involves the assistance of readily available objects (namely

filter paper, cotton and glass wool) embedded with a suitable gel-like material. The gel-like precursor (a metals/urea complex) ensure the formation of highly pure and crystalline garnet phase, while the template allows to prepare it as well-structured, homogeneous and compact layers of nanoparticles having good optical properties. In addition, hierarchical structure could combine the optical properties with the properties of the original template. Knowing that special glasses have been developed with low dielectric constant to serve in certain radar installations, with high lead content for radiation shielding, and with exceptionally high strength and modulus of elasticity for critical reinforced plastics applications, the unique properties of the luminescent glass wool nanostructure have great potential in applications for large structures including lighting applications combining the strength, chemical durability, fire resistance, and translucency of glass fibres.

The new synthetic pathway is also not expensive, easily scalable for large scale production and open up the way to the preparation of tailored optical devices. In general, the possibility to convert easily adaptable materials (e.g. foldable paper or unrolling glass wool) into organized, still highly functional, doped YAG nanoparticles open up the way to a myriad of possibility to prepare systems that can be easily shaped and then lighted up.

References

[1] A. Djurišić, A. Ng, X. Chen, Prog. Quantum Electron, 34 (2010), 191−259.
[2] O. Paris, G. Fritz-Popovski, D. V. Opdenbosch, C. Zollfrank, Adv. Funct. Mater, 23 (2013), 4408−4422.
[3] W. Gan, S. Xiao, L. Gao, R. Gao, J. Li, X. Zhan, ACS Sustainable Chem. Eng. 5 (2017), 3855−3862.
[4] A. Kool, P. Thakur, B. Bagchi, N. A. Hoque, S. Banerjee, Sukhen, Da, J Am Ceram Soc. 100 (2017), 4836–4847.
[5] S. Glatzel, Z. Schnepp, C. Giordano, Angewandte Chemie, 52 (2013), 2355–2358.
[6] E. Caponetti, D. F. Chillura Martino, M. L. Saladino, C. Leonelli, Langmuir, 23(7) (2007), 3947-3952.
[7] R.A. Young, International Union of Crystallograhy, Oxford University Press: [Chester, England]: Oxford; New York, 1993.

[8] L. Lutterotti, S. Gialanella, Acta Mater. 46 (1) (1998), 101–110
[9] C. Dresler, M.L. Saladino, C. Demirbag, E. Caponetti, D. F. Chillura Martino, R. Alduina, International Biodeterioration & Biodegradation, 125 (2017), 150-156.
[10] B. D. Jamnani, S. Hosseini, A. Shavandi, M. R. Hassan, Maerogel Composites Advances in Materials Science and Engineering (2016) ,2016-11-23.
[11] R. Kasuya, T. Isobe, H.Kuma, J. Katano, Journal of Physical Chemistry B, 109 (2005) (47), 22126-22130.
[12] M. Vorsthove, U. Kynast, Materials Research Bulletin, 46 (11) (2011), 1761-1765.

Conclusions

In this thesis the development and assessment of luminescent composites and nanocomposites based on Ce:YAG phosphors is reported.

The composites and nanocomposites have been investigated focusing to white LED as possible application. The optical properties have been investigated varying methodology of preparation, particles size and dopant quantity.

Two sets of composites have been prepared by using commercial Ce:YAG in PMMA and PC by the melt mixing procedure. Both PMMA and PC composites reveal interesting properties in terms of structure and optical properties. The obtained materials were useful for the color tuning of a blue LED and, most important, two composites allowed to obtaining the white light.

The preparation of Ce:YAG nanocomposites was dependent from the synthesis of nanophosphors. Three non-common and innovative methodology of synthesis have been developed. Each synthesis method allowed obtaining nanophosphors with different features.

Excluding the glycothermal ones, the developed synthetic routes gave good results. The glycothermal synthesis provided nanoparticles with high amounts of secondary phases. The microemulsion assisted synthesis allowed the production of pure garnet nanophosphor with high quantum efficiency. However, big amounts of solvents and surfactants are required for the production of low quantities of powder (yield = 40% in weight), with a consequent increase of the preparation's cost.

The Urea Glass Route (UGR) was the method giving the highest yield (100% in weight) and lower costs. Furthermore, it can be considered eco-friendly, readily available and efforts the possibility to a scaling up. Otherwise, the optical properties are inferior than the ones observed in the nanophosphor from microemulsion assisted synthesis.

Everything considered, the nanocomposites have been prepared by using the best nanophosphor in terms of crystallinity and emission properties synthesized by UGR

at 0.5% of cerium content. The effect of nanocomposites thickness on the effectiveness of white light production has been investigated. Respect to the composites obtained by using the commercial powders, the more adequate nanocomposite is thinner, with an overall production costs containment.

These findings provide new way for companies based on green procedures, low cost and energy efficiency technologies which promote technological transfer and sustainable development.

Since the UGR synthesis gave the possibility to obtain a gel-like starting materials, it was used to prepare hierarchical Ce:YAG nanostructures. The synthetic pathway is not expensive, easily scalable for large scale production and open up the way to the preparation of tailored optical devices. In particular, the glass wool was the best material used as support allowing to the production of a multifunctional material with moldable shape and potential lighting application for large structures combining the strength, chemical durability, fire resistance, and translucency of glass fibres.

A1. Materials

Composites preparation

Ce:YAG powder, with a density of 4.8 g cm^{-3}, was supplied by Dogtai Tianyuan Fluorescent Materials, China.

Commercial grade PMMA (Altuglas® V920T), in pellet form, having a melt flow rate of 1g/10 min at 230 °C/3.8 kg, M_w = 110 000 g mol^{-1}, produced by Altuglas International (France).

Commercial grade bisphenol-A polycarbonate (Makrolon® 2407), having a melt flow rate of 20 g/10 min (300 °C/1.2 kg), was supplied in pellet form by Bayer Material Science, Germany.

Nanophosphors preparation

Glicotermal synthesis: Yttrium acetate hydrate $Y(CH_3CO_2)_3 \cdot xH_2O$ (Sigma-Aldrich ≥99.9%), aluminum isopropoxide $Al(OCH(CH_3)_2)_3$ (Sigma-Aldrich ≥98%) and 99.99% pure cerium acetate hydrate $Ce(CH_3CO_2)_3 \cdot xH_2O$ (Sigma-Aldrich, 99,99%). 1,4-butanediol (Sigma-Aldrich ≥99.9%).

Microemulsion assisted synthesis: Cetyltrimethylammonium bromide (CTAB) (Aldrich ≥98%), 1-butanol (Aldrich, 99,8 %), n-heptane (Sigma-Aldrich, 99%), deionized water, $Y(NO_3)_3 \cdot 6H_2O$ (Sigma-Aldrich, 99,8%), $Al(NO_3)_3 \cdot 9H_2O$ (Sigma-Aldrich, 99,8%) and ammonia solution (Sigma-Aldrich 28%) were used as received. The conductance of deionized water was < 1.5 µS/m.

UGR: $YCl_3 \cdot 6H_2O$ (Aldrich, 99.9%), $AlCl_3$ (Aldrich, 98%), $CeCl_3 \cdot 7H_2O$ (Aldrich, 99.99%) Urea (Acros Organics, 98%), ethanol (Aldrich, 99.98%).

Nanocomposites preparation

PMMA (MW: 120,000 g mol^{-1}, supplied by Aldrich)

A2. Characterization techniques

- **Wide Angle X-Ray Scattering (WAXS)** patterns were acquired by a Philips PW 1050/39 diffractometer in the Bragg-Brentano geometry using Ni-filtered Cu Kα radiation (λ = 1.54056 Å) in the 2θ range 5-90° with a step of 0.05° and a time for step of 5 sec. The X-ray generator worked at power of 40 kV and 30 mA, and the resolution of the instrument (divergent and antiscatter slits of 0.5°) was determined using R-SiO_2 and R-Al_2O_3 standards free from the effect of reduced crystallite size and lattice defects. The phase identification has been performed by using the X'pert HighScore® Software.

  During the period in London the patterns were recorded with a Panalytical Empyrean Diffractometer (Cu Kα radiation, λ = 0.154 nm).

- **Small Angle X-Ray Scattering (SAXS)** measurements were performed with Bruker AXS Nanostar-U spectrometer using a Cu rotating anode working at 40 kV and 18 mA as the source. The X-ray beam was monochromatized at a wavelength λ of 1.54 Å using a pair of Göbel mirrors and was collimated using a series of three pinholes with diameters of 500, 150 and 500 µm. Samples were introduced in glass capillaries of 2 mm diameter and directly mounted on the sample stage to avoid additional scattering of the holder. Samples temperature was 25.0 °C for all the measurements.

  Data were collected for 5000 seconds, in a two-dimensional multiwire proportional counter detector placed at 105 cm from the sample. Q values ($0.08 < Q < 0.20$) were calculated from scattering angles, θ:

$$Q = \frac{4\pi sen\theta}{\lambda}$$

  Since all the diffraction patterns were isotropic, a radial integration was performed and the obtained intensities were subsequently corrected for the transmittance of the sample and contribution of the empty capillary.

- **Scanning Electron Microscopy (SEM)** were acquired on a FEI inspect F instrument. The samples were loaded on carbon coated stubs and coated by sputtering an Au alloy prior to imaging.

- **Transmission Electron Microscopy (TEM)** micrographs were acquired by using a JEM-2100 (JEOL, Japan) operating at 200 kV accelerating voltage, equipped with an energy dispersive X-ray spectrometer (EDS, Oxford, UK) suitable for element identification. Each powder was homogeneously dispersed in isopropanol by sonication. A small drop was deposited on a lacey-carbon grid of 300 mesh, and after complete solvent evaporation the nickel-copper grid was introduced into the TEM chamber analysis. For the observation of the composites, 100 nm thick slices were prepared by using a Leica EM UC6 ultra-microtome, and were put onto a 3 mm Cu grid 'lacey carbon' for analysis. The Selected Area Electron Diffraction (SAED) pattern was collected by using a CCD camera (Gatan MSC KAF1000).
- **Nuclear Magnetic Resonance Spectroscopy (NMR)** The ^{13}C {^{1}H} CP-MAS NMR spectra were obtained at room temperature using a Bruker Avance II 400 MHz (9.4T) spectrometer operating at 100.63 MHz for the ^{13}C nucleus with a MAS rate of 10 kHz, 400 scans, a contact time of 1.5 μs, and a repetition delay of 2 s. The optimization of the Hartmann-Hahn condition was obtained using an adamantane sample. Each sample was placed in a 4 mm zirconia rotor with KEL-F caps using silica as filler to avoid inhomogeneities inside the rotor. The proton spin–lattice relaxation time in the rotating frame $T_{1\rho}(H)$ was indirectly determined, with the variable spin lock (VSL) pulse sequence, by the carbon nucleus observation using a 90°-τ-spin-lock pulse sequence prior to cross polarization with a delay time τ ranging from 0.01 to 3 s. The ^{13}C spin–lattice relaxation time in the rotating frame $T_{1\rho}(C)$ was determined, with the variable spin lock (VSL) pulse sequence, applying the spin-lock pulse after the cross-polarization on the carbon channel. The data acquisition was performed by ^{1}H decoupling with a spin lock pulse length, τ, ranging from 0.4 to 30 ms and a contact time of 1.5 ms.
- **Thermogravimetry and Differential Thermal Analysis (TGA)** was performed with a Q500 TA instrument under an air flow of 60 cm^3 min^{-1} for the sample and a nitrogen flow of 40 cm^3 min^{-1} for the balance. The weight of each sample was ca. 40 mg. The measurements were carried out by heating the sample from room temperature to 900°C at a rate of 6°C min^{-1}.

- **Porosimetry** *N_2 absorption-desorption isotherms* were registered at 77 K using a Quantachrome Nova 2200 Multi-Station High Speed Gas Sorption Analyser. Samples were outgassed for 12 hrs at room temperature in the degas station. Adsorbed nitrogen volumes were normalized to the standard temperature and pressure. The specific surface area (S_{BET}) was calculated according to the standard BET method in the relative absorption pressure (P/P_0) range from 0.045 to 0.250.
- **Infrared Spectroscopy (IR)** *ATR Infrared Spectra* were acquired between 600 and 4000 cm^{-1} by using a Perkin Elmer Spectrum 65 Spectrometer equipped with an attenuated total reflection (ATR) setup.
- **Luminescence Spectroscopy:**
    - **Emission and excitation spectra** of the Ce:YAG-PC and Ce:YAG-PMMA composites were measured using a Fluoromax 4 HORIBA Jobin Yvon spectrofluometer. Samples, placed at 45°, were excited by an Xe source operating at 150 W. The Ce:YAG-PC composites were excited with a wavelength of 450 nm for emission measurement and 550 nm for excitation measurements.
    - **Emission and excitation spectra** of the nanophosphors were measured using the FLS980 Fluorescence Spectrometer from Edinburgh Instruments equipped with 450 W Xenon lamp. Both the excitation and emission 300 mm focal length monochromators were in Czerny Turner configuration. Excitation arm was supplied with holographic grating of 1800 lines/mm, blazed at 250nm, while the emission spectra was supplied with ruled grating, 1800 lines/mm blazed at 500nm. The spectral resolution was 0.1 nm. The R928P side window photomultiplier tube from Hamamatsu was used as a detector.
    - **Quantum efficiency** of luminescence was measured using the same equipment supplied with 30 cm in diameter integrating sphere.
    - **The lifetimes measurements** were carried on a femtosecond laser setup composed of a Coherent Libra-S all-in-one ultrafast oscillator and regenerative amplifier laser system, with pulse duration less than 100 fs at

1 kHz repetition rate, a Coherent OPerA-Solo optical parametric amplifier and a Hamamatsu C5677 streak camera with time resolution of 14 ps.

- **Emission Spectroscopy** of the Ce:YAG-PC and Ce:YAG-PMMA composites and Ce:YAG-PMMA nanocomposites combined with a blue LED (InGaN, Quantum Light technology, Voltage 3.2V, Current 350mA) were performed by using an Ocean USB2000+ spectrometer operating in the wavelength range 200-1100 nm. The chromaticity coordinates were calculated from the emission spectra following the standard CIE 15:2004.
- **Viscosimetry** measurement were performed by using three Ubbelohde (Schott) viscometers with capillary diameter appropriate for the different viscosity range. Relative viscosity was calculated with respect to cinematic viscosity as stated in the following equation:

$$\eta_r = \frac{\eta_{sample}}{\eta_{water}}$$

where η_r is the relative viscosity and η_{sample} and η_{water} are the cinematic viscosities of the sample and of the pure water, respectively.

- **Electrical conductivity** measurements were performed with an Amel 160 conductimeter. The microemulsions were kept under agitation with a magnetic stirrer.

A3. Graphs and tables

Table A1 SAXS fit parameters according to eq. 8. Results obtained considering the hard sphere potential for ellipsoidal object and critical scattering.

Sample	r	nu	eta	rhs	fi	Io	ξ
R4.3 NO3	20.61 (9)	0.359 (6)	0.0020593 (1)	21.42 (2)	0.1278 (6)	618 (65)	165 (10)
R10 NO3	25.49 (3)	0.431 (1)	0.0014566 (7)	27.36 (3)	0.0959 (2)	1700 (240)	214 (18)
R20 NO3	34.32 (1)	0.5063 (5)	0.0008583 (5)	39.46 (2)	0.1024 (2)	3868 (25)	180 (8)
R30 NO3	41.65 (2)	0.549 (3)	0.0006250 (7)	51.69 (1)	0.12987 (9)	6520 (30)	99.9 (1)
R4.3NH3	20.0 (1)	0.381 (8)	0.002239 (1)	21.64 (2)	0.1311 (7)	2430 (25)	302 (3)

The error on the last digit is given in parenthesis.
R is the radius of rotational axes, nu ratio between radius of the semi-principle axes and equatorial axis, eta is the scattering length density difference between ellipsoid and matrix, rhs is the hard potential radius, fi is the volume fraction and Io and ξ are the Ornstein Zernike parameters.

Table A2 SAXS fit parameters according to eq. 13. With ξ, d and fa calculated from eqs. 10, 11 and 12.

Sample	A ·10^{-6}	L ·10^{-3}	$<\varepsilon^2>$ ·10^{-2}	D ·10^{-6}	I	E	ξ	d	fa
R4.3NH3	356(8)	-19.78(9)	6.6(2)	42.3(9)	0.0184(5)	15(6)	14.928	52.374	-0.524
R10NH3	102(2)	-6.1(1)	8.2(1)	3(5)	0.042(3)	48(5)	16.879	77.482	-0.304
R20NH3	29.7(3)	-4.43(8)	7.09(9)	170(20)	0.30(3)	52(5)	24.866	101.466	-0.406
R30NH3	10.86(6)	-3.44(3)	6.47(5)	1.30(10)	0.42(3)	51(5)	35.625	125.401	-0.522
R40NH3	5.41(3)	-2.88(1)	6.00(4)	77(9)	0.53(4)	28(6)	47.540	144.736	-0.619
R46NH3	4.09(3)	-3.96(1)	1.41(5)	920(70)	7.8(5)	283(46)	219.967	140.396	-0.980
R49NH3	4.01(2)	-3.94(1)	2.42(6)	1170(90)	13.5(9)	567(74)	248.461	140.889	-0.984
R57NH3	3.15(2)	-3.488(9)	1.57(4)	850(50)	10.0(6)	481(52)	256.912	149.726	-0.983
R68NH3	2.254(6)	-2.446(5)	5.57(4)	170(10)	1.7(1)	61(11)	84.763	170.148	-0.815

Sample	A ·10^{-6}	L ·10^{-3}	$<\varepsilon^2>$ ·10^{-2}	D ·10^{-6}	I	E	ξ	d	fa
R10NO3	128(2)	-9.32(8)	7.6(1)	32.5(3)	0.021(1)	38(4)	17.312	70.230	-0.411
R20NO3	32.1(3)	-6.54(6)	7.48(9)	240(4)	0.28(4)	43(6)	28.919	93.951	-0.578
R30NO3	12.72(6)	-4.99(2)	6.17(5)	299(5)	0.41(6)	29(5)	43.189	114.093	-0.699
R40NO3	5.85(2)	-3.63(1)	6.08(5)	375(6)	0.7(1)	29(7)	57.544	136.498	-0.750
R46NO3	3.97(1)	-3.035(7)	6.18(4)	322(5)	0.7(1)	26(8)	64.836	149.882	-0.761
R49NO3	3.739(7)	-3.005(4)	6.66(3)	236(4)	0.42(7)	1(6)	68.112	151.506	-0.777
R49NO3	3.739(7)	-3.005(4)	6.66(3)	236(4)	0.42(7)	1(6)	68.112	151.506	-0.777
R57NO3	2.501(3)	-2.508(2)	6.76(2)	364(7)	0.51(9)	-11(7)	78.176	166.782	-0.793
R70NO3	1.504(2)	-1.957(2)	9.05(2)	9.23(6)	0.04(3)	-80(9)	89.891	189.138	-0.798

The error on the last digit is given in parenthesis.

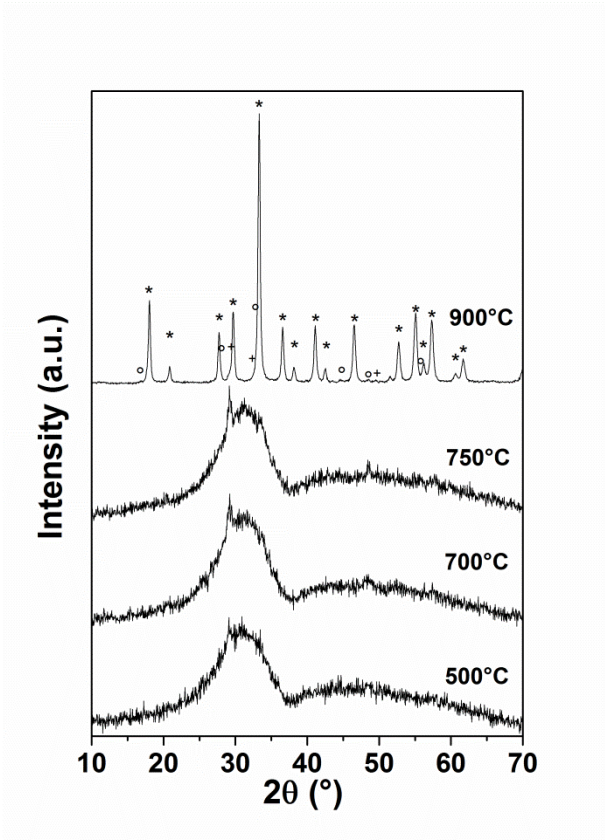

Figure A1. WAXS patterns of the samples thermal treated at 500, 700, 750 and 900°C. YAG *, YAH ° and Yttria +

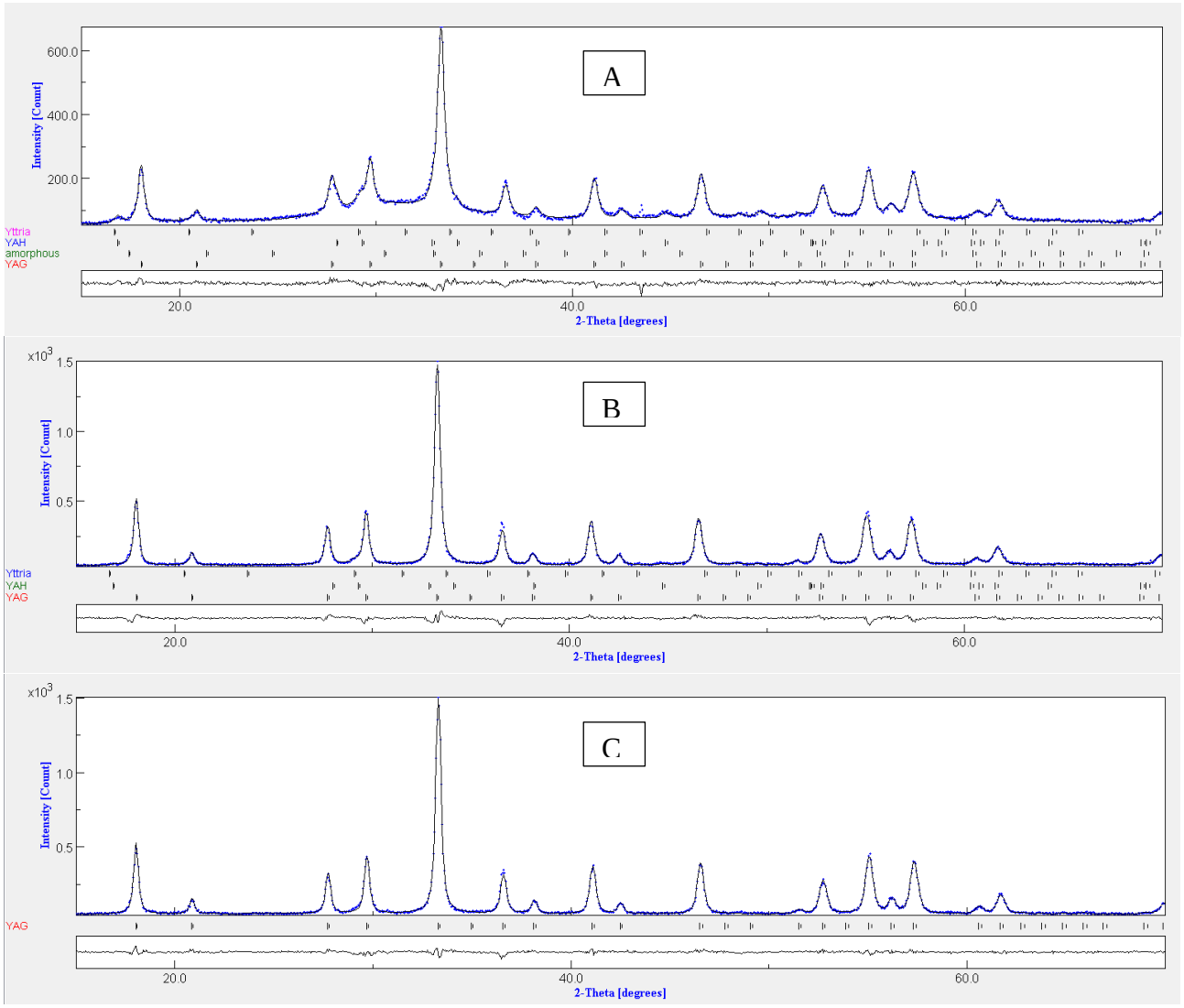

Figure A2. WAXS patterns (dots) and the Rietveld fits (full lines) of the samples treated at 850°C (A), 900°C (B) and 950°C (C). Bar sequences of YAG and YAH and Yttria reference diffraction patterns and residual plot are shown along the bottom.

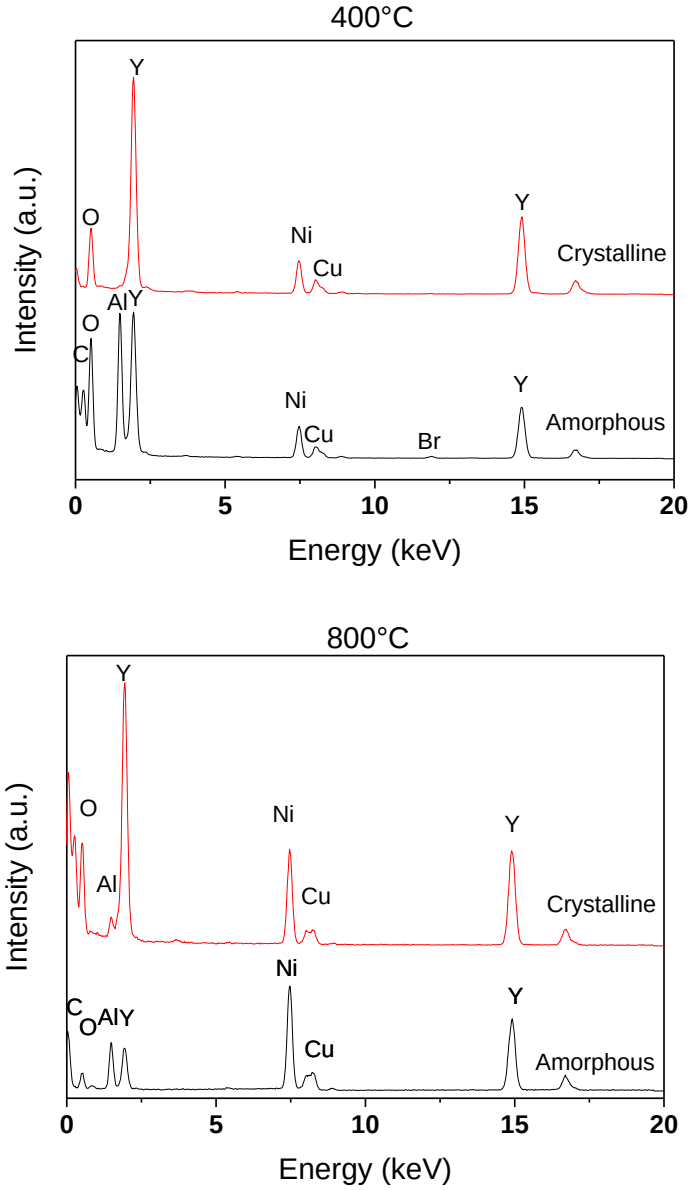

Figure A3. EDS spectra of amorphous agglomerates (black) and of crystalline hedgehogs (red) observed in the samples treated at 400 and 800°C.

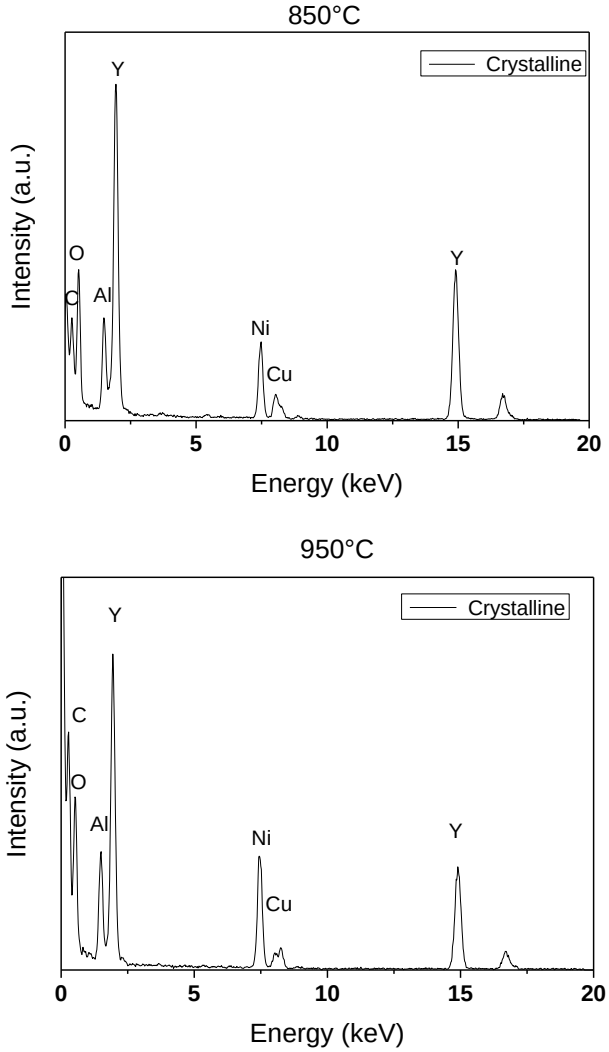

Figure A4. EDS spectra of the particles observed in the samples treated at 850 and 950°C.

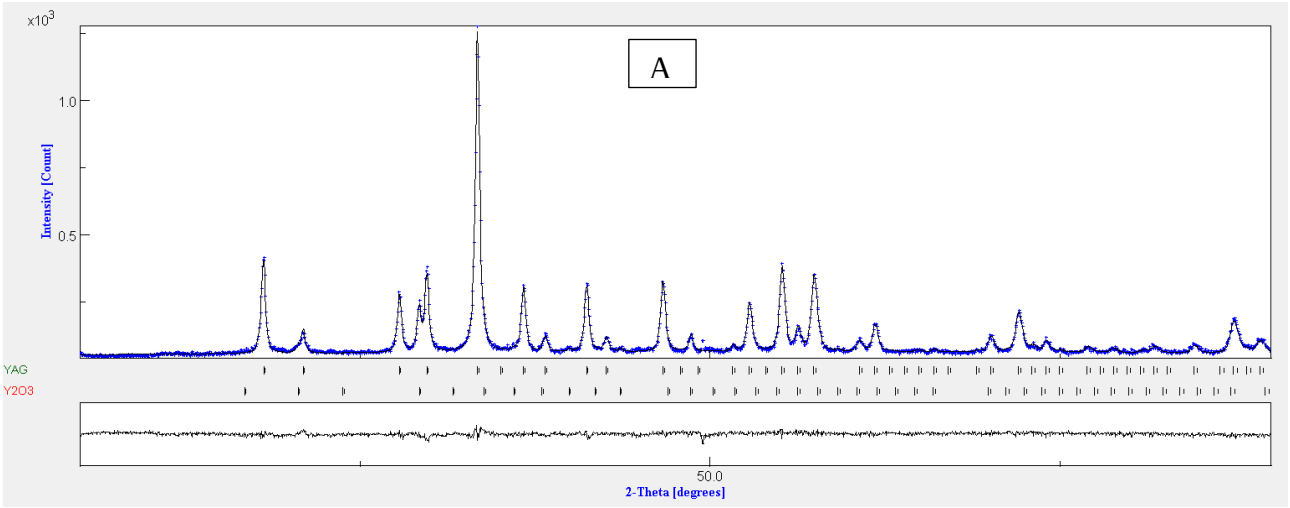

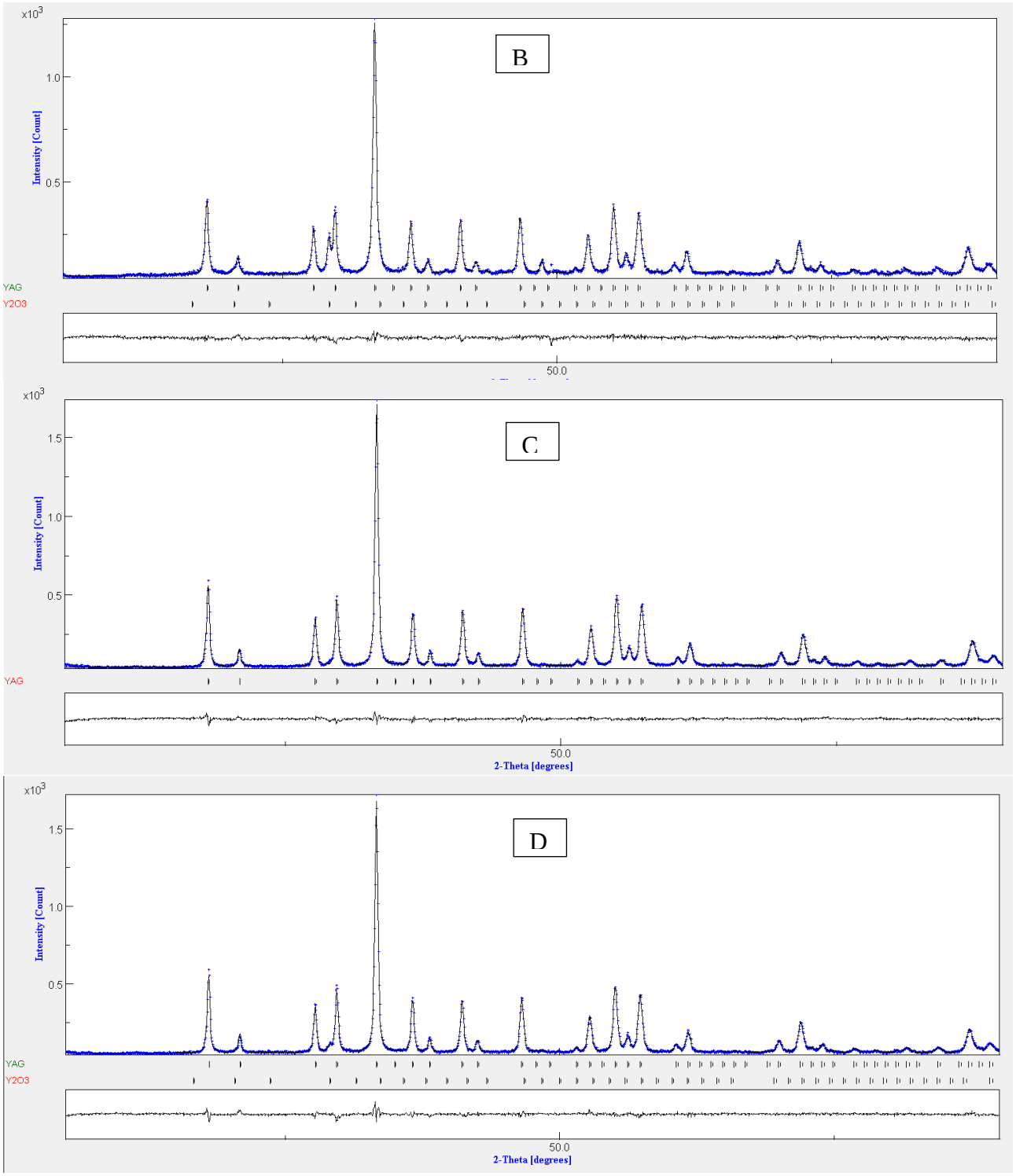
B
C
D
x10^3
Intensity [Count]
YAG
Y2O3
50.0
2-Theta [degrees]

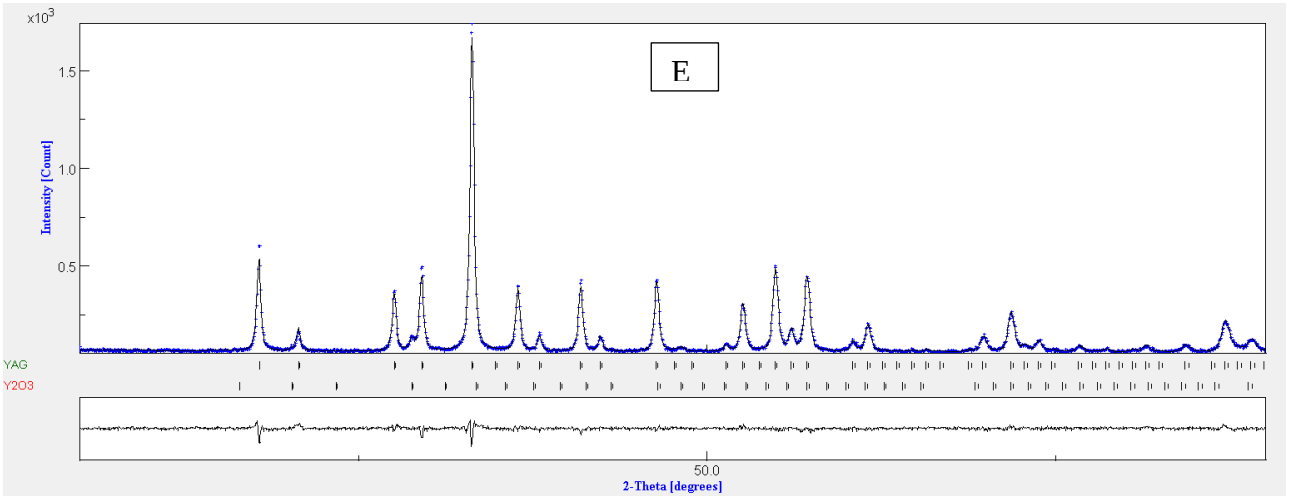

Figure A5. WAXS patterns (dots) and the Rietveld fits (full lines) of the samples doped at 0.1, 0.2, 0.5, 1, 2% respectively (A, B, C, D, E). Bar sequences of YAG and Yttria reference diffraction patterns and residual plot are shown along the bottom.

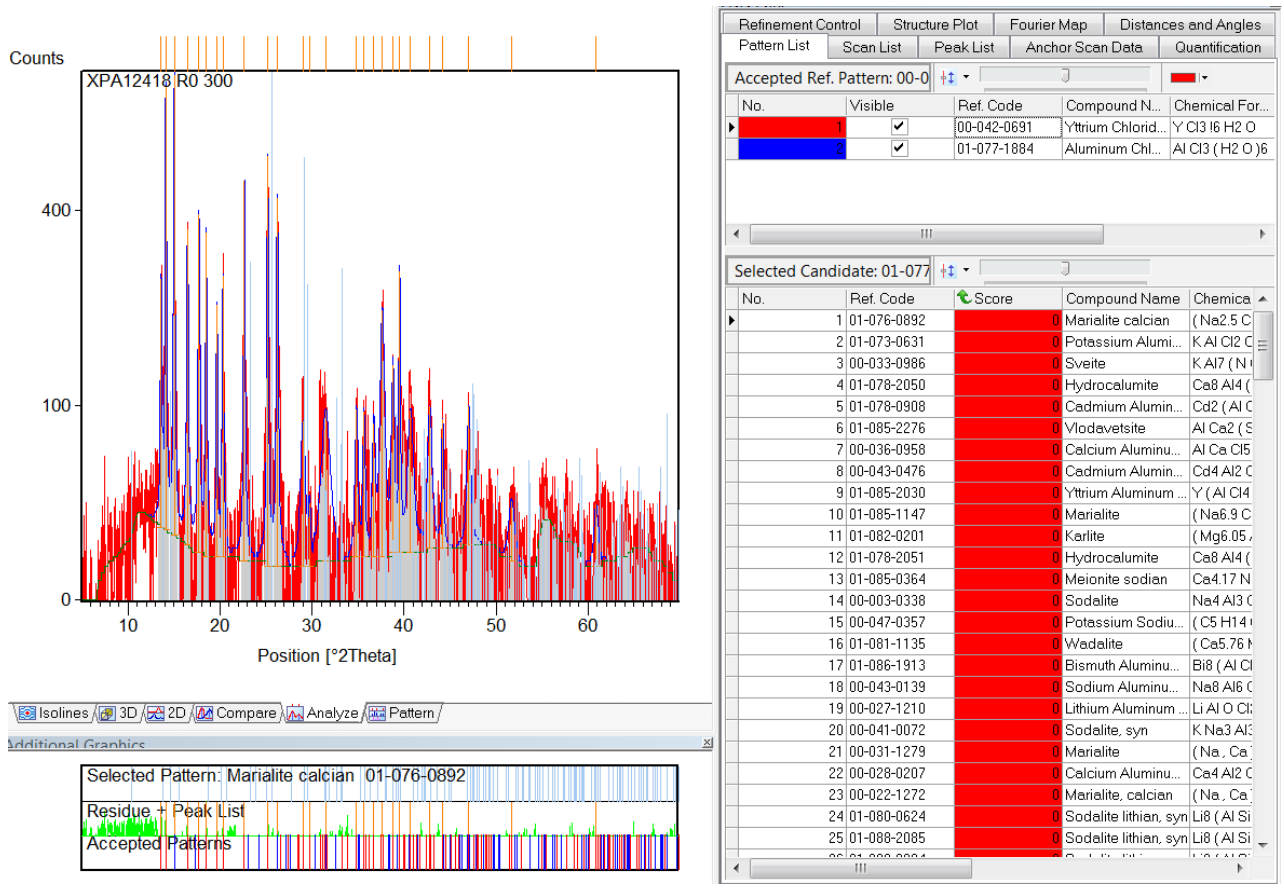

Figure A6. WAXS pattern of the sample prepared without addition of urea (R0) and treating at 300°C (R0). YCl_3 $6H_2O$ and $AlCl_3$ has been identified.

Figure A7. Photos of the glass wool before (left) and after (right) calcination at 800°C.

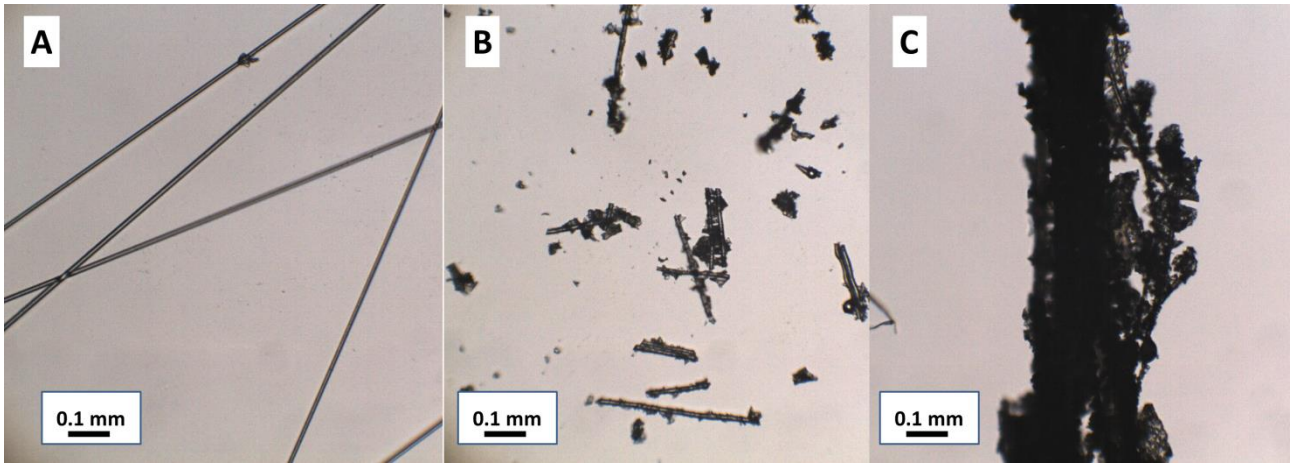

Figure A8. Optical microscope images of (A) glass wool and glass wool template samples obtained at (B) 800°C and (C) 900°C

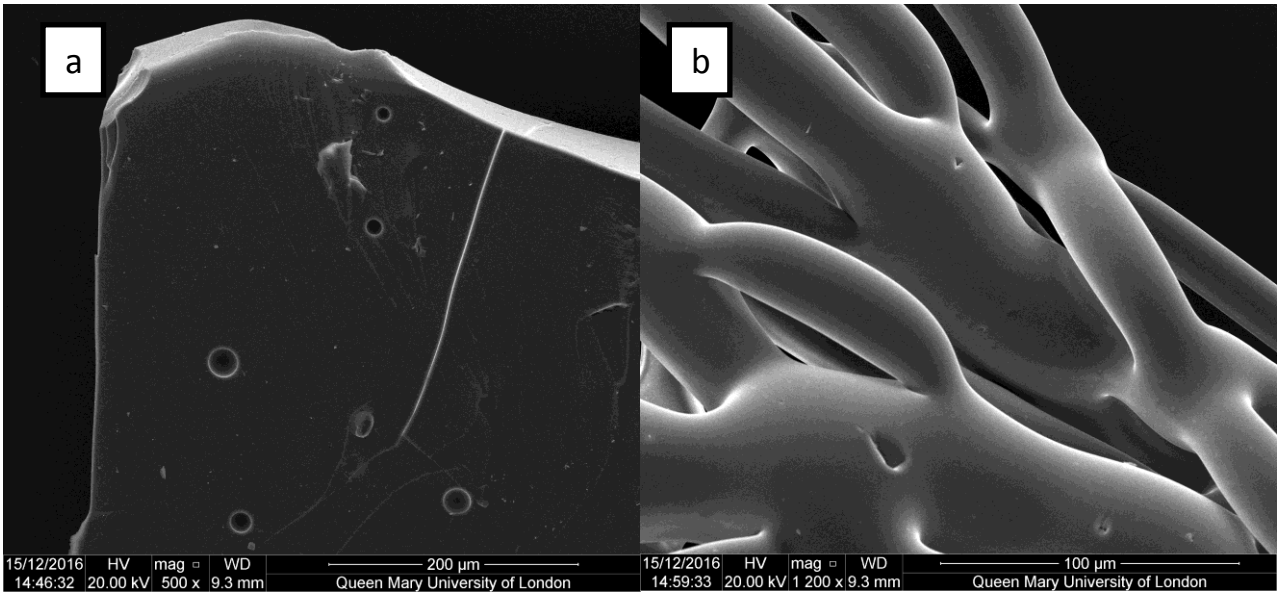

Figure A9. SEM micrographs of glass wool calcined at 800°C.

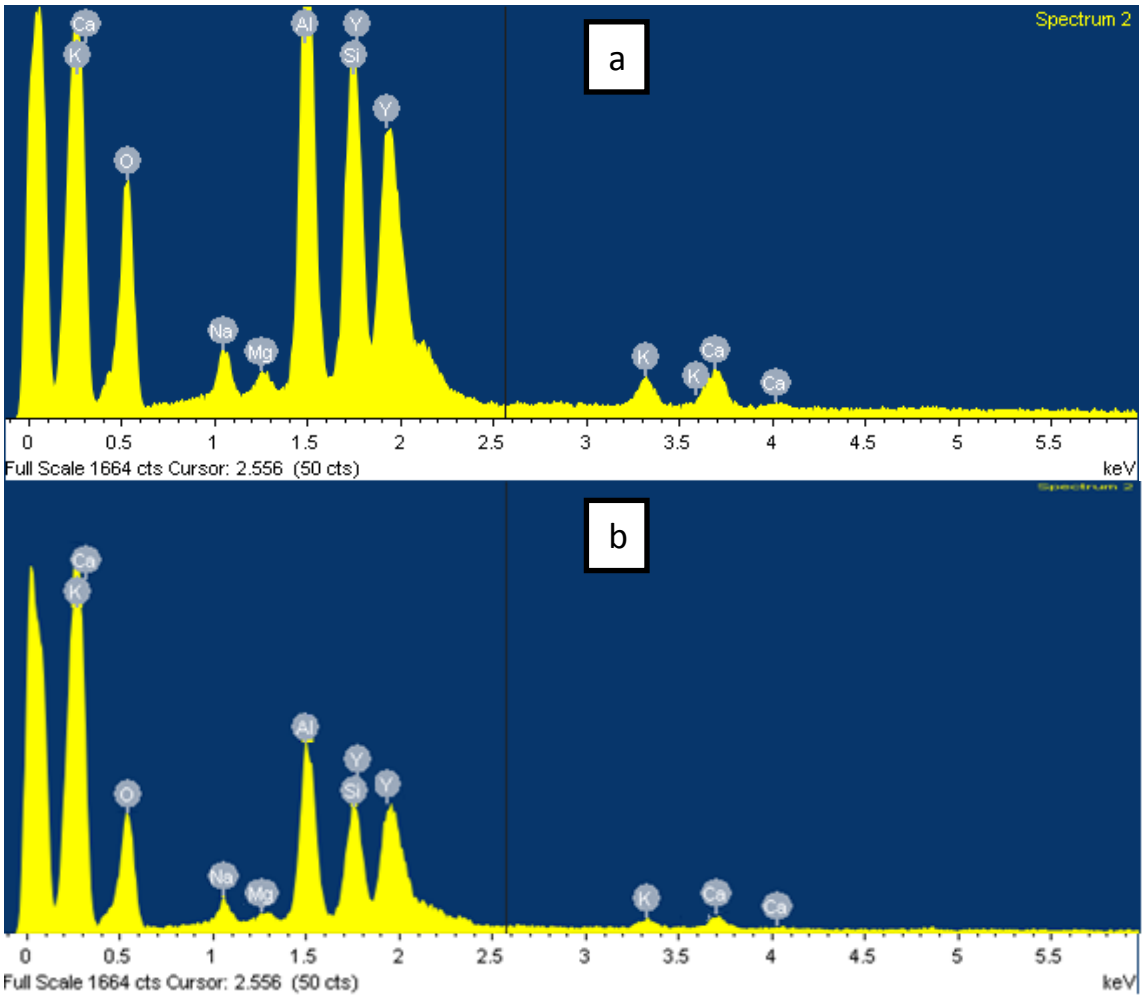

Figure A10. EDS spectra of the particles observed during SEM measurements of glass wool template samples obtained at (A) 800°C and (B) 900°C

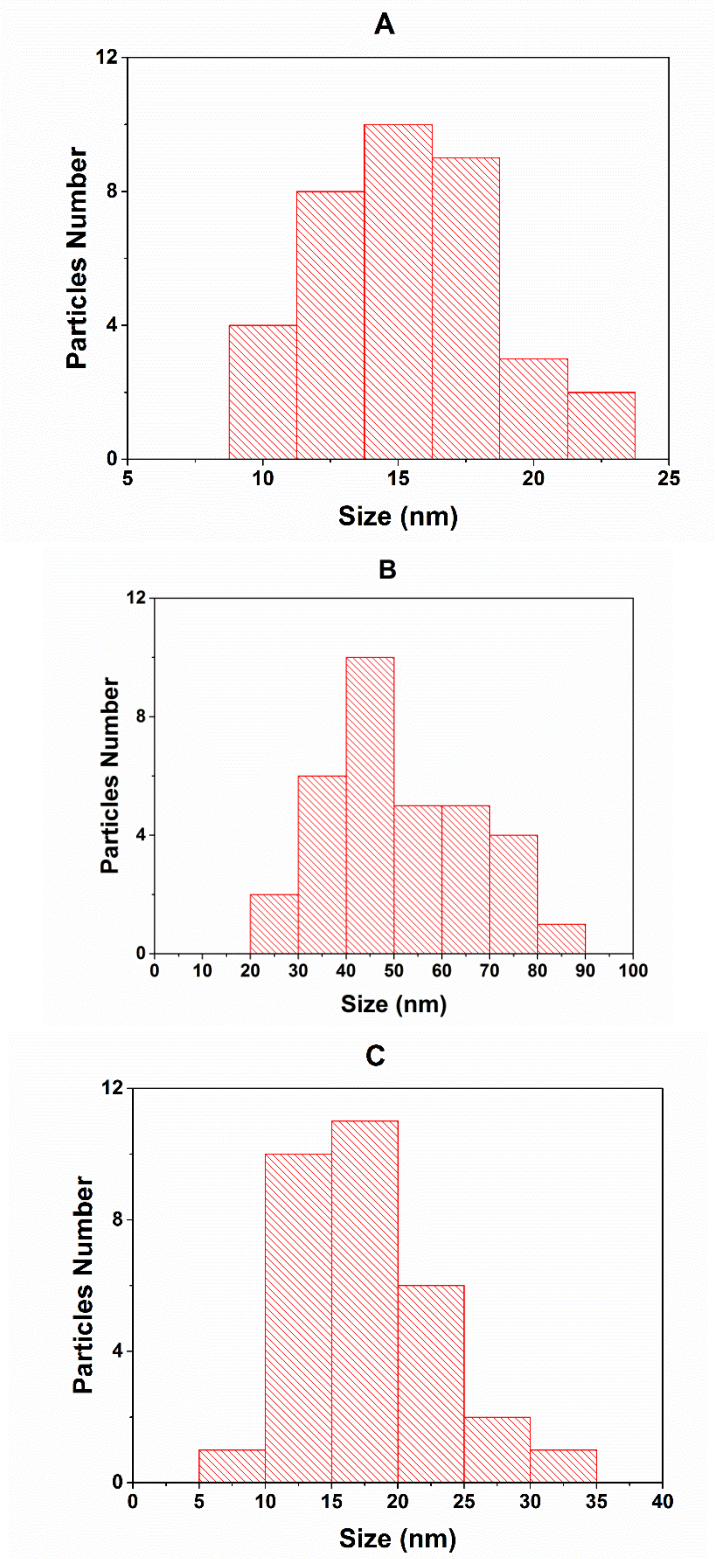

Figure A11. Particle size distribution obtained from TEM micrographs of glass wool template samples obtained at (A) 800°C and (B) 900°C and of powder obtained at 900°C.

A4. Activity of Francesco Armetta

Formation

Erasmus plus "Joint innovative training and teaching/learning program in enchancing developmentand transfer knowledge of application of ionizing radiation in materials processing". *Universite de Reims Champagne - Ardenne (France* 23/09/2016 - 15/09/16*) and Kaunas University of Technology (Lithuania* 03/10/16 - 08/10/16*)*

English course "Academic Writing and oral skills for PHD Students" "Università degli Studi di Palermo"

Training course on Ionizing Radiations Physics and Radioprotection "Università degli Studi di Palermo"

Mentoring at Università degli Studi di Palermo

20 hours mentoring for first year students of Biology and Biotechnology degree courses
200 hours mentoring for student which have to study Chemistry.

Member of organization committee of:

Arte è Scienza. Palermo, 3-4 December 2016. *La diagnostica come mezzo di approfondimento della conoscenza dell'opera d'arte - l'opera d'arte come mezzo di divulgazione della cultura scientifica*. a cura di E. Caponetti, D. Chillura Martino, M.L. Saladino, S. Bastone, V. Renda, F. Armetta, G. Chirco, S. Ridolfi

Mirabilia Maris. Tesori dai Mari di Sicilia, 27 Frebruary 2017. *Il contributo delle indagini chimico-fisiche*. a cura di E. Caponetti, F. Armetta, D. Chillura Martino, M.L. Saladino, S. Bastone, V. Renda, G. Chirco.

Archmat Summer School 2017, 20-26 July 2017. *Archaeometry and Underwater Archaeology*. a cura di E. Caponetti,. D.F. Chillura Martino, F. Armetta, S. Bastone, R. Pitonzo, G. Nasillo, V. Renda, M.L. Saladino, A. Spinella, F. Sammartino.

Arte è Scienza. Palermo, 3 December 2017. *L'affresco "Trionfo della morte" Oltre l'approccio visivo*. a cura di E. Caponetti, D. Chillura Martino, M.L. Saladino, S. Bastone, V. Renda, F. Armetta, G. Chirco

Research visiting:

1. Institute of Low Temperature and Structure Research Polish Academy of Sciences in Wrocław (Polonia), for luminescent investigation on the Ce:YAG nanophosphors (31/05/2015 - 07/06/2017).
2. Departnment of Chemistry and Biochemistry della Queen Mary University in London (Regno Unito) to developed the Urea Glass Route for the Ce:YAG nanophosphor and hierarchical nanostructure synthesis and to characterize the products structure (23/09/2016 - 24/12/2016).

3. Institut für Chemie, Technische Universität Berlin, Berlin, Germania, to set up the Urea Glass Route for the Ce:YAG nanophosphor (05/07/2015 - 11/07/2015).

Patents

Patent request N. 102016000029804 filed for Italy in 22/03/2016.
"Composizione per la deacidificazione e la riduzione della carta e relativo metodo per il restauro della carta" Eugenio Caponetti, Delia Francesca Chillura Martino, Stella Bastone, Maria Luisa Saladino, Francesco Armetta.

List of Publications

P1. E. Caponetti, **F. Armetta***, L. Brusca, M. Delia Chillura, M. L. Saladino, S. Ridolfi, G. Chirco, M. Berrettoni, P. Conti, B. Nicolò, S. Tusa "*A multivariate approach to the study of orichalcum ingots from the underwater Gela's archaeological site*" Microchemical Journal, 135 (2017).

P2. **F. Armetta**, M.L. Saladino, D. Chillura Martino, P. Livreri, M. Berrettoni, E. Caponetti, "*Synthesis of Yttrium Aluminum Garnet nanoparticles in confined environment II: role of the thermal treatment on the composition and microstructural evolution*" J. of Alloy and Comp (2017)

P3. E. Caponetti, **F. Armetta**, M. Delia Chillura, M. L. Saladino, S. Ridolfi, G. Chirco, M. Berrettoni, P. Conti, B. Nicolò, S. Tusa, "*First discovery of orichalcum ingots from the remains of a 6th century bc shipwreck near Gela (Sicily) seabed*" Mediterranean Archaeology and Archaeometry, 17 2 (2017).

P4. **F. Armetta**, D. F. Chillura Martino, R. Lombardo, M. L. Saladino, M. Berrettoni, E. Caponetti, " *Synthesis of yttrium aluminum garnet nanoparticles in confined environment, and their characterization*" Colloids and Surfaces A: Physicochemical and Engineering Aspects 511 (2016) 82-90

P5. **F. Armetta**, M. Sibeko, A. S. Luyt, D. F. Chillura Martino, A. Spinella, M. L. Saladino, "*Influence of the Ce:YAG amount on structure and optical properties of Ce:YAG-PMMA composites for white LED"* Zeitschrift für Physikalische Chemie 230(9) (2016) 1219–1231

P6. M. L. Saladino, **F. Armetta**, M. Sibeko, A. S. Luyt, D. F. Chillura Martino, E. Caponetti, "*Preparation and characterisation of Ce:YAG -polycarbonate composites for white LED"* Journal of Alloys and Compounds 664 (2016) 726–731

P7. M. Russo, **F. Armetta**, S. Riela, D. Chillura Martino, P. Lo Meo,* R. Noto, "*Silver nanoparticles stabilized by a polyaminocyclodextrin as catalysts for the reduction of nitroaromatic compounds"* Journal of Molecular Catalysis A: Chemical 408 (2015) 250–261

*** Corresponding author**

List of Communications

C1. M.F. Alberghina, **F. Armetta**, S. Bastone, E. Caponetti, D. Chillura Martino, E. De Castro, G. Chirco, C. Greco, V. Renda, S. Ridolfi, M.L. Saladino, S. Schiavone, "*One day at the Abatellis museum in Palermo discovering the "Trionfo della Morte" fresco: "Arte è Scienza" confirms to be one of the best practice to diffusion of the scientific culture on CH field*". X Congresso Nazionale AIAR 2018, Torino, 14-17 febbraio 2018. Poster

C2. D. Chillura Martino, C. Elisa Portale, M. de Cesare, M.L. Saladino, G. Chirco, V. Renda, **F. Armetta**, E. Caponetti, "*Pictorial techniques on Greek vases: an Attic white-ground crater and the "Centuripe" ware*". X Congresso Nazionale AIAR 2018, Torino, 14-17 febbraio 2018. *Poster*

C3. M.L. Saladino, V. Renda, **F. Armetta**, S. Ridolfi, S. Tusa, E. Caponetti, "*Investigation of eight Helmets founded in three different Sicilian underwater archeological sites*", IMEKO TC4 International Conference on Metrology for Archaeology and Cultural Heritage 2017, Lecce, October 23-25, 2017. *Poster*

C4. E. Caponetti, M. Berrettoni, **F. Armetta**, S. Tusa, "*Gela Oricalchum Ingots: a Multianalytical Approach*", IMEKO TC4 International Conference on Metrology for Archaeology and Cultural Heritage 2017, Lecce, October 23-25, 2017. *Presentazione orale*

C5. M.L.Saladino, **F. Armetta**, D. Hreniak, L. Marciniak, W. Stręk, C. Giordano, E.Caponetti, "Non conventional based Ce:YAG nanocomposites" XXVI Congresso Nazionale della Società Chimica Italiana 2017, Paestum (SA) 10-14 settembre 2017 (Italy). *Comunicazione orale*.

C6. M.L.Saladino, S. Ridolfi, **F. Armetta**, S. Bastone, V. Renda, A. Spinella, G. Nasillo, R. Pitonzo, D. Chillura Martino, E.Caponetti, "*A physical-chemical approach to the investigation of Objects of artistic and archeological interest*" XXVI Congresso Nazionale della Società Chimica Italiana 2017, Paestum (SA) 10-14 settembre 2017 (Italy). *Poster*.

C7. M.L.Saladino, S. Ridolfi, D. Chillura Martino, **F. Armetta**, S. Bastone, V. Renda, G. Chirco, E.Caponetti, "*A multi-analytical non-invasive and micro-invasive approach to oil paintings on canvas or wood. General considerations from some specific cases*" XXVI Congresso Nazionale della Società Chimica Italiana 2017, Paestum (SA) 10-14 settembre 2017 (Italy). *Poster*.

C8. M.L. Saladino, **F. Armetta**, V. Renda, S. Bastone, A. Spinella, G. Nasillo, R. Pitonzo, Delia Chillura Martino, E. Caponetti, "*Strumentazione e apparecchiature da laboratorio: esempi di un connubio efficace*" Convegno Tematico AIAr Beni Culturali: grandi facilities, reti e networks di laboratori, Firenze, 8 – 10 Marzo 2017 (Italy). *Poster*.

C9. R. Pitonzo, **F. Armetta**, M.L. Saladino, E. Caponetti, F. Oliveri, S. Tusa "*Application of Gas Chromatography coupled with Mass Spectroscopy (GC/MS) to the analysis of archeological ceramic amphorae belonging to the Carthaginian fleet that was defeated in the Egadi battle (241 B.C.)*" Metrology for Archaeology and Cultural Heritage, 19-21 Ottobre 2016, Torino (Italy). *Poster*.

C10. M.L. Saladino, **F. Armetta**, S. Bastone, D. F. Chillura Martino, G. Chirco, G. Nasillo, R. Pitonzo, V.Renda, A. Spinella, E. Caponetti, "*Diagnostic of Cultural Heritage: the synergy between portable instruments and laboratory instrumentations*" Metrology for Archaeology and Cultural Heritage, 19-21 Ottobre 2016, Torino (Italy). *Comunicazione*

orale.

C11. D. F. Chillura Martino, M.L. Saladino, **F. Armetta**, R. Lombardo, E. Caponetti, "*The role of a confined enviroment on the YAG nanoparticles*" XLIV Congresso della Divisione di Chimica Fisica della SCI, 20-23 Settembre 2016, Napoli (Italy). *Comunicazione orale*.

C12. M.L. Saladino, **F. Armetta**, G. Russo, D. F. Chillura Martino, E. Caponetti, "*One-step synthesis of Ce:YAG nanoparticles using solvothermal method*" XLIV Congresso della Divisione di Chimica Fisica della SCI, 20-23 Settembre 2016, Napoli (Italy). *Poster*.

C13. D. Chillura Martino, M.L. Saladino, S. Bastone, **F. Armetta**, E. Caponetti, N. T. Dincheva, R. Arrigo, F. P. La Mantia "*Sviluppo di formulazioni biodegradabili e biocompatibili per la cura della persona e la detergenza della casa*" "La Chimica Verde in Sicilia: realtà e prospettive", 30 giugno 2016, Palermo (Italy). *Comunicazione orale.*

C14. M. L. Saladino, S. Bastone, **F. Armetta**, V. Renda, G. Chirco, D. Chillura Martino, E. Caponetti "Attività del gruppo "*Sintesi e caratterizzazione*" *nell'ambito della Green Chemistry*" "*La Chimica Verde in Sicilia: realtà e prospettive*", 30 giugno 2016, Palermo (Italy). *Comunicazione orale.*

C15. E. Caponetti, M.L. Saladino, G. Chirco, **F. Armetta**,V. Renda, F. Filizzola, I. Carocci, S. Ridolfi, *"Il dipinto su tela S. Maria delle Grazie: il dilemma risolto" XVI Congresso Nazionale di Chimica dell'ambiente e dei Beni Culturali* "Dall'emergenza alla salvaguardia: la chimica per un nuovo modello di sviluppo" 26-29 Giugno 2016 Lecce (Italy). *Comunicazione orale*.

C16. M.L. Saladino, **F. Armetta**, C. Giordano, E. Caponetti, "Synthesis of Ce:YAG nanoparticles via the formation of urea complexes" CIMTEC 2016- 5th International Conference "*Smart and Multifunctional Materials, Structures and Systems*" 5-9 june 2016, Perugia (Italy). *Comunicazione orale*.

C17. D. Chillura Martino, **F. Armetta**, M.L. Saladino, R. Lombardo, E. Caponetti, "*Synthesis of YAG precursor in microemulsion: effect of confined environment on the YAG nanopowder features (o formation)"* CIMTEC 2016- 5th International Conference "Smart and Multifunctional Materials, Structures and Systems" 5-9 june 2016, Perugia (Italy). *Poster*.

C18. L. Lo Grasso, A. Sabella, A. Pisciotta, **F. Armetta**, D. F. Chillura Martino, M. Massimi, S. Donadio, M. Sosio, R. Alduina, "*Role of the two component system Dbv6/Dbv22 in regulating A40926 biosynthesis in Nonomuraea sp.ATCC 39727*" III meeting in Biotecnologie ricerche di base interdisciplinare traslazionale in ambito biomedico IBIM–CNR, 17 -18 Dicembre 2015, Palermo (PA) (Italy). *Poster*

C19. E. Caponetti, S. Bastone, A. Spinella, **F. Armetta**, L. Brusca, V. Tusa, C. A. Buccellato, S. Ridolfi "*Approccio chimico-fisico allo studio degli elmi della battaglia delle egadi e del rostro di acqualadroni*" Convegno la Battaglia delle Egadi, 20-21 Novembre 2015, Favignana (TP) (Italy). *Comunicazione Orale.*

C20. M.L. Saladino, **F. Armetta**, M. Sibeko, A. S. Luyt, E. Caponetti "*Ce:YAG composites for white LED*" FISMAT 2015 Italian National Conference on Condensed Matter Physics, 28 settembre-2 ottobre 2015, Palermo (Italy). *Poster*.

C21. E. Caponetti, **F. Armetta**, S. Bastone, D. Chillura Martino, D. Capitani, A. Spinella,

"*Advanced solid state NMR techniques for the characterization of a waterlogged wood*" XV Congresso Divisione di Chimica dell'Ambiente e dei Beni Culturali – Società Chimica Italiana, 14 – 18 giugno 2015, Bergamo (Italy). *Poster*.

C22. M.L. Saladino, **F. Armetta**, M. Sibeko, A. S. Luyt, E. Caponetti, "Preparation and characterization of Ce:YAG-PMMA and Ce:YAG-PC composites for white LED" X Convegno Nazionale INSTM sulla Scienza e Tecnologia dei Materiali, 28 giungo-1 luglio 2015, Favignana (TP) (Italy). *Comunicazione orale.*

C23. **F. Armetta**, S. Bastone, D. Capitani, E. Caponetti, A. Spinella, "*Advanced solid state NMR techniques for the characterization of a waterlogged wood*" Technart, 27-30 aprile 2015, Catania (Italy). *Poster*

Acknowledgments

I would like to thank Prof. Eugenio Caponetti and Prof. Delia Francesca Chillura Martino for giving me access to use the lab facilities at the Department STEBICEF-UNIPA.

NMR, SAXS and TEM experimental data were provided by Centro Grandi Apparecchiature—ATeN- Center of Università di Palermo funded by P.O.R. Sicilia 2000–2006, Misura 3.15 Azione C Quota Regionale. Thanks to Dr. Alberto Spinella and Dr. Giorgio Nasillo for their help and precious suggestions.

Thanks to Dr. Ivana Pibiri and Dr. Camillo Sartorio for the registration of some excitation and emission spectra of the composites and nanocomposites.

Thanks to University of Palermo for supporting the research in London with the PJ-DR-CONTR-ESTERO-DA00.05 projects (Premi e contributi a studenti meritevoli o svantaggiati).

I would like to thank Prof. Cristina Giordano for the hospitality at Institut für Chemie, Technische, Universität Berlin (Germany) and at School of Biological and Chemical Sciences, Queen Mary University of London (UK). She was a mentor during these research visiting.

It is impossible to write about London without say thanks to Chiara Defilippi, which helps in the lab experiences.

A particular thank to Dr. Ing. Dariusz Hreniak and Dr. Ing. Łukasz Marciniak forgiving me access to use some of the instrumentations I need for the luminescent characterization of nanophosphors. They were also fundamental for the data interpretation giving me the opportunity to learn more than I hope in just one week of visiting (Institute of Low Temperature and Structure Research, Polish Academy of Sciences of Wrocław). Thanks to Prof. Wieslaw Strek for his valuable remarks and Mr. Robert Tomala for his help in QE measurements (Institute of Low Temperature and Structure Research, Polish Academy of Sciences of Wrocław).

Thanks to Motshabi Sibeko of Department of Chemistry, University of the Free State (Qwaqwa Campus), South Africa for the preparation of the composites by the melt mixing procedure.